Aus dem Zentrum für Neuropathologie und Prionforschung
der Ludwig-Maximilians-Universität München
Direktor: Prof. Dr. med. Jochen Herms

The Role of CBP in Forebrain Development - A Mouse-Model for Rubinstein-Taybi-Syndrome

Dissertation
zur Erlangung des Doktorgrades der Medizin
an der Medizinischen Fakultät
der Ludwig-Maximilians-Universität zu München

vorgelegt von

Michael Launspach

aus Deggendorf

2019

Mit Genehmigung der Medizinischen Fakultät

der Ludwig-Maximilians-Universität München

Berichterstatter: Prof. Dr. Ulrich Schüller

Mitberichterstatter: Prof. Dr. Harald Steiner
Prof. Dr. Florian Heinen
Prof. Dr. Ortrud Steinlein

Dekan: Prof. Dr. med. dent. Reinhard Hickel

Tag der mündlichen Prüfung: 11.04.2019

Eidesstattliche Versicherung

Ich, Michael Launspach, erkläre hiermit an Eidesstatt, dass ich die vorliegende Dissertation mit dem Titel “The Role of CBP in Forebrain Development – A Mouse-Model for Rubinstein-Taybi-Syndrome” selbständig verfasst, mich außer der angegebenen keiner weiterer Hilfsmittel bedient und alle Erkenntnisse, die aus dem Schrifttum ganz oder annähernd übernommen sind, als solche kenntlich gemacht und nach ihrer Herkunft unter Bezeichnung der Fundstelle einzeln nachgewiesen habe.

Ich erkläre des Weiteren, dass die vorliegende Dissertation weder in gleicher noch in ähnlicher Form einer anderen Prüfungsbehörde zur Erlangung eines akademischen Grades vorgelegt wurde.

München, den 09.05.2019

_____

Michael Launspach

Table of contents

Zusammenfassung

Das Rubinstein-Taybi Syndrom (RTS) ist eine archetypische neurologische Entwicklungsstörung, die durch Mikrozephalie, geistige Behinderung, postnatale Wachstumsverzögerung und typische Körper- und Gesichtsmerkmale charakterisiert ist. Ursache des RTS sind unter Anderem Mutationen in den CBP (CREB binding protein) und p300 kodierenden Genen. Bei diesen Proteinen handelt es sich um homologe, ubiquitär exprimierte Ko-Aktivatoren der Transkription mit Histon-Acetyltransferaseaktivität. Obwohl Studien mit Mausmodellen für das Rubinstein-Taybi Syndrom CBP und Histonacetylierung eine direkte Rolle für Kognition und Gedächtnisbildung postulieren, konnte bisher kein eindeutiges neuropathologisches bzw. anatomisches Korrelat für die beim RTS beobachteten Symptome geistige Behinderung und Lernschwäche, beschrieben werden. Um die Pathogenese des RTS besser zu verstehen, wurde im Rahmen dieser Arbeit die Rolle von CBP während der Entwicklung des Großhirns untersucht. Dabei wurde ein konditionales homozygotes CBP knock-out Maus Modell verwendet. Mit Hilfe eines cre-loxP Systems wurde das CBP Gen spezifisch in GFAP exprimierenden neuronalen Vorläuferzellen zu einem frühen embryonalen Zeitpunkt inaktiviert. Die Auswirkungen dieses frühen CBP Verlusts auf das sich entwickelnde Gehirn wurden mittels histologischer Auswertung von Gewebeproben, 3D Zell-Rekonstruktion und Verhaltenstests untersucht.

In den transgenen Mäusen konnten Mikrozephalie, ein dünnerer Neocortex und Balken, sowie ein kleinerer Hippocampus und Bulbus Olfaktorius festgestellt werden, was die beschriebene besondere Bedeutung von CBP für regelhaftes Größenwachstums des Gehirns bestätigt. Weiterhin wurden verschiedene Hinweise auf eine gestörte Zelldifferenzierung beobachtet: einerseits ein verschobenes Verhältnis von exzitatorischen zu inhibitorischen Neuronen im Bulbus Olfaktorius, sowie anderseits ein vermindertes Zellvolumen von 3D-rekonstruierten Pyramidenzellneuronen der Lamina V des Neocortex. Außerdem konnte gezeigt werden, dass ein früher CBP Verlust zu einer verringerten Zellviabilität sowie verminderten Proliferationskapazität von embryonalen neuronalen Vorläuferzellen innerhalb der ventrikulären Keimzone führt. Darüber hinaus ließen sich ausgeprägte Störungen sowohl der radialen Vorläuferzell-Migration während der Entwicklung des Neocortex, als auch der tangentialen Vorläuferzell-Migration durch den rostralen migratorischen Strom (rostral migratory stream, RMS) oder während der Hippocampusentwicklung feststellen. Dies legt nahe, dass Migrationsstörungen auch während der Pathogenese des RTS eine wichtige Rolle spielen. Die beobachteten Fehlentwicklungen von

Neocortex, Corpus Callosum und Hippocampus nach CBP Verlust - insbesondere eine dabei verminderte adulte Neurogenese im Hippocampus - unterstützen insgesamt die bisherige Theorie, dass es sich bei diesen Hirnregionen um diejenigen zentral betroffenen Regionen handelt, die die klinischen neurokognitiven Befunde des RTS bedingen. Schließlich zeigten diese Ergebnisse auch deutliche Übereinstimmungen mit den Befunden struktureller Vermessungen von MRT Untersuchungen des Gehirns von RTS Patienten, welche ergänzend im Verlauf dieser Arbeit durchgeführt worden waren.

Summary

Rubinstein-Taybi syndrome (RTS) is an archetypic neurodevelopmental disorder characterized by microcephaly and mental retardation, postnatal growth impairment and distinctive facial & skeletal features. It is associated with heterozygous mutations in the CREB binding protein (CBP) and p300 genes that code for two strongly homologous ubiquitously expressed transcription coactivators with intrinsic histone acetyltransferase (HAT) activity. Though studies in mouse models for RTS suggest a direct role of CBP and histone acetylation in cognition and memory, no anatomical substrates for the findings of mental retardation and learning disability in RTS patients have been pin-pointed so far. Thus, to elucidate RTS pathogenesis further, the role of CBP during forebrain development was studied in this work utilizing a conditional homozygous CBP knock-out mouse model. Using a cre-loxP system the CBP gene was knocked out specifically in GFAP expressing neural precursor cells at early embryonic stages. The effects of this early CBP loss where then studied in the developing brain through histological analysis of brain tissue, 3D cell reconstruction and behavioral testing.

In the transgenic mice microcephaly, a thinner neocortex & corpus callosum as well as a smaller hippocampus & olfactory bulb were observed which corroborates a high importance of CBP for brain size regulation as postulated before. With disturbed excitatory and inhibitory balance of neurons in the olfactory bulb and a reduced cell volume of 3D reconstructed lamina V pyramidal neurons, cell differentiation was found to be disturbed after CBP depletion. It could furthermore be determined that a loss of CBP leads to diminished cell viability and reduced proliferation rates of neural precursor cells within the germinal ventricular zone during embryonal stages. Moreover, profound impairment of both radial migration during neocortex development, as well as of tangential migration through the rostral migratory stream and during hippocampus development were shown, strongly suggesting that impaired migration also plays an important role during RTS pathogenesis. In terms of an anatomical substrate for RTS related cognitive impairment, it can be noted that the alterations found in the neocortex, corpus callosum and hippocampus after loss of CBP - especially with a reduction of adult neurogenesis - heavily support the theory of these areas being the main substrates for the findings in RTS patients. Finally, these results were shown to be corresponding well with a structural analysis of acquired brain MRI images from RTS patients that was conducted additionally during the course of this work.

1. Introduction

1.1 Rubinstein-Taybi syndrome

Rubinstein-Taybi syndrome (RSTS or RTS; OMIM #180,849, #613,684), firstly described in 1963, is an archetypic neurodevelopmental, multiple congenital anomalies/mental retardation syndrome with a prevalence of 1:100,000 to 1:125,000 at birth[1,2]. Still primarily clinically diagnosed, RTS is characterized by microcephaly and mental retardation, postnatal growth impairment, specific facial abnormalities and broad & angulated thumbs and big halluces[1,3,4]. Genetic analysis uncovered heterozygous mutations in the strongly homologous CREB binding protein (CBP) and p300 (also called EP300 or E1A binding protein p300) genes to be causative for the development of RTS in about 50-70% of the cases, whereupon the cause of the other 30-50% remain unknown up to date[5,6,7,8,9] (Fig. 1).

1.1.1 Clinical characteristics

Beside the striking broad thumbs and big toes of many RTS patients - especially those with p300 mutations regularly have normally shaped thumbs and toes[7,9] - affected children show characteristic facial abnormalities such as highly arched eyebrows, down slanting palpebral fissures, a broad nasal bridge and beaked nose with the nasal septum extending below the nostrils, a highly arched palate and mild micrognathia[10]. Eye (i.e. congenital glaucoma)[11,12] and skin anomalies (i.e. hirsutism & keloid formation)[11,12,13] as well as affections of internal organs including heart malformations (~33%), kidney abnormalities and increased risk of seizures are also common[16,17]. Furthermore, RTS patients have an increased risk of developing both benign and malignant tumors, especially of neural or developmental origin[18,19]. Mental retardation in RTS is described as moderate to severe (IQ: <25-75) with a progression throughout life being discussed[12,19,20]. While the ability to establish social contacts is usually well intact, RTS patients often show a short attention span and poor coordination as well as sudden mood swings that may increase from early adulthood on[3].

1.1.2 Genetics

Though showing autosomal dominant character, RTS is caused by de novo mutations in most cases[21,22]. Causative mutations in the CBP gene include foremost point mutations, small deletions

and duplications that may lead to premature translations stops, substitutions or splicing defects, as well as, though less frequent, large deletions, translocations and inversions[5,23–25] (Fig. 1). Mosaic carriers of mutations have also been described what could be an explanation for some cases where no RTS causing mutations had been detected[26,27]. With regard to genotype-phenotype correlation, no striking correlations especially concerning mental retardation have been described up to date with the exception of the aforementioned often normally shaped thumbs and toes of patients with p300 mutations, more frequent growth retardation when the mutation did not lie within the CBP gene, a higher rate of seizure disorders in patients with CBP mutations and single cases of CBP missense mutations with milder phenotypes[6,28,29].

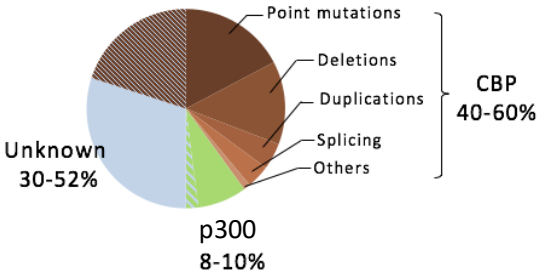

Figure 1: Causative mutations in Rubinstein-Taybi syndrome. The majority of RTS cases is caused by mutations in the CBP gene with point mutations & deletions making up for approximately 75% of all CBP mutations. (Others: insertions/deletions, insertions, translocations). In 8-10% of published RTS cases, p300 mutations have recently been discovered to be causative. CBP mutation type distribution is shown according to RTS cases listed in the Human Gene Mutation Database (HGMD, Qiagen Bioinformatics).

1.2 CREB-binding protein (CBP)

1.2.1 Function and structure

CBP, as well as its paralogue p300, is an ubiquitously expressed transcription coactivator known to play an important role in embryonic development, growth control, and homeostasis[30]. It has an intrinsic histone acetyltransferase activity and stabilizes protein interactions with the transcription complex, thus mediating chromatin remodeling and transcription factor recognition[31–33]. By acetylating histones, CBP opens the chromatin structure at a gene, which is essential for gene expression[34,35]. Its name derives from its early described ability to bind cAMP-response-element (CRE) binding protein (CREB)[36,37], by now, however, it was shown to integrate signals from a multitude of signaling pathways, interacting with more than 400 transcription factors and other regulatory proteins[38]. It was found to be present at promotors of more than 16000 human genes[39]. The CBP coding gene is situated at p13.3 of chromosome 16, with its 31 exons encoding the 2442 amino acids long CBP protein[40,41]. Besides large intrinsically disordered regions - 60% of the sequence - CBP has a folded histone acetyltransferase (HAT) domain, that

contains a 60 amino acid, disordered, auto-inhibitory loop residue that regulates acetyltransferase activity[42], and several folded domains that form the interaction sites for activation domains of cellular transcription factors and other regulatory proteins like the transactivation domains 9aaTADs of the tumor suppressor p53[43–46] (Fig. 2).

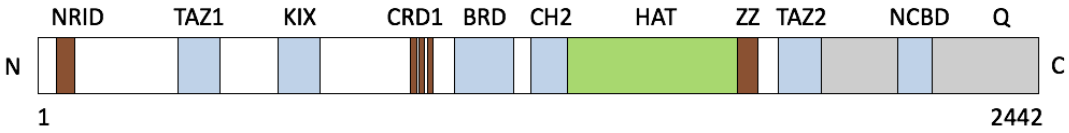

Figure 2: Domain arrangement of CBP. Schematic overview of the 2442 amino acids long protein CBP, its protein binding sites and other regions of interest. NRID: nuclear receptor interaction domain; TAZ1, TAZ2: transcriptional adapter zinc-binding motifs; TAZ1 domain mediates transcription of genes related to hypoxic response, the immune and inflammatory response, and cellular proliferation and survival[47,48]. By recruiting CBP, through interactions with TAZ2, various promoter-bound transcription factors activate transcription[30]. KIX: partner of kinase-inducible domain (KID) of CREB. The primary interaction site for various cellular transcription factors related to hematopoietic differentiation[49–52]; CRD1: cyclin-dependent kinase inhibitor-reactive domain; BRD: bromodomain. Recognizes acetyl-lysine residues in histone tails and intrinsically disordered protein regions of transcription factors[53]; CH2: cysteine-histidine-rich domain 2. A non-canonical zinc finger interacting with the preceding bromodomain and mutually stabilizing each other[54]; HAT: (histone) acetyl transferase domain, including a disordered regulatory loop; ZZ: dystrophin-like small zinc-binding domain; NCBD: nuclear receptor coactivator binding domain, also called iBiD; Q: Glutamin-rich region at the C-terminus[55]. *Based on figure 1 from Dyson, H. J. & Wright, P. E. Role of Intrinsic Protein Disorder in the Function and Interactions of the Transcriptional Coactivators CREB-binding Protein (CBP) and p300. J. Biol. Chem. 291, 6714–6722 (2016).*

1.2.2 Target of viral proteins

CBP - and p300 - with their important role as hubs in critical signaling and transcriptional networks are both targeted by disordered viral proteins and oncoproteins, which compete with cellular proteins, disrupt cell signaling and manipulate the cell cycle[56]. These include, amongst others, oncoproteins encoded by DNA tumor viruses such as adenovirus E1A and human papillomavirus E7, Tax and HBZ proteins encoded by the human T-cell leukemia virus HTLV-1, and the HIV-1 Tat protein[57–62].

1.2.3 Role in oncology

In terms of tumorigenesis and tumor progression, mutations in, or affecting the CBP gene have been reported in a number of malignancies. Chromosome translocations including the CBP gene locus that lead to a heterozygous loss of CBP have been found in acute myeloid leukemia and

treatment related hematological disorders[41,63–65]. Mutations especially in the HAT domain or domains important for transcription factor interaction were also described in cases of relapsed acute lymphoblastic leukemia and B-cell lymphomas[66,67]. In solid tumors, somatic mutations at the 16p13 CBP locus have been described for primary pulmonary cancer and pulmonary cancer cell lines[68,69], as well as in human medulloblastoma[70,71]. This is in line with the aforementioned findings in RTS patients of an increased risk of developing tumors (see 1.1.1.). It is furthermore discussed whether CBP acts as a tumor suppressor in tumorigenesis. On the one hand, CBP mutations especially in solid tumors are generally uncommon[72] and studies showed reduced proliferative capacity after loss or knockdown of CBP[73,74], what speaks against the role as a classical tumor suppressor. Studies on knock-out and conditional knock-out mice, on the other hand, confirmed a role as a tumor suppressor in hematological malignancies[75] and recently also in sonic hedgehog (SHH) medulloblastoma development, suggesting a different role at different developmental time points. While at early embryonal stages indispensable for proliferation and growth of the developing organism, CBP might act as a tumor suppressor later on[76].

1.3 Development of the cerebrum in mice

Approximately mid-gestation in rodents, on gestational day E9.0 - E9.5 of mice occurs the formation of the so called neural tube. A specialized fold of ectodermal tissue from which brain and spinal cord subsequently differentiate. This process is called neurulation and marks the first major step towards central nervous system (CNS) development in all vertebrates[77,78]. From the neuroectoderm of the anterior neural tube arises the forebrain (also called prosencephalon) which represents the foremost subdivision of the embryonic vertebrate brain. It further divides into the telencephalon, the diencephalon, that consists of structures such as thalamus and pretectum, and the hypothalamus[79,80]. From the telencephalon emerges eventually the cerebrum. It contains the cerebral cortex as well as subcortical structures like the hippocampus, basal ganglia and olfactory bulb. The other subdivisions, midbrain (also called mesencephalon), hindbrain (also called rhombencephalon) and spinal-cord develop into the respective parts of the CNS. With the dorsal bifurcation of the expanding telencephalon to form the two hemispheres and the patterning into ventral and dorsal telencephalon (also called subpallium and pallium) begins the development of distinct cerebral structures[80,81] (Fig. 3).

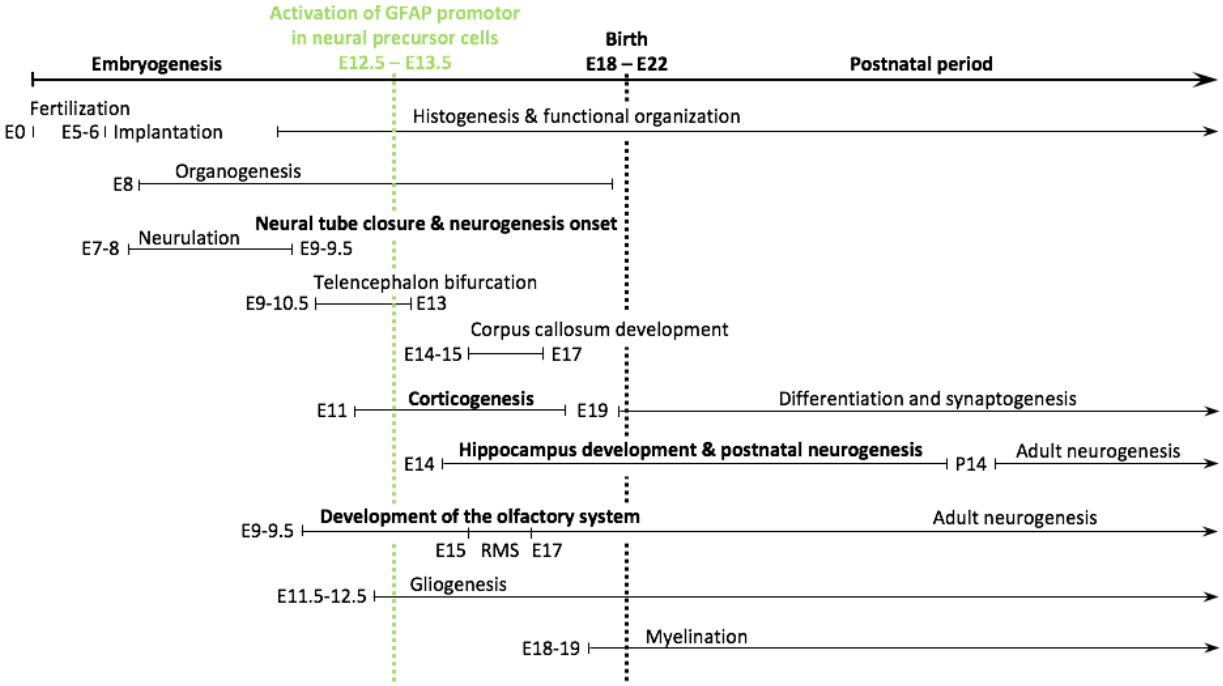

Figure 3: Timeline overview of the cerebral development in mice. Different developmental processes of the cerebrum against the background of the general embryonic and postnatal development of mice. Time points are labeled as embryonic (E) and postnatal (P) days post fertilization. As onset time points and process durations may vary between different strains of mice and due to inconsistency in nomenclature all time points were used as published: Implantation[82]; Organogenesis[83–85]; Neurulation[86]; Neural tube closure & neurogenesis onset[78,87]; Telencephalon bifurcation[88]; Corpus callosum development[89,90]; Corticogenesis[91]; Hippocampus development[92–94]; Development of the olfactory system[95]; Gliogenesis[96,97]; Myelination[98]; Activation of GFAP promotor in neural precursor cells[99,100]. The figure was inspired by figure 1 out of *Vorhees CV. Principles of behavioral teratology. In: Handbook of Behavioral Teratology (Riley EP, Vorhees CV, eds). New York:Plenum Press, 1986; 23-48.*

1.3.1 Corticogenesis

The developed neocortex - the outer covering of the cerebral hemispheres - is the seat of higher cognitive functions and especially well-developed in mammals[101]. It consists of a mantle of gray matter and the underlying white matter. While the gray matter comprises a network of excitatory (glutamatergic) and inhibitory (GABAergic) neurons supported by glial cells and blood vessels, the white matter is formed by myelinated axons stemming from, or directed to the neurons of the gray matter[102]. In the radial dimension the neurons of the gray matter are organized in columns working as functional microunits with stereotypical interconnections between the respective neurons[103,104]. In the lateral dimension the neocortex is dividable in six laminae (I-VI, with lamina I at the surface). The laminae can be identified by cell types and connectivity patterns[105]. For example, layer V and VI pyramidal multipolar neurons preferentially

connect with subcortical structures, whereas upper layer neurons (I-IV) mainly form ipsi- or contralateral cortico-cortical connections[106,107]. Further, the cortex as a whole is subdivided into a number of areas that represent functionally specialized fields[105].

The neocortex is formed during corticogenesis primarily from the dorsal telencephalon. Its neurons thereby originate from two germinal compartments lining the cerebral ventricles - the ventricular zone (VZ) and the subventricular zone (SVZ)[108]. The VZ initially consists of neuroepithelial cells (NECs) that divide at the apical surface. Later, mitosis also occurs at the basal surface and forms the SVZ[109,110]. The emerging precursor cells from which cortical neurons originate can be divided into different types and subtypes of which three outstanding types shall be explained in detail here. Firstly, elongated bipolar apical radial glial cells (aRGCs), spanning the full thickness of the embryonic cortical wall that function on the one hand as primary progenitor cells capable of generating neurons, astrocytes and oligodendrocytes and on the other hand as scaffolds for migrating neurons travelling to their destination in the cortex[108,111,112]. Secondly, apical intermediate progenitor cells (aIP, also known as short neural precursor cells (SNPs)), also dividing at the apical surface of the VZ that produce post-mitotic neurons directly from the VZ[113,114]. And finally, from RGCs derived basal intermediate progenitor cells (bIPs) which divided away from the VZ into the SVZ to produce post-mitotic neurons from there[109,115]. In this context, it was shown through gene expression analysis that although the SVZ derives from the VZ the two zones have different precursor cell pools and that the VZ is generating only lower layer neurons while the SVZ generates both upper and lower layer neurons[116]. Before the neocortex laminae are formed the first generated neurons form a pre-plate that is then split by later-born cortical plate neurons into an outer marginal zone and inner sub-plate[117,118]. From then on newly generated postmitotic neurons migrate radially from the VZ and SVZ to the cortical plate to form the neocortical laminae. During this process deeper layers are formed by earlier-generated neurons and the later-born neurons migrate to successively higher layers[119,120]. Laminar organization is thereby directed by reelin, a multifunctional extracellular protein, that controls neuronal radial migration and proper positioning in cortical layers[121,122]. Besides this process of radial migration, it was shown recently that the majority of GABAergic interneurons and a fraction of oligodendrocytes of the neocortex are generated in the ventral telencephalon and migrate tangentially to the cortical plate[123–126] (Fig. 4). In terms of inter-species differences, it has to be noted that the human neocortex is not only comparably larger than that of the mouse

but also convoluted (gyrencephalic) with fissures (sulci) and ridges (gyri) while the mouse neocortex is smooth (lissencephalic)[127,128]. While basic principles are conserved between mammalian species, there are also notable differences in the process of corticogenesis such as differences regarding the abundance of certain NPC types[129], the complexity of their lineages[130,131] and their proliferative potential[115,130,132,133]. This has to be taken into account when making inter-species comparisons.

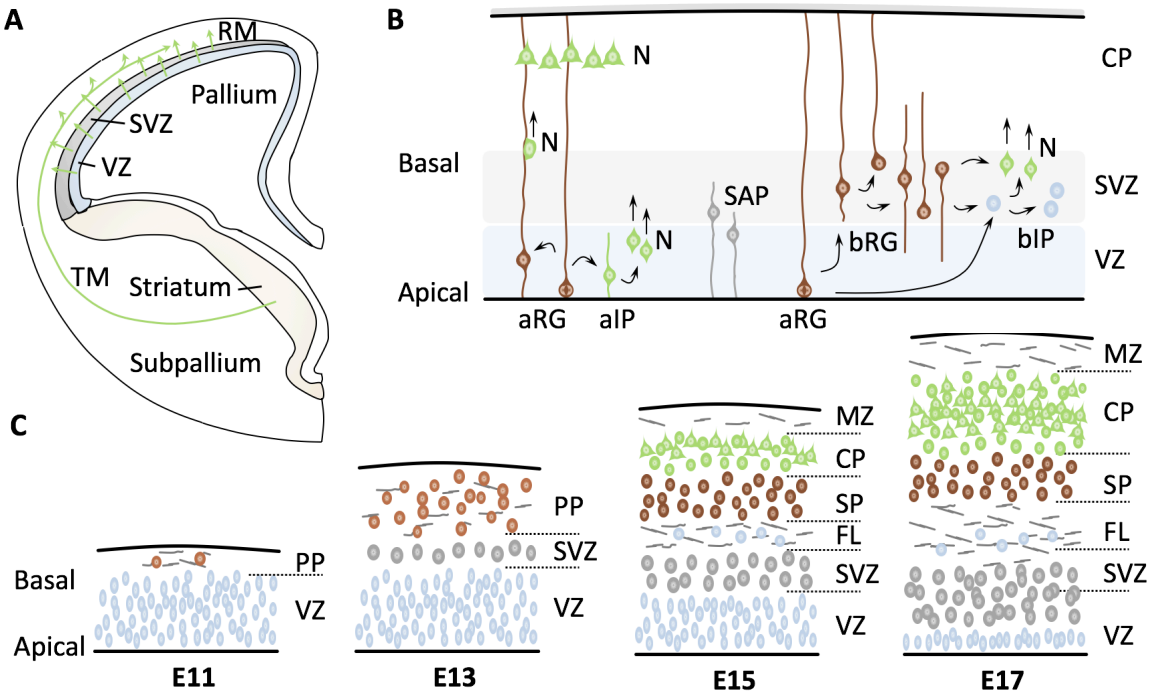

Figure 4: Corticogenesis in mice. ***(A)*** Migration movement during corticogenesis in a schematic coronal section. Radial migration (RM) of pyramidal neurons from the ventricular zone (VZ) and subventricular zone (SVZ) of the dorsal telencephalon (pallium) and tangential migration (TM) of interneurons to the developing neocortex from the striatum of the ventral telencephalon (subpallium). **(B)** Neural precursor cell (NPC) types during mammalian corticogenesis, classified according to cell polarity, the presence of ventricular contact, and the location of mitosis. Division behavior is labeled with curved black arrows. Neuroepithelial cells (NECs) that give rise to the following precursor cells are not depicted. Apical progenitor cells, which include apical radial glia (aRG) and apical intermediate progenitors (aIPs), are defined by mitosis occurring at the ventricular surface and the presence of ventricular contact. aIPS after being born from aRG follow one round of symmetric neurogenic division to givie rise to two neurons (N) that start migrating towards the cortical plate. Subapical progenitors (SAPs), a type of radial glia cells, are defined by mitosis occurring at an abventricular location and the presence of ventricular contact[134]. Basal progenitors (BPs), which comprise basal radial glia (bRG) and basal intermediate progenitors (bIPs), are defined by mitosis occurring at an abventricular location and the absence of ventricular contact[129,130]. The depicted bRG subtypes include bipolar bRG (bRG-both-P (P stands for process)), with both apical and basal processes, and monopolar bRGs: bRG-basal-P and bRG-apical-P[131,134]. bIPs born from aRG or bRG follow either symmetric proliferative division or symmetric neurogenic division[109,115,130]. **(C)** Anatomical organization of the embryonic cortex of mice at different embryonal time points. Schematics depict transects through the presumptive area 17 (primary visual cortex). While the

subventricular zone increases progressively in thickness throughout corticogenesis the ventricular zone declines progressively after E14, the day when the pre-plate (PP) begins to be separated into marginal zone (MZ), cortical plate (CP) and sub-plate (SP). Fibre layer (FL). **(A)** was derived from fig. 2 out of *Marin, O. & Rubenstein, J. L. A long, remarkable journey: tangential migration in the telencephalon. Nature Rev. Neurosci. 2, 780–790 (2001*). **(B)** was derived from fig. 2 out of *Florio, M. & Huttner, W. B. Neural progenitors, neurogenesis and the evolution of the neocortex. Development 141, 2182–2194 (2014).* **(C**) was derived from fig. 8 out of *Smart, I. H. M. et al. Unique morphological features of the proliferative zones and posmitotic compartments of the neural epithelium giving rise to striate and extrastriate cortex in the monkey. Cereb. Cortex 12, 37–53 (2002).*

1.3.2 Development of the hippocampus

The hippocampus is a ridge of grey matter located in the medial temporal lobe, elevating from the floor of each lateral ventricle which mediates important functions in learning, spatial navigation and memory[135–137]. The following structures are thereby included in the hippocampal formation: The dentate gyrus (DG), a trilaminar, convoluted semilunar (C-shaped) gyrus as the most medial area of the formation; The hippocampus proper with its 4 subfields CA1-CA4; And the subiculum that lies between the entorhinal cortex and the CA1 subfield[138]. The entorhinal cortex is an atypical organized cortical area acting as the main interface between hippocampus, neocortical areas and limbic cortices[139]. Different circuits and pathways that interconnect the structures of the hippocampal formation and entorhinal cortex have been described. For example, in the so called perforans path, axons from entorhinal cortex cross the partially fused hippocampal fissure and terminate in the DG. In turn, DG efferent axons, known as mossy fibers, form prominent bundles that synapse on CA3 pyramidal neurons. Neurons of CA3 mainly project to CA1 from which pathways lead to the subiculum and directly back to the entorhinal cortex, thus completing this so called trisynaptic circuit[140–142]. The subiculum, as the main output of the hippocampus, projects thereby not only to the entorhinal cortex but also to structures like the nucleus accumbens, lateral hypothalamus and amygdala[143].

The formation of the hippocampus starts around E14 in the Mouse in response to active secretion of BMP and WNT molecules from the cortical ham (CH), a dorsomedial telencephalic structure that also organizes the choroid plexus, and that lacks the transcription factor Lhx2[144,145,146]. BMP and WNT particularly promote the proliferation of neural precursors and are important for NSC (neural stem cell) maintenance and differentiation in the adult organism[147,148]. Nevertheless, some mechanisms during the embryonic development of the hippocampus equal those in the neocortex. As in the neocortex, glutamatergic projection neurons emerge from

radial glia precursors (RGPs) and intermediate precursor cells (IPs) and GABAergic interneurons migrate to the hippocampal site from subcortical progenitor compartments. Laminar organization is also regulated through reelin signaling and the CA segments are also formed through radial migration[149,150]. Especially unique, in contrast, is the development of the DG. It differs in molecular expression, mode of cell migration, hippocampal fissure formation, dependence on cortical hem signaling and its Cajal-Retzius (CR) cells, and shows prolonged neurogenesis with the peak of DG neurogenesis in rodents in the first postnatal week[151,152]. The DG originates from the dentate neuroepithelium (DNE), also called primary matrix, a part of the VZ that stands out with high expression of Lef1, an important transcription factor downstream of Wnt signaling[153,154]. From there, mitotically active NPCs at different stages of differentiation - both gliogenic and neurogenic - migrate towards the nascent hippocampal fissure (HF) forming the dentate migration stream (DMS) also called the secondary matrix that is supported by a glial scaffold made up from radial glia fibers[150,155,156]. This process depends heavily on hem-derived CR cells. Emerging from the cortical hem they disperse widely throughout the cortex and produce reelin. While all cortical areas are influenced by the cortical hem and CR cells the DG is especially dependent on these elements for patterning, growth and morphogenesis and CR cells promote DG development not only through reelin-dependent, but also reelin-independent mechanisms[157,158]. Reaching the hippocampal fissure, the NPCs form another hub of proliferating cells called the tertiary matrix and the granular cell layer starts to be formed[159]. Its semilunar two-bladed shape is thereby dictated by CR cells surrounding the hippocampal fissure. Thus, the hippocampal fissure itself plays an important directive part during the DG development and CR cells migrate into subpial and compact zones of the hippocampal fissure while beeing essential for its lengthening[160,153] (Fig. 5).

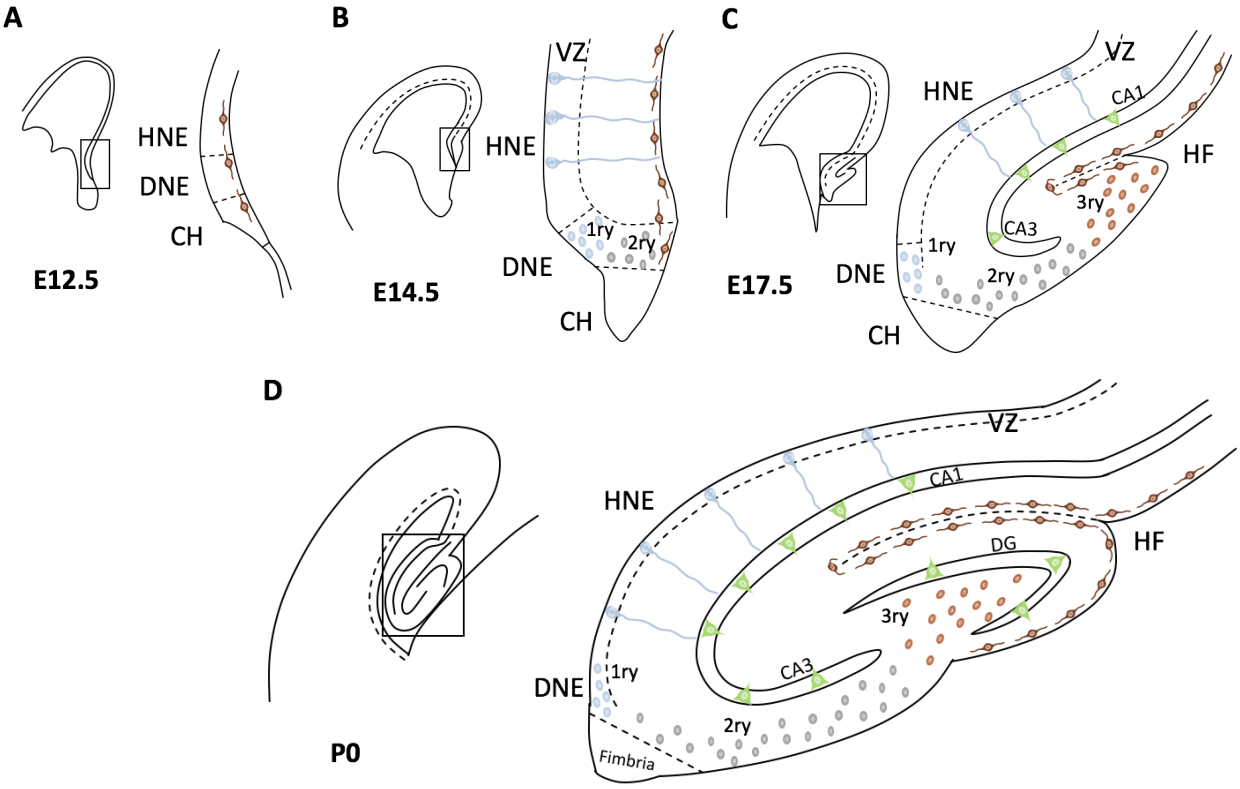

Figure 5: Development of the hippocampus in mice. Schematic representation of the pallium at different developmental stages. Squares indicate magnified hippocampal regions. **(A)** At E12.5, the presumptive, not yet distinguishable DNE is located between the hippocampal neuroepithelium (HNE) and the cortical hem (CH). CR cells (dark-brown) are shown lining the pial side of the cortex. **(B)** At E14.5 dentate precursor cells (blue circles) in the DNE, also called primary matrix (1ry), start migrating to the pial side of the cortex, thereby forming the dentate migration stream (DMS), the secondary matrix (2ry; gray circles). In the HNE segment of the VZ, RGPs are depicted (blue with process) that will give rise to neurons of the CA segments. **(C)** At E17.5 the hippocampal fissure (HF) is formed, NPCs migrate towards it and accumulate there forming the tertiary matrix (3ry; light brown circles). The glial scaffold which directs the migration process and extends from the CH to the HF and pial surface is not depicted. Differentiated neurons (green) of the CA segments, born from the HNE migrated via radial migration along radial glia cells (blue circles with processes) to their final positions. **(D)** At birth, the blades of the DG start to form. Granule neurons of the DG (green) settle first in the upper blade below the HF. The formation of the lower blade is then promoted by immigrating Cajal-Retzius cells after the upper blade is formed. NPCs in the primary and secondary matrix will then disappear leaving solely NPCs of the tertiary matrix with the postnatal production of granule neurons for the DG. The figure was derived from fig. 1 out of *Urbán, N. & Guillemot, F. Neurogenesis in the embryonic and adult brain: same regulators, different roles. Front. Cell. Neurosci.* ***8,*** *396 (2014).*

1.3.3 Development of the olfactory bulb & the rostral migratory stream

The olfactory system is being divided into two pathways. The primary olfactory pathway including the olfactory epithelium (OE) and the olfactory bulb (OB)[161], and the secondary olfactory pathway that comprises multiple higher cortical regions referred to as the olfactory

cortex, directly innervated by mitral and tufted cells of the OB via the lateral olfactory tract (LOT)[162]. The olfactory epithelium, a pseudostratified neuroepithelium derived from the olfactory placodes - special areas of non-neural ectoderm in the rostrolateral regions of the head visible at E9 - contains the olfactory sensory neurons (OSNs)[163]. OSN axons, alongside other migrating cells, exit the OE and form a presumptive olfactory nerve layer (pONL) by E12. OSN axons thereby enter the CNS through small fenestrations and grow into the developing OB finally establishing synaptic connections with the mitral, periglomerular and tufted cells of the OB's glomeruli[164–166]. The OB is the CNS structure where olfactory information is first processed and relayed before forwarded to higher cortical regions[167]. Olfactory signals are sharpened or filtered there through lateral inhibition mediated by the OBs granular cells, axonless local interneurons[168,169]. The formation of the OB begins slightly after the formation of the OE in a predetermined region of the rostral telencephalon, with mitral cell differentiation onset at E10.5-E11[170]. It was shown that the OB initially develops independently from the OE and its penetrating OSN axons, although the exact nature of the signals that induce OB formation are yet to be fully understood[171–173]. While the OBs projection neurons - mitral and tufted cells - are born within the OB and only exhibit short way radial migration to the OB's borders and undergo tangential reorientation there[174], OB interneurons - granular and periglomerular cells - are born in the subventricular zone lining the lateral ventricles mainly during early postnatal life and migrate as still undifferentiated neuroblasts into the OB along the so called rostral migratory stream (RMS) (Fig.6)[170,175]. Beside the migrating neuroblasts organized in chains, the RMS contains specialized surrounding glial cells which postnatally form a so called glial-tube that then serves as a scaffold for the migrating neuroblasts during adult neurogenesis (see 1.4.2)[176,177]. While the initial formation of the RMS occurs between E15 and E17, it was shown that pioneer populations of OB interneurons are generated from precursors in the lateral ganglionic eminence (LGE) - a progenitor domain of the ventral telencephalon that gives later rise to the striatum and globus pallidum[178] - between E12.5 and E14. They migrate towards the presumptive OB in a passage that adumbrates the RMS[179]. In terms of inter-species differences, it can be noted that, although differences in RMS morphology and structure exist, human RMSs also contain migrating neuroblasts and OB neurogenesis also persists into adulthood[180,181].

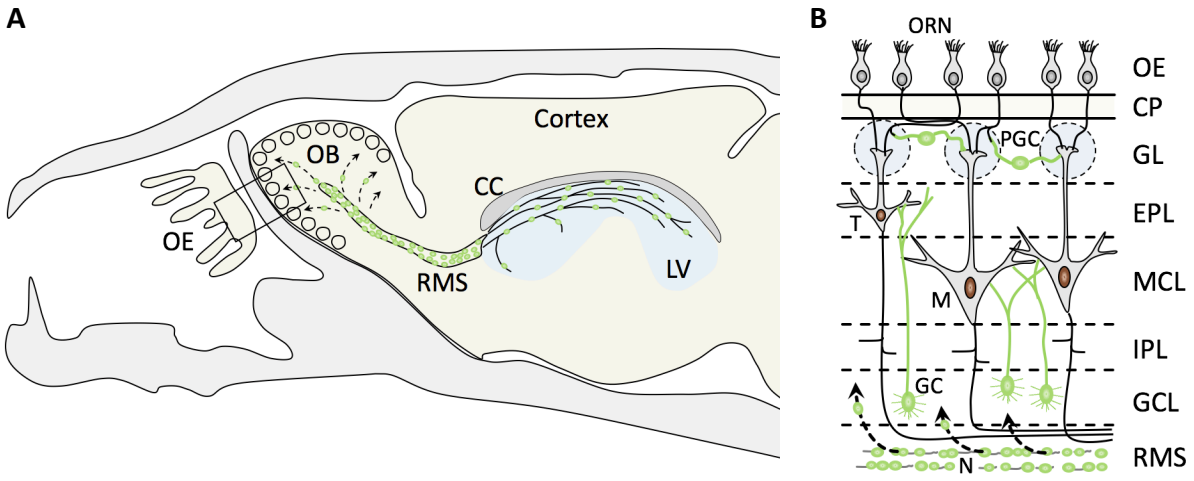

Figure 6: Overview of the adult olfactory bulb and neurogenesis via the rostral migratory stream. (A) Schematic sagittal paramedian section through an adult mouse head. Neuroblasts (green circles) born in the subependymal zone of the lateral ventricle (LV; blue) are shown forming the rostral migratory stream (RMS) and migrating towards the olfactory bulb (OB), where they then migrate radially (black arrows) towards their final destination within the OB. Corpus Callosum (CC); Olfactory epithelium (OE). The boxed area is shown enlarged in (B). **(B)** Schematic overview of the neuronal layers of the adult OB**.** Migratory neuroblasts (N) leave the RMS (black arrows) and differentiate into granule cells (GC) and periglomerular cells (PGC) residing in the granule cell layer (GCL) and glomerular layer (GL) respectively. Olfactory receptor neurons (ORN) in the olfactory epithelium (OE) project to the GL. The main projection neurons of the OB reside in the mitral cell layer (MCL) and external plexiform layer (EPL). Mitral cells (M) in the MCL and Tufted cells (T) in the EPL. Cribiforme plate (CP); Internal Plexiform layer (IPL). ***(A)*** *was derived from fig. 1 out of Lim, D. A. & Alvarez-Buylla, A. The Adult Ventricular–Subventricular Zone (V-SVZ) and Olfactory Bulb (OB) Neurogenesis. Cold Spring Harb. Perspect. Biol. 8, a018820 (2016).* ***(B)*** *was inspired by fig. 2 out of Doty RL, Kamath V. The influences of age on olfaction: a review. Front Psychol 5: 20, 2014.*

1.4 Adult neurogenesis

Besides neurons being generated during early embryonic development and early postnatal stages, only two main neurogenic regions remain in the adult brain that comprise of complex cellular microenvironments surrounding the NSCs keeping them quiescent and undifferentiated[182–185]. The subependymal zone of the lateral ventricles, also called the ventricular-subventricular zone (V-SVZ) that produces new neurons migrating to the OB[182,186]. And the non-periventricular subgranular zone (SGZ), the innermost layer of the DG in the hippocampus[187–190]. In contrast to the multipotency of embryonal NSCs, the different populations of stem cells in adult neurogenic regions are restricted to the generation of few types of neurons and glia cells. Granule neurons and astrocytes in the DG and granule or periglomerular neurons and oligodendrocytes or astrocytes in the V-SVZ[184,186,191–194]. Remaining in quiescence,

out of the cell cycle, in G0 for long periods - another difference to embryonal NSCs - is important for maintenance of tissue homeostasis and to avoid stem cell exhaustion[195]. The effects of signaling pathways, gene expression patterns and intrinsic factors on adult neurogenesis and its regulation mechanisms are the focus of current intensive research.

1.4.1 Adult neurogenesis in the hippocampus

During the second postnatal week, proliferation in the DG and former tertiary matrix declines and is eventually confined to the SGZ. The NSCs residing there throughout adulthood are called type-I cells or radial glia-like cells[196]. Thereby, it was shown recently that SGZ NSCs not only originate from the DNE but are also induced by sonic hedgehog (SHH) secreted from the amygdala at peri-natal stages in the ventral hippocampus and then migrate dorsally to seed the SGZ of the entire DG[197]. Granule cells in the adult DG are generated from type-I cells via a cell linage that includes rapidly dividing intermediate progenitor cells (IPCs) called type-IIa- and type-IIb cells and neuroblasts (type-III)[198]. Selective elimination of IPCs by microglia during this process is an important mechanism of regulating neurogenesis in the DG[199,200]. The addition of new granule cells to the hippocampus circuitry was shown to be crucial for the acquisition of a certain type of contextual memory[201,202]. Furthermore, situations such as physical exercise, task learning but also seizures stimulate neurogenesis in the adult DG[196]. The aging of the brain on the other hand goes along with a major decrease in the number of new neurons generated in in the DG. For one thing through reduction of the NSC pool and secondly through an increased number of NSCs in quiescence[203–205].

1.4.2 Adult neurogenesis in the ventricular-subventrticular zone

In the first postnatal weeks, the assembly of the glial-tube sheathing the RMS and changes in the cell populations within the subependymal zone along the lateral ventricles mark the transition towards adult neurogenesis[176,206]. The region is then called ventricular-subventricular zone as it shows characteristics similar to both the embryonic VZ and SVZ. During that process, embryonic NSCs which display undifferentiated radial glia characteristics differentiate to specialized astrocytes with ventricular contact called type-B1 cells that represent the primary NSCs of the V-SVZ[207–211]. When activated from their quiescent state, type-B1 cells give rise to transit-amplifying precursor cells (type-C cells) which then produce neuroblasts (type-A cells) that travel to the

OB[212–215]. They can furthermore undergo asymmetric division for self-renewal or give rise to oligodendrocytes and non-neurogenic astrocytes[216]. However, type-B1 cells are thereby not a homogenous population of adult NSCs as their location throughout the V-SVZ determines the type of OB neurons they will produce[217,218]. For example, ventral type-B1 cells produce deep granule neurons and calbindin positive periglomerular cells, whereas dorsal type-B1 cells produce superficial granule cells and calbindin negative periglomerular cells. These regional specifications are moreover already established at early developmental prenatal stages[210]. Until now the number of subregions in the V-SVZ and how many different types of OB interneurons are produced is not known. It therefore remains uncertain whether type-B1 cells are to be considered multipotent and if both neuronal and glial linages can emerge from a single type-B1 cell[216,219].

2. Objective

Using the definition of the European Commission for rare diseases of affecting less than 1 in 2000 people and being life-threatening or causing chronic illness, this group entails 5000 - 8000 different diseases with the majority being of genetic origin[220,221]. As published in a WHO background paper from 2013 this leads to the rough estimate of 1 in 15 people as a worldwide prevalence of rare diseases making this group a challenging global health issue both in terms of clinical diagnosis and treatment as well as investigatory approach, due to its enormous heterogeneity[222]. Accordingly, cause and symptoms causing pathophysiological processes are yet to be fully understood in a great number of these rare diseases. This work aims therefore to elucidate the pathophysiological mechanisms and changes occurring during brain development that lead to the clinical picture of mental retardation and cognitive impairment in one of these entities, the Rubinstein-Taybi syndrome. More specifically, the sub-group of RTS cases, where the cause of the disease lies within mutations affecting the CBP gene. While the causative role of the heterozygous loss of CBP or its HAT activity has been shown sufficiently at various occasions[7,223], studies on heterozygous knock-out mouse models so far did not identify alterations in forebrain anatomy & -histology or pathological processes during their development that could explain satisfactorily the clinical findings of mental retardation and cognitive impairment in RTS patients[224–226]. Hence, in this work a different approach was chosen by studying the in vivo effects of a complete loss of CBP during embryonal development in a conditional homozygous CBP knock-out mouse model using a cre-loxP system. A focus was thereby placed on the analysis of integrity and development of the forebrain structures neocortex, hippocampus and olfactory bulb as well postnatal neurogenesis and developmental processes like precursor cell proliferation, neural migration and neural cell differentiation. Furthermore, the effect of CBP loss on neural cell structure was studied through 3D cell volume reconstruction of lamina V pyramidal cells. A mutation frequency analysis of mutations throughout the CBP gene in published RTS cases was conducted to validate the induced mutation in the used mouse model as a possible RTS causing mutation. Finally, data from magnetic resonance imaging (MRI) of the head and brain of RTS patients was acquired and analyzed in terms of structural parameters. Results were then compared to findings in the conditional CBP knock-out mouse model.

3. Material and methods

3.1 Animal experiments

For this work *hGFAP-cre*[99] & CBP$^{Fl/Fl;\ 227}$ transgenic mouse lines were used. All animal procedures were performed in accordance with the policies on the use of animals established at the institute *Zentrum für Neuropathologie und Prionforschung* of the LMU Munich and the applicable animal protection law. All experiments were approved by the state of Bavaria under license number 55.2-1-54-2532-10-14. Mice were held in groups of up to five animals in standard individually ventilated cages in an apathogenic environment at 23±2°C. They were separated according to their sex. A day/night cycle of 12 hours was maintained and the animals had free access to autoclaved food and water. For brain preparation, adult animals were sacrificed through manual cervical dislocation and animals aged younger than 14 days through decapitation.

3.1.1 *hGFAPcre::CBP$^{Fl/Fl}$* transgenic mouse model

To assess the impact of CBP-knockout specifically in the developing brain *hGFAP-cre* & *CBP$^{Fl/Fl}$* mice were mated to generate *hGFAPcre::CBP$^{Fl/Fl}$* transgenic mice. In this homozygous conditional knock-out model, the loxP flanked (floxed) CBP-gene is knocked out in those cells that start expressing GFAP and under its promoter the cre-recombinase (Fig.7). This accounts mainly for neural precursor cells at about E12.5 - E13.5[99,100]. Male and female animals were used equally in the study. For control groups animals which were either categorized as wildtype or which had solely a *hGFAPcre*, *CBP$^{Fl/Fl}$* or *CBP$^{Fl/+}$* genotype were used. *hGFAPcre::CBP$^{Fl/+}$* heterozygous knock-out mice were investigated additionally on a basic level.

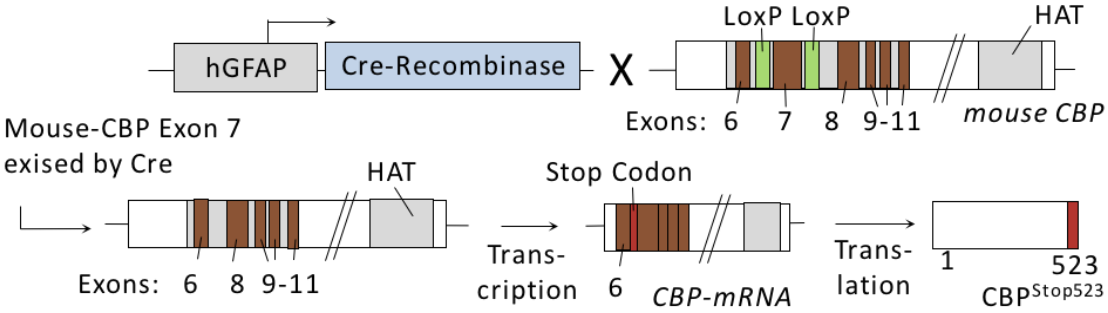

Figure 7: RTS mouse model: *hGFAP-cre::CBP$^{Fl/Fl}$*. In *hGFAP-cre::CBP$^{Fl/Fl}$* mice only CBP^{Stop523}, an insufficient C-terminally truncated version of the mouse CBP, is expressed in those cells that express the cre-recombinase under the GFAP promotor. CBP^{Stop523} does no longer contain the HAT domain. LoxP: Cre-recombinase recognition and incision site, HAT: Histone acetyltransferase domain

3.1.2 Genotyping

For genotyping biopsies of the tail from three-day old mice were used. The tissue was beeing lysed on the thermal mixer for two hours at 56 °C with 500 µl of a lysis buffer (200 mM NaCl, 100 mM Tris-HCl pH 8.3, 5 mM EDTA, 0.2% SDS, 200 µg/ml protein kinase K in ddH_2O). Afterwards, the probes were being centrifuged for 5min at 14000 g and the supernatant diluted with 500 µl isopropanol. Shaking then caused precipitation of the genomic DNA and the probe was again being centrifuged for 5 min at 14000 g. The pellet was dissolved in TE buffer (20 mM Tris-HCL pH 8.3, 1 mM EDTA in ddH_2O and stored at 4 °C. This genomic DNA served as raw material for the following process of determining the animal's genotype: Genotype-specific regions of the genome were amplified via PCR utilizing primers inspired by the original publications (see 3.1.1) and a TAQ-Polymerase based standard reaction mixture (Table 1). Analysis of the amplified DNA fragments was conducted through gel electrophoresis using 1% agarose gel plates and a Syngene documentation system (Synoptics Limited).

Primer name	**5' - 3' Sequence**
Cre fwd.	TCCGGGCTGCCACGACCAA
Cre rev.	GGCGCGGCAACACCATTTT
CBP fwd.	CCTCTGAAGGAGAAACAAGCA
CBP rev.	ACCATCATTCATCAGTGGACT

PCR step	**Temperature [°C]**	**Duration [s]**	**No. of repeats**
Denaturation	95	120	1
Denaturation	95	30	35
Annealing	60	30	
Elongation	72	60	
Elongation	72	120	1
Stop	4	-	

Table 1: Primer sequences and PCR cycle specifications used for genotyping

3.1.3 BrdU/EdU double pulse fate-mapping

For measuring the proliferation rate in different cerebral structures in vivo, 25 µg bromodeoxyuridin (BrdU) per gram bodyweight was injected intraperitoneally two hours before sacrificing the animal. Analogous to the thymidine nucleoside, BrdU is integrated into newly formed DNA. Subsequently, it is possible to identify cells that passed the S-Phase during the two hours after the BrdU pulse using immunohistochemistry. To furthermore compare proliferation at different time points in the same animal and thus to be able to analyse cell migration from

stem cell rich regions to their respective destinations, a BrdU/EdU double pulse fate-mapping method was utilized. 5-ethynyl-2´-deoxyuridine (EdU), an alkyne-containing thymidine analogue, incorporated into DNA during active DNA synthesis like BrdU, was also administered intraperitoneally at 25µg per gram bodyweight. The double pulse method consisted of two injection steps. At a first time point, BrdU was injected and after a chosen interval, EdU was applicated and the animal was sacrificed. Hence, the stem cells were labeled with BrdU during active proliferation in the living animals, travelled to their destination and where identified histologically there (Fig.8). EdU on the other hand labeled new active stem cells in the area of their origin before migration in the same animal. Furthermore, this method also helped to rule out that the BrdU positive cells after migration were in fact stationary continuously proliferating cells of the destination region. Those cells would have been found to be both BrdU and EdU positive. For analysis, a fluorescence double staining of tissue sections was performed. EdU positive cells were stained by using the Click-IT® assay (ThermoFisher).

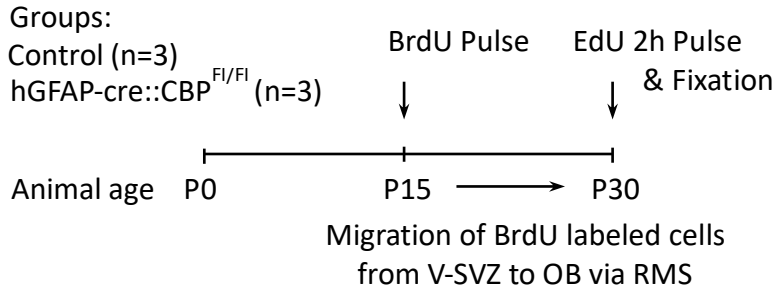

Figure 8: Example for a BrdU EdU double pulse fate-mapping. To retrace cell migration from the ventricular-subventricular zone (V-SVZ) to the olfactory bulb (OB) via the rostral migratory stream (RMS) proliferating cells in the V-SVZ were marked at P15 through BrdU injection. Fifteen days later, EdU was injected and the animals were sacrificed for analyzing sections of the OB and RMS immunohistochemically.

3.1.4 Behaviour testing

To investigate whether structural and histological findings in the olfactory bulb and rostral migratory stream in *hGFAPcre::CBP$^{Fl/Fl}$* transgenic mice reflected in disorders of functional systems two behaviour tests that are used to assess the olfactory sense were conducted: a modified buried food and an olfactory habituation/dishabituation test[228,229]. Besides olfactory testing an anxiety/curiosity test was utilized to determine this confounding variable. All tests were conducted between 9 am and 9 pm. The animals were accustomed to the test room for at least 24 hours prior to testing. Gender-matched litter mates with genotypes as described in 3.1.1

where used as a control group. All tests were performed with animals at P30. The animals' genotypes were unknown to the tester during testing. Females and males were tested separately but indiscriminately included in the analysis.

To investigate anxiety and curiosity a light/dark box test was used. It is based on the fact that rodents react aversive when confronted with brightly illuminated areas on the one hand, but display exploratory behaviour in front of novel environment on the other hand[230,231]. The test box consisted of a smaller dark and closed chamber which was connected through a door to a bigger, illuminated and at the top open compartment painted in white. The box measured 60 cm in length, 40 cm in width and 40 cm in height with the bright compartment taking up two thirds of the floor space. Each animal was kept in the box for 5 minutes, whereby the latency until the first transition from the dark to bright compartment, the number of transitions and the total time spent in each compartment were measured.

In the buried food test the test subjects were put into standard cages in which pieces of chocolate (1g) were buried under 0.5cm of bedding. Then, the time until the mice had dug up the piece of chocolate was measured. If it was not found after 5 minutes, the trial was ended. The test was repeated 6 more times for each animal to reduce susceptibility to faults. In the 7th run, a surface pellet trial was conducted with the piece of chocolate lying visibly on top of the bedding to determine whether the chocolate had not been dug up before because the mouse either wasn't hungry or didn't accept chocolate as aliment. Animals who had not dug up the chocolate for more than two times or rejected chocolate in the surface pellet trial were excluded from the experiment afterwards. To increase search behaviour the mice weight was reduced to about 90% in the days before testing and chocolate was presented to them as an alternative aliment.

The used habituation/dishabituation test aims at determining whether a mouse can discriminate between familiar and novel, innocuous scents. Plastic cartridges carrying a piece of cotton impregnated with 20µl of either almond or banana extract were presented to the mice repeatedly for 30 seconds with 5 minute intervals. The first 6 trials almond extract was used for examining habituation and in a 7th trial banana extract was used as a novel scent to trigger dishabituation. The measured time variable 'nose-contact with the cartridge' was defined as the desired variable of 'time spent sniffing'. Animals which had shown no interest at all for the cartridges were excluded from the study afterwards.

3.2 Histological methods

3.2.1 Tissue preparation and standard staining

After sacrificing the animal, its brain was separated from the skull and the dura mater removed. Phosphate-buffered saline (PBS) was used to keep the brain from desiccating during the dissection. Tissue that was meant to be analysed through confocal microscopy for 3D cell reconstruction was fixated overnight in 4% paraformaldehyde in PBS at 4 °C and then processed to 100 µm slices using a VT1000S microtome (Leica Biosystems). Tissue destined for light or fluorescence microscopy was fixated overnight in 10% formalin solution containing about 4% formaldehyde at room temperature and was subsequently embedded in paraffin. The paraffin blocks were sliced using a sliding microtome (Leica Biosystems) and 3 µm slices of the regions of interest were affixed to Superfrost Plus microscope slides (Fisher) using a water bath at 40 °C. Before further use, affixed paraffin-slices were dewaxed in xylol and rehydrated in a series of decreasing alcohol concentrations. General morphology was analysed by means of hematoxylin/eosin (H&E) staining. For H&E staining a standard protocol was used.

3.2.2 Immunohistochemistry

After dewaxing and rehydration, the slices were cooked five times for 4 minutes in citrate buffer (pH 6) for antigen unmasking. Next, slices were incubated in 5% H_2O_2 in methanol for 15 minutes to inactivate endogenous peroxidases. Subsequently, the tissue was blocked for 30 minutes with I-Block casein-based blocking reagent (ThermoFisher Scientific) and afterwards incubated overnight with primary antibodies at 4 °C (Table 2). On the next day, the slices were developed using a 3,3'-diaminobenzidine (DAB) chromogen – HRP system (DAKO EnVision™+ System, HRP) following the manufacturer's instruction. A hemalum counter staining was performed as a nuclear staining for all chromogen procedures. For immunofluorescence staining, slices were incubated for one hour with species-specific fluorophore linked secondary antibodies (Alexa 488 & Alexa 546; Invitrogen) instead of using the DAB kit. Nuclear counter staining was performed with 4',6-diamidin-2-phenylindol (DAPI; Roth). PBS + 0.3% Triton X-100 (polyethylene glycol p-(1,1,3,3-tetramethylbutyl)-phenyl ether) was used in all washing steps for BrdU staining. For other antibodies, solely PBS was used. The 100 µm slices for 3D cell reconstruction were stained directly with NeuroTrace 530/615 (1:100; ThermoFisher), a red fluorescent Nissl stain, and Hoechst (1:1000; Invitrogen) as a nuclear counter staining both diluted in PBS + 0.3% Triton X-

100, after pre-incubating the slices for 30 minutes with PBS + 2% Triton X-100 to permeabilize the cells. All washing steps were performed with PBS. VECTASHIELD HardSet Antifade mounting medium (VECTOR Laboratories) was used for mounting.

Antigen	Provider	Catalogue no°	Dilution in I-Block
BrdU	Roche	11170376001	1:500
BrdU (clone Mobu-1) *	Invitrogen	B35128	1:100
Calbindin	Chemicon	AB1778	1:100
Caspase 3 (Asp 175)	Cell Signaling Tech	9664	1:100
CBP	Biozol	LS-B3360	1:50
Cre	Covance	PRB-106P	1:3000
HuB	Sigma	H1538	1:200
Ki67	Abcam	ab16667	1:200
Map2	Abcam	ab5392	1:100
MBP	Abcam	ab40390	1:100
NeuN	Abcam	ab104224	1:300
Olig2	Abcam	ab109186	1:100
Pax6	DSHB	Pax6	1:25
Prox1	Abcam	ab199359	1:500
S100	Abcam	14849	1:3000
Sox2	Abcam	ab79351	1:200
Synaptophysin	DAKO	A0010	1:100
Tbr2	Millipore	AB2283	1:300
Wfs1	Proteintech	11558-1-AP	1:50

*The BrdU Mobu-1 clone was used in BdrU-EdU double staining as it does not cross react with the Click-It assay

Table 2: List of primary antibodies used

3.3 Imaging and image analysis

Chromogen histological slides were examined under an Olympus Bx50 microscope with 4x, 10x, 20x and 40x objectives. Overview images were taken with an Olympus SZ51 stereo microscope. For fluorescence stained slides an Olympus IX50 microscope was used. Images were taken with the help of ColorView Soft Imaging Systems (Olympus). For 3D cell reconstruction z-stack series in layer V of the neocortex were acquired from 100 µm slices stained with NeuroTrace & Hoechst using a Zeiss LSM780 confocal microscope and ZEN microscope software (Zeiss). The hippocampus was used for orientation and determination of the region from which slices were used. The series were acquired at fixed intervals of 0.5 µm along the z-axis with an 20x objective and the same pinhole setting for both channels. Frame size was 1024x1024 pixels.

3.3.1 Stereological measurements

To increase validity and reduce variability a stereological approach was chosen for analysing the different forebrain structures. To account for its three-dimensional character, for each structure of interest three section planes were analysed in every animal of the *hGFAPcre::CBP*$^{Fl/Fl}$ - or control group. In each section plane, several measurements were executed and averaged for parameters such as cell layer thickness, cell density or composition to further reduce variability (Fig. 9). Section planes were chosen by recognizable landmarks in light microscopy instead of predetermined intervals as brain size was not a stable constant (see 4.2.1). All measurements were conducted on pseudonymised images with the help of the open source image processing program ImageJ. This investigation aimed to investigate possible differences between the transgene mouse model and the control group rather than to provide accurate values for the in vivo situation. Consequently, confounding variables affecting both groups equally, i.e. tissue shrinking after preparation, were ignored.

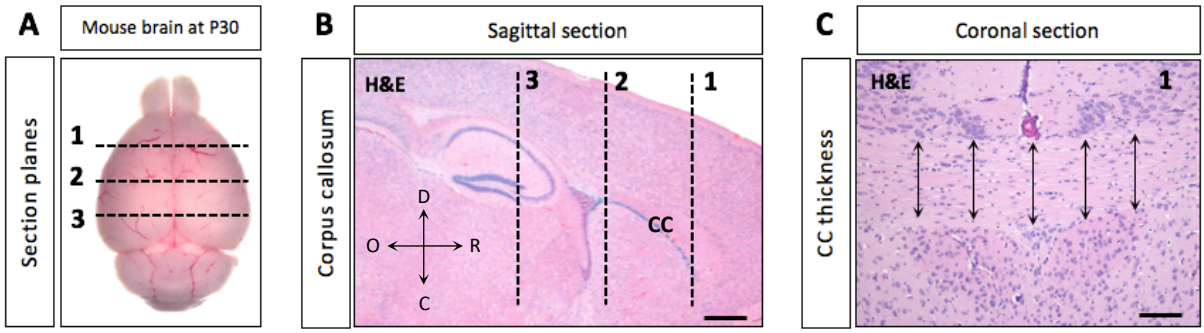

Figure 9: Stereological approach for estimating the corpus callosum thickness. (A) Top view on a mouse brain of a control animal at P30 displaying coronal section planes **(B)** Section planes projected on a sagittal section in a view from medial and running through the corpus callosum (CC). **(C)** High resolution image of the coronal section no° 1 in brain midline with repeated measurements of the corpus callosum thickness. Directions: caudal (C), dorsal (D), occipital (O), rostral (R)*; Scale bar: 800 µm (B), 100 µm (C)*

3.3.2 3D cell volume reconstruction of layer V giant pyramidal cells

The z-stacks acquired through confocal microscopy were further analysed through custom-written MATLAB (MathWorks) analysis and use of the microscopy image analysis software Imaris (Bitplane). It was utilized to conduct 3D reconstructions of neocortical layer V giant pyramidal cells (Fig. 10). The volumes of these reconstructed cells were then used for investigating differences in neuron cell size between trial and control group. The process of reconstruction included the following steps: First, the z-stacks were imported to Imaris that recognized the

NeuroTrace and Hoechst stained tissue as a multitude of voxels of two different colors when the voxel's color intensity surpassed the 90th percentile of intensity as a minimal threshold. Voxels with color intensity levels below these thresholds were colored black and defined as free space. This step was executed to reduce background noise. Afterwards contiguous turquoise voxels (Hoechst) were defined as cell cores. Magenta voxels (NeuroTrace), that were defined as soma, were then assigned to the respective closest core. The distances from soma voxels to the different cores were identified by simultaneously projecting multiple spheres with raising radius around the cores on which the soma voxels came to lie. Then soma voxels were automatically assigned to the corresponding sphere's core. When coming to lie on more than one sphere of different cores the sphere with the smallest radius was chosen. Cores and assigned soma voxels were then defined as cells and their volume was measured. To reduce the number of incorrect allocations and therefore falsely reconstructed cells thresholds for core volume size and cell volume size were implemented. Consequently, smaller cells like glial cells were excluded. Furthermore, cells that were located close to or touching the sections' margins were also excluded. Finally, falsely reconstructed cells, such as fused cells - when two or more cores were defined as one by the algorithm - or structures like cut and stained vessels that had falsely been defined as cell cores, were excluded manually after the reconstruction process.

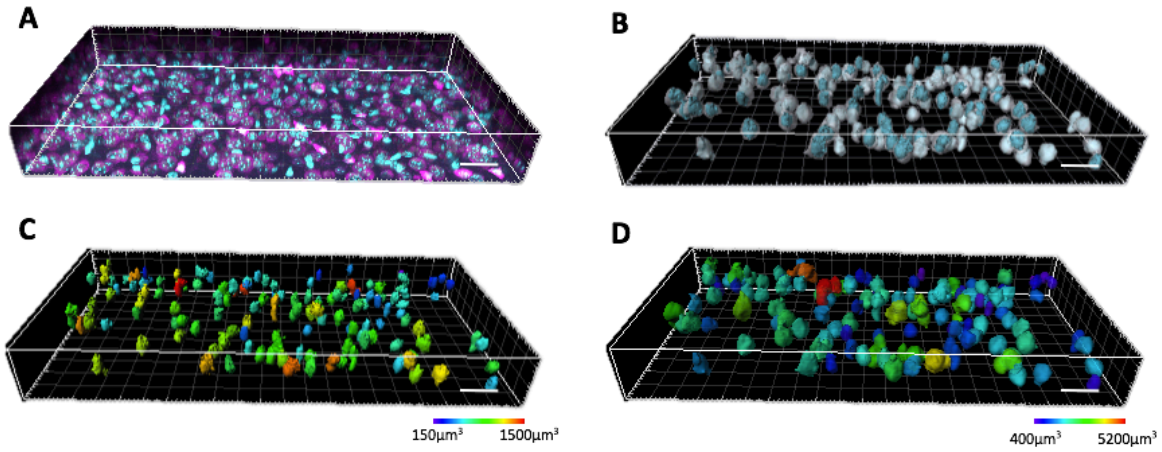

Figure 10: 3D Cell reconstruction of layer V giant pyramidal cells using Imaris. (A) Z-stack of a NeuroTrace (magenta) and Hoechst (turquoise) stained section as displayed by Imaris after stack acquisition and adjustment using a Zeiss LSM780 confocal microscope and Zen imaging software. **(B)** Imaris 3D cell reconstruction with differentiation of cell cores (blue) and soma (gray) before manual selection. **(C)** Cell cores and **(D)** cell bodies with a color volume gradient that was used for identifying possible reconstruction mistakes for manual exclusion. *Scale bar (white): 40 µm (A, B, C, D)*

3.4 Human data

To evaluate the structural findings in *hGFAPcre::CBP$^{Fl/Fl}$* transgenic mice and to assess the validity of this mouse line as a mouse model for Rubinstein-Taybi syndrome a series of cerebral measurements in cranial MR image sets from RTS patients was conducted. Furthermore, the gene mutation type- and localisation distribution in a larger number of published RTS cases was analysed to compare it to the truncated CBP^{stop523} variant expressed in used the mouse model.

3.4.1 Acquisition of cranial MRI data sets from RTS patients

For this study only pre-existing MRI data was used, therefore no direct patient contact or uncomfortable and compromising examination was necessary. Only RTS patients with a molecular-genetically assured diagnosis were included. The procedure and study design were approved by the ethics committee of the LMU faculty of medicine. The parents of RTS patients of the medical centre of the University of Munich or the kbo Children's Centre Munich were formally contacted and informed about the study. They were subsequently asked for their consent to request MRI data from external institutes and to include this data in the study in a pseudonymised manner. The children's age at the time of MRI imaging ranged from one month to five years. Acquired data was stored in hard copy and digitally in the computerized data bank of the Institute for clinical radiology of the LMU university clinic.

3.4.2 Measurement of structural parameters

All measurements were conducted in T2 weighted images. They were repeated several times for each parameter and averaged to reduce variability. They include measurements of the corpus callosum (length, genu thickness and splenium thickness), the lateral ventricles (anterior and posterior horn thickness), cerebral diameters and the distance between the frontobasal plane and the sella floor. Cerebral diameters were measured at the level of the interventricular foramen. Both maximal anterior-posterior and left-right - at the level of the anterior and posterior horn of the lateral ventricle - diameters were determined. Analogue measurements were conducted with cranial MRI data from age matched controls selected from the database of the institute of radiology to perform matched-pair statistical analysis.

3.4.3 Gene mutation type & location in published cases of RTS

To further investigate the role of the HAT and other domains of the CBP gene for the development of RTS, 193 published cases of RTS listed in the Human Gene Mutation Database (Qiagen Bioinformatics) were organized by type and localisation of the pathogenic mutation (table 3). A focus was put on point mutations for a more precise allocation concerning different domains and exons. For comparisons number of point mutations per 100 bp (base pairs) rates were calculated for exons, certain domains or regions of interest to take the different region sizes into account. Cases in which the pathogenic mutation did not lie within the CBP gene's exons were not included.

Type of mutation	**No° of reported cases**
Point mutations	97
Duplications, Insertions & Indels	34
Small deletions	62
Large deletions (not used)	59
Missense mutations in the entire gene	54
Missense mutations in HAT domain	36
Missense mutations in exons 1-17 (before HAT domain)	9
Nonsense mutations in the entire gene	43
Nonsense mutations in HAT domain	16
Nonsense mutations in exons 1-17 (before HAT domain)	21

Domain or gene region of interest	**Exons**	**Segment length [bp]**	**No° of point mutations**	**No° of point mutations per 100 bp**
HAT-domain	18-29	1521	52	3,42
Non-HAT	1-17, 30, 31	5808	45	0,775
Non-HAT, non-Q	1-17, 30	3714	34	0,915
before HAT	1-17	3369	30	0,89
Kix-domain	5-9	725	9	1,24
Non-Kix	1-4, 10-31	6599	88	1,334
Non-Kix, non-Q	1-4, 10-30	4442	77	1,733
Non-Kix, non-HAT, non-Q	1-4, 10-17, 30	2926	25	0,85
Q domain	31	2157	11	0,51
Non-Q	1-30	5172	86	1,663
Exon 2	2	713	6	0,84
Non-Exon 2	1,3-31	6616	91	1,38
Non-Ex. 2, non-HAT, non-Q	1,3-17,30	2938	27	0,92
Entire gene	1-31	7329	97	1,32

Table 3: Excerpt of mutation type and distribution in RTS cases (HGMD, QIAGEN)

3.5 Statistical analysis

Statistical analysis was conducted with Prism 5.0 and 6.0 software (Graphpad). The level of significance was defined at 5% with a two-sided p-value for all tests used. Consequently, a p-value of <0.05 indicated a significant difference between the compared groups regarding the respective parameter tested. In these cases, the null hypothesis - that there was no significant difference between the compared groups - was rejected. If not stated differently results are shown graphically as mean value of the respective group ± SEM (standard error of mean).

3.5.1 Kaplan-Meier survival curves and Log-rank test

Survival rates of *hGFAPcre::CBP*$^{Fl/Fl}$ transgenic mice and control animals are illustrated as Kaplan-Meier curves. Starting with their birth the animals were observed for 100 days. Animals which were sacrificed beforehand were taken into account as drop outs. The survival distributions of the two groups were compared by means of the nonparametric Log-rank test.

3.5.2 Chi-squared test for across gene mutation distribution analysis

The X^2(Chi-squared) test was used for comparing point mutation frequencies of specific domains and regions of the CBP gene. In the respective cases the *no°* of point mutations, missense mutations or nonsense mutations per 100bp were defined as the feature that was distributed between two groups. The region or domain of interest was defined as the first group and the rest of the gene or another region was defined as the second group.

3.5.3 Parametric testing for differences between two groups

Assuming approximate Gaussian distribution of the statistical population in the in vivo situation from which the collected data had been derived, parametric tests were used to analyse for differences between groups. For comparing the transgenic mice with the control group regarding different aspects the unpaired *t*-test was used. The same accounts for analysis of the buried food and light/dark box test. Further, a two-way repeated measurements ANOVA test and Bonferroni's multiple comparisons post hoc test as well as nonlinear regression using an exponential decay model were applied for evaluation of the habituation test. For comparing the MRI measurements, the paired *t*-test was used as for each RTS patient images of healthy children of the same age were analyzed.

4. Results

4.1 Mutation types and location in the CBP gene of RTS patients

In the *hGFAPcre::CBP*$^{Fl/Fl}$ transgenic mice a truncated *CBP*^{Stop523} version of the wild-type CBP, with a missing HAT domain, is expressed. So, the question arose whether this kind of truncation with a loss of the HAT domain could be a typical RTS cause also in humans. It is suggested that mutations in the HAT domain which go along with a reduction of HAT activity are sufficient for the development of RTS[223]. To verify the major role of diminished HAT activity in RTS pathogenesis the mutation distribution in published RTS cases was analysed focusing on HAT domain mutation or loss and the frequency with which these were the sole cause for the development of RTS compared to mutations in other regions of the CBP gene.

4.1.1 Pathogenic mutations are not distributed equally within the CBP gene

Associating the published cases of RTS-triggering point mutations, duplications, insertions, indels and small deletions to the respective affected exon suggests an inhomogeneous distribution with a peak in exons belonging to the HAT domain. In line with previous findings[7], subsequent statistical distribution analysis of point mutations per 100bp shows that there are significantly more point mutations leading to the development of RTS in the HAT than in other domains or regions. By contrast, the C-terminal Q domain contains significantly less disease-causing point mutations per 100bp than the rest of the gene. Point mutation freuquency for KIX domain and Exon 2 - which was previously described as an instable region for harboring translocation and inversion breakpoints[41] - did not differ from the rest of the gene (Fig. 11).

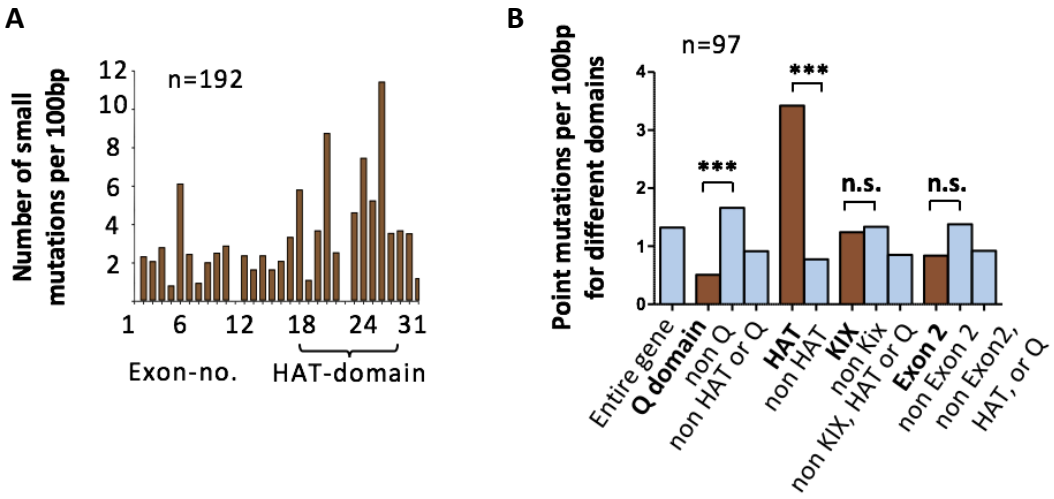

Figure 11: Inhomogeneous mutation distribution in the CBP gene in published RTS cases. (A) Point mutations, duplications, insertions, indels and small deletions as mutations per 100bp sorted by affected exons with a visible peak of mutations within the HAT domain (Exons 18-29; in total 52 out of the 192 published RTS cases). **(B)** Point mutations per 100bp distribution analysis comparing different domains and regions of interest. The HAT domain was shown to harbor significantly more RTS causing point mutations than the rest of the gene and the C-terminal Q domain significantly less. ***p < 0.01, ***p < 0.001*

4.1.2 Loss of HAT domain function plays a distinct role in RTS exegesis

Previous findings suggest that most RTS causing mutations in the CBP gene lead to a premature translation stop with a stable but not functioning, truncated product[7,19]. To further investigate the role of reduced histone acetyl transferase activity in the development of RTS, missense and nonsense mutation frequencies within HAT domain and in exon 1-17 (before HAT domain) were compared. Nonsense mutations are bound to lead to a translation stop and subsequently to a loss of the HAT domain whereas missense mutations before the HAT domain could also lead to stable but dysfunctional proteins where the HAT domain was still intact. Distribution analysis of 97 RTS causing missense & nonsense mutations showed that significantly more missense mutations are located in the HAT domain than in exon 1-17, while no significant clustering of nonsense mutations was observed. Accordingly, a significantly bigger percentage of all reported missense mutations compared to the percentage of all nonsense mutations (66.67% to 37.21%) where found within the HAT domain. In line with this, the percentage of all reported nonsense mutations in exons 1-17 were significantly higher than the respective percentage of missense mutations (48.84% to 16.67%) (Fig. 12). Thus, suggesting that point mutations in exons 1-17 are more likely to cause RTS when being nosense mutations that lead to a a loss of HAT activity.

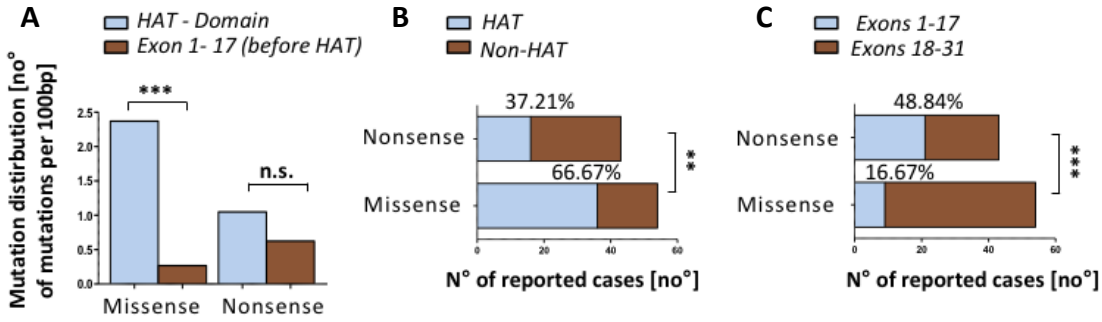

Figure 12: Predominant role of the loss of HAT domain function in published RTS cases with CBP mutations. **(A)** Missense and nonsense mutation distribution between HAT domain and exon 1-17 (before HAT domain) as mutations per 100bp **(B)** Comparison of nonsense and missense mutation counts in the HAT domain as percentage of all reported cases **(C)** Comparison of nonsense and missense mutation counts in exons 1-17 as percentage of all reported cases. n_1 (nonsense mutations) = 43, n_2 (missense mutations) = 54; ***p < 0.01, ***p < 0.001*

4.2 General characteristics of conditional CBP knock-out mice

4.2.1 *hGFAPcre::CBP$^{Fl/Fl}$* mice have a higher 30 day mortality and lower brain weight

Non-conditional homozygous CBP-deficient mice die around E10 during embryonal development[73,232]. A comparable increase in embryonal mortality was not observed for *hGFAPcre::CBP$^{Fl/Fl}$* mice. However, a higher 30-day mortality compared to control animals or heterozygous knock-out animals was measured. The survival curve for *hGFAPcre::CBP$^{Fl/+}$* heterozygous animals did also show a trend towards an increase in mortality during a 100 day observation period, although not statistically significant in comparison to the control group. While non-conditional heterozygous mutants exhibit skeletal abnormalities that correspond closely with those typical for RTS patients[224,225], neither homozygous nor heterozygous conditional knock-out mice where distinguishable from control litter mates by their appearance and their body weight at P30 did not differ significantly. Brain weight at P30 on the other hand, was significantly lower both in *hGFAPcre::CBP$^{Fl/Fl}$* and *hGFAPcre::CBP$^{Fl/+}$* mice (Fig. 13).

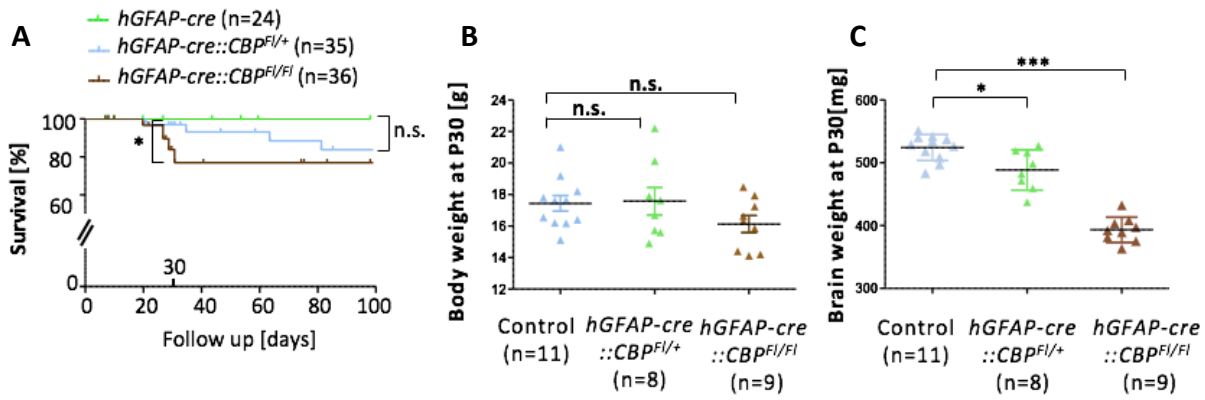

Figure 13: General characteristics of conditional CBP knock-out mice. **(A)** Survival curves for mutant and control groups with a follow up duration of 100 days. Drop outs are depicted as decimal points in the respective curves. **(B)** Body weight at P30 measured shortly before killing. **(C)** Brain weight at P30, determined after preparation. **p < 0.05, ***p < 0.001*

4.2.2 Structural brain abnormalities in overview sections

For general examination of forebrain structures, sagittal H&E stained sections of recently born (P0) and thirty-day-old (P30) animals from the different groups were compared. Except the tendency towards a dysmorphic cerebellum in P0 animals which could not be found at P30 and possibly smaller hippocampi at P30 no consistent and definite differences between heterozygous conditional knock-out mice and control animals could be observed. In contrast, homozygous

knock-out mice exhibited a clearly visible smaller hippocampus at P30, a disruption of the rostral migratory stream (RMS) in form of an apparent cell accumulation, and a diverging architecture of the olfactory bulb (OB), beside a dysmorphic cerebellum at all ages. For determining the efficiency of the CBP knock-out, sections were stained immunohistochemically with a C-terminally binding CBP antibody that did not react with the truncated murine CBP in cells of the used transgenic mice. In those cells expressing GFAP during development, like neurons of the hippocampus[233,234] or neocortex[99,111,235], reduction of CBP expression in heterozygous and a complete loss in homozygous knock-out animals was confirmed (Fig. 14). Furthermore, dilated lateral ventricles could be observed in frontal sections at P30 (see Fig. 16). Besides, MBP - myelin basic protein, an extrinsic myelin membrane protein[236] - staining did not show differences in myelination in *hGFAPcre::CBP$^{Fl/Fl}$* mice at different time points (App. 1).

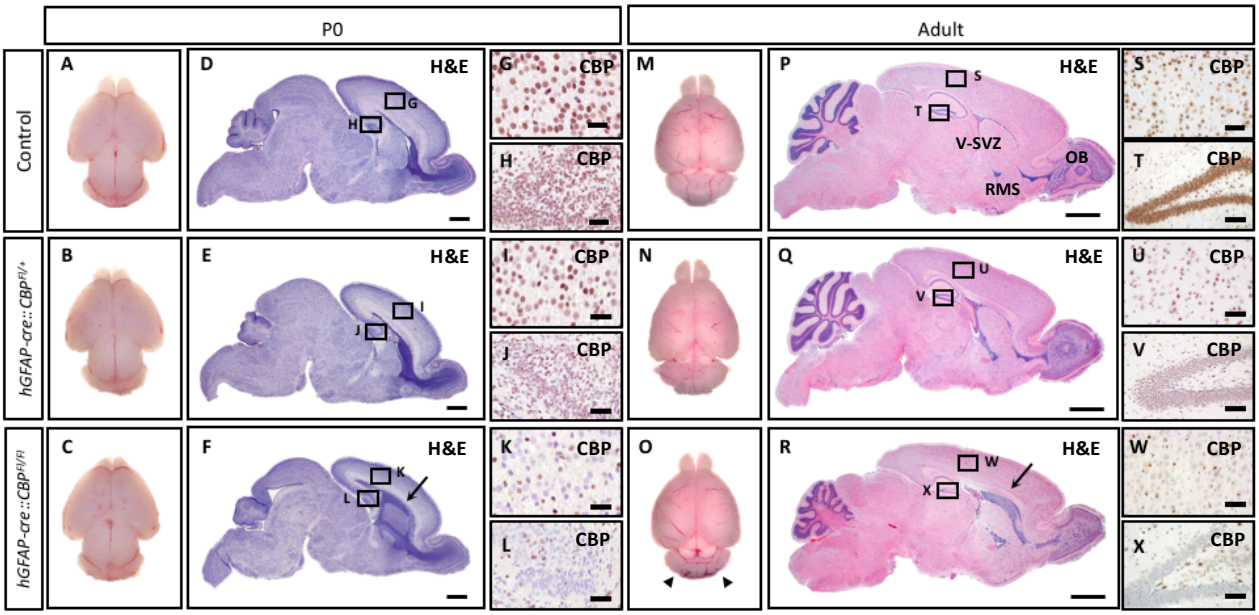

Figure 14: Structural brain abnormalities in overview sections of conditional CBP knock-out transgenic mice. **(A-C, M-O)** Images of murine brains after preparation of transgenic and control animals at P0 and P30. The dismorphic cerebellum of a P30 homozygous knock-out mouse is marked with arrowheads **(O). (D-F, P-R)** Sagittal H&E stained sections through the rostral migratory stream (RMS) at P0 and P30 display aberrations of the cerebellum, hippocampus, RMS and olfactory bulb (OB) in *hGFAPcre::CBP$^{Fl/Fl}$* mice. Arrows mark a region in the RMS with a cell accumulation close to the ventricular-subventricular zone (V-SVZ) **(F,R). (G-I, S-X)** Magnifications of CBP stained regions of the hippocampus and neocortex displaying the reduction of CBP expression in the conditional knock-out mouse model. *Scale bar: 900 µm (D-F),75 µm (S-L),1800 µm (P-R), 100 µm (S-X)*

4.3 Corpus callosum (CC) development

Consisting of axonal fibers which connect the right and left hemisphere, the corpus callosum plays an important role in the integration of information between different areas of the forebrain. Recent findings suggest that corpus callosum agenesis, hypoplasia or dysplasia relate to impairment of cognitive functions[237,238]. Corpus callosum dysgenesis or agenesis was also found repeatedly in RTS patients[239,240,241].

4.3.1 Early CBP depletion leads to decrease in corpus callosum midline thickness

Corpus callosum midline thickness was measured at P15 and P30 in transgenic and control animals in H&E stained frontal sections. It was found to be significantly thinner at both time points in the transgenic mice suggesting a disturbed corpus callosum development (Fig. 15).

4.3.2 Cell migration from the V-SVZ to the CC is disrupted in *hGFAPcre::CBP$^{Fl/Fl}$* postnatal mice

A recent work showed that astroglial progenitor cells travel from the ventricular-subventricular zone to the corpus callosum in the adult organism[242]. To investigate this process in *hGFAPcre::CBP$^{Fl/Fl}$* mice a BrdU fate-mapping approach was employed where BrdU was injected at P15 and preparation was performed 15 days later. At P30 a significantly reduced percentage of BrdU+ cells in the genu of the corpus callosum were measured in transgenic mice compared to the control group (Fig. 15). In the same setting, no differences in the proliferation- or apoptosis rate within the V-SVZ or CC were observed at P15 suggesting that indeed cell migration from the V-SVZ to the corpus callosum is impaired (App. 2 & 3).

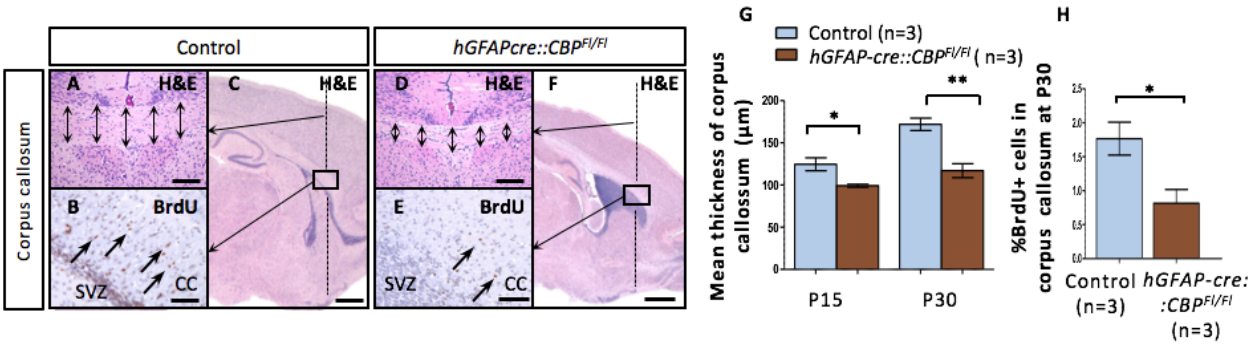

Figure 15: Corpus callosum development is impaired in *hGFAPcre::CBP$^{Fl/Fl}$* mice. **(A,D)** Exemplary repeated CC thickness measurements at P15 in frontal sections of the CC with the section plane indicated in sagittal sections **(C,F)**. **(B,E)** BrdU staining of the CC genu in sagittal sections at P30 after BrdU injection at P15. BrdU+ cells in the CC are labelled with arrows. **(G)** Midline thickness of the corpus callosum is significantly smaller in *hGFAPcre::CBP$^{Fl/Fl}$* mice at P15 and P30. **(H)** A significantly lower percentage of BrdU+ cells were observed in the corpus callosum at P30 after BrdU injection at P15. *Scale bar: 160 µm (A,D), 200 µm (B,E), 2200 µm (C,F); , *p < 0.05, **p < 0.01*

4.4 Neocortical development

4.4.1 Early loss of CBP leads to an impairment in postnatal neocortical growth

Following embryonal development, the neocortical thickness in postnatal mammals increases further, whereby a continued rise in the number of neocortical neurons and glial cells can be observed[243,244]. To investigate the postnatal neocortical development of *hGFAPcre::CBP$^{Fl/Fl}$* mice and to look for structural alterations a mean neocortical thickness was determined at different time points in the region neighbouring the hippocampus. For each animal, repeated measurements where conducted and averaged at three levels in different section planes. While at P0 the mean neocortical thickness did not differ from the control group, the neocortex was found to be significantly thinner in animals aged 20 or 30 days (Fig. 16).

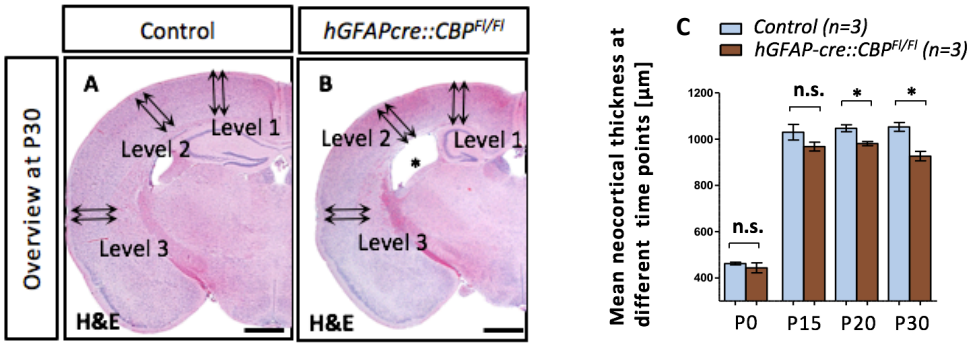

Figure 16: Neocortical thickness at different ages. **(A,B)** Frontal H&E stained matched sections in the area of the hippocampus in which neocortical thickness was measured repeatedly at different levels. A dilated lateral ventricle is marked with a star (*). **(C)** Mean neocortical thickness did not differ significantly at P0 between control and transgenic mice. In older animals mean neocortical thickness was found to be significantly smaller in *hGFAPcre::CBP$^{Fl/Fl}$* animals aged 20 or 30 days. At P15 a tendency was visibile that did not produce statistical significant differences due to heterogeneity in the control group. *Scale bar: 1300 µm (A, B); *p < 0.05*

4.4.2 *hGFAPcre::CBP$^{Fl/Fl}$* mice develop a normal architecture of the neocortex with six distinguishable laminae

To further investigate the postnatal neocortical development in the transgenic mice, cytoarchitecture, proliferation-rate, apoptosis-rate and neural differentiation were examined in the neocortex and ventricular zone at different ages between P0 and P30. At all time points a classical structure with six laminae was apparent and no differences in proliferation or apoptosis could be observed. This is in line with previous findings in a mouse model with conditional CBP knock-out in post mitotic principal neurons of the forebrain[245]. Concerning neural differentiation,

though no difference in the density of NeuN positive neurons was measured, the transgenic mice's neurons appeared smaller and dysmorphic especially in lamina V of the neocortex (Fig. 17; App. 4 & 5). Besides, using antibodies against MAP2 - a microtubule regulating dendritic protein important for neurite stability[246,247] - and synaptophysin - a synaptic vesicle glycoprotein[248] - for immuno-histochemical staining, no differences in neurite development were revealed suggesting architectural integrity (App. 6).

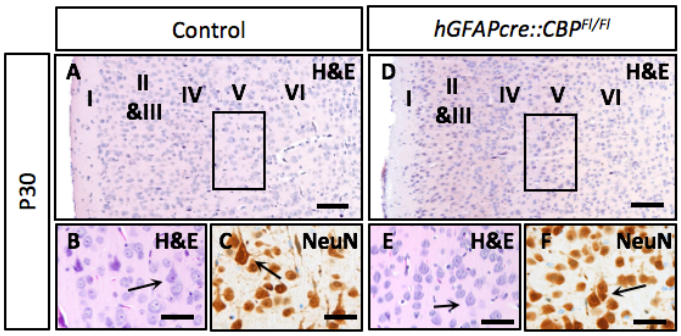

Figure 17: Neocortical organization and neural differentiation at P30. (A,D) Frontal section of the neocortex architecture and formation of the six neocortical laminae (I-VI) with magnification of Layer V at P30 **(B,E). (C,F)** Neural differentiation in layer V of the neocortex, made visible through NeuN staining. Arrows mark lamina V giant pyramidal cells that appeared to be smaller and dysmorphic in transgenic mice. *Scale bar: 130 µm (A,D), 50 µm (B,C,E,F)*

4.4.3 3D reconstruction suggests that CBP lacking giant pyramidal cell neurons of lamina five have a reduced cell volume

To shed more light on the influence of early loss of CBP on the development and differentiation of neocortical neurons on a more cellular level 3D reconstruction of lamina V giant pyramidal cells was conducted. This cell population was chosen due to its cell size and relatively low density in lamina V that allowed an automated process of set stack analysis using Imaris. All animals were sacrificed at P30. After reconstruction and volume measurement, on the one hand, volume distribution curves for the two groups were generated. On the other hand, mean volume values were determined for each animal for more direct comparison between control and *hGFAPcre::CBP$^{Fl/Fl}$* groups. Statistical testing of mean volume values resulted in significant lower neuronal cell volume of transgenic mice. Supporting this finding, the volume distribution curves for the two groups differed and displayed a shift of the *hGFAPcre::CBP$^{Fl/Fl}$* mices curve towards smaller volumes (Fig. 18). This implicates that differentiation and development is disturbed in neocortical precursor cells lacking CBP, while not being inhibited completely.

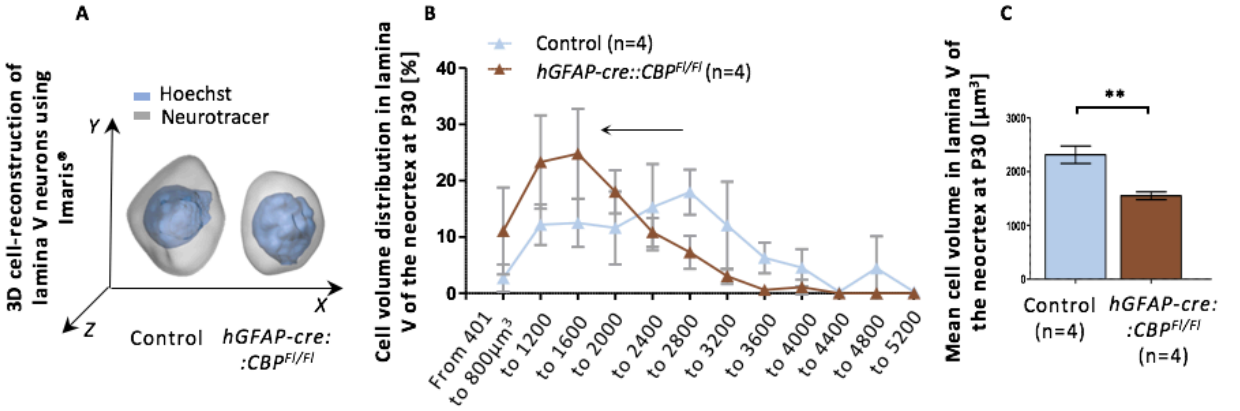

Figure 18: Lamina V cell reconstruction and volume analysis. **(A)** Exemplatory 3D cell reconstruction of Lamina V giant pyramidal cells from hoechst and neurotracer stained 100 µm sections using z-stacks acquired through confocal microscopy and Imaris. **(B)** Cell volume distribution curves with rates of cells within a certain volume range. Error bars indicate inter-individual differences. The curve for neurons from the *hGFAPcre::CBP$^{Fl/Fl}$* group is shifted to the left towards smaller cell volumes. **(C)** Determined mean cell volume in the lamina V of the neocortex at P30 was found to be significantly smaller in the transgenic mice compared to control litter mates. ***p < 0.01*

4.4.4 Early CBP knock-out leads to reduced proliferation- and increased apoptosis-rates in the ventricular zone during embryonal development.

Embryonal neocortical development was investigated at E14.5 and E16.5 (embryonal age of 14.5 and 16.5 days after conception). First it was confirmed that CBP knock-out was effective and that both ventricular zone stem cells at E14.5 as well as cells that migrated earlier were affected. Subsequent overview H&E staining of frontal sections at these time points showed no clearly visible differences between control and knock out animals concerning the constellation of ventricular zone and neocortex. Sox2 staining was then used to verify that cells in the ventricular zone of *hGFAPcre::CBP$^{Fl/Fl}$* exhibit a pluripotent neuronal stem cell character, too[249,250]. Furthermore, no differences in proliferation or apoptosis were observed within the already formed neocortical cell layers (App.7). In the VZ, however, differences between the two groups were found concerning both proliferation and apoptosis. The proliferation rate was observed to be significantly reduced in transgenic animals both at E14.5 and E16.5, what was validated statistically in BrdU and EdU stained frontal sections, whereby BrdU was injected 2h before preparation of the pregnant animals at E14.5 and EdU in an analogous manner at E16.5. The apoptosis rate was found to be significantly increased in the ventricular zone of *hGFAPcre::CBP$^{Fl/Fl}$* mice at E16.5, while no difference was found at E14.5 (Fig. 19). These results were supported by a significantly thinner ventricular zone at E16.5 measured in Sox2 and Ki67 stained frontal sections (Fig. 19; App. 7).

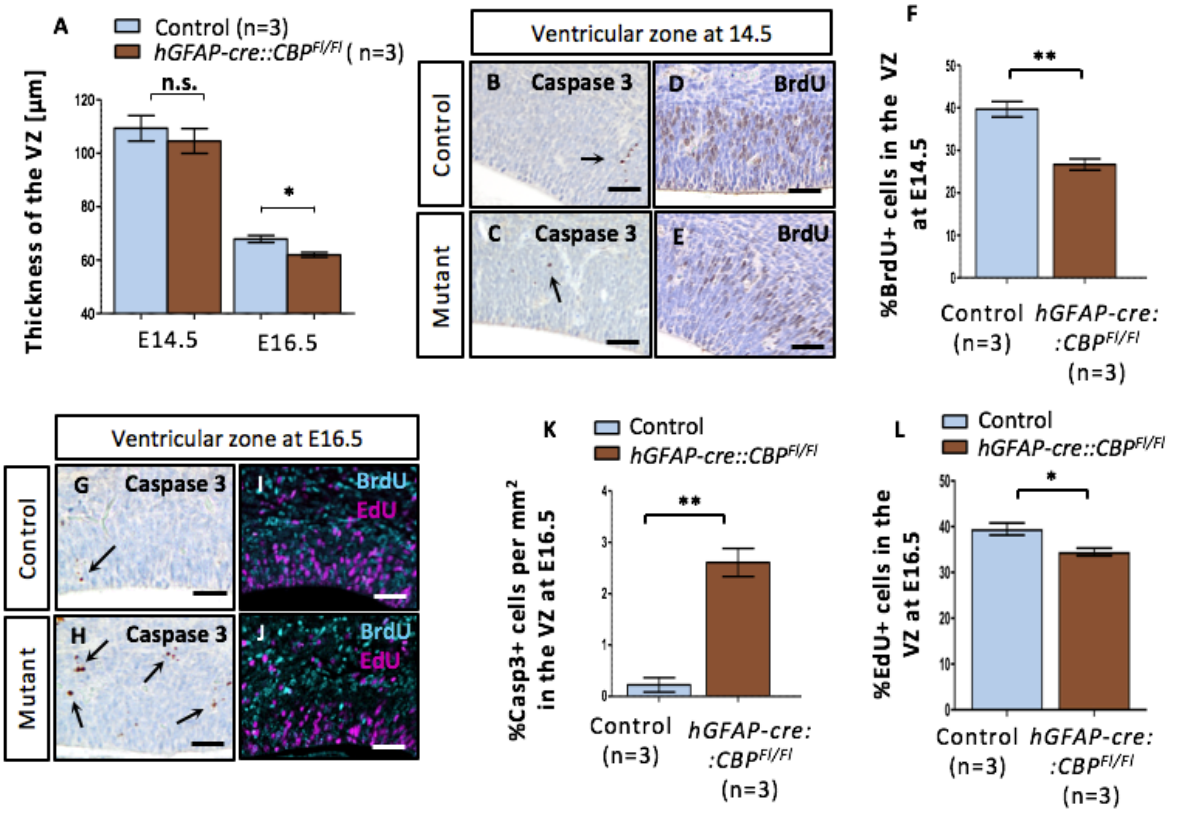

Figure 19: A *hGFAPcre::CBP$^{Fl/Fl}$* genotype leads to alteration of proliferation- and apoptosis-rates in the ventricular zone during embryonal development. (A) Ventricular zone thickness is significantly reduced at E16.5 in transgenic mice with measurements conducted in Sox2 and Ki67 stained frontal sections (App.7). **(B,C)** No significant amount of Caspase 3+ apoptotic cells was found in the ventricular zone at E14.5. **(D,E,F)** The percentage of BrdU+ cells as a marker of proliferation within the ventricular zone at E14.5 were shown to be significantly lower in *hGFAPcre::CBP$^{Fl/Fl}$* animals compared to control litter mates. **(G,H,K)** A significant rise in apoptosis rates within the ventricular zone of transgenic mice was measured at E16.5. **(I,J,L)** A diminished proliferation rate of ventricular zone stem cells was confirmed also at E16.5 in EDU 2h injected animals. Here BrdU had been injected at E14.5 for migration analysis (see 4.4.5). *Scale bar: 50 µm (B-E,G-J), *p < 0.05, **p < 0.01*

4.4.5 Radial migration during neocortex development is impaired when CBP is knocked out in neural progenitor cells.

For assessing the migration process of neural precursor cells during neocortex development at embryonal stages a BrdU/EdU double pulse fate-mapping approach was used. Proliferating cells in the ventricular zone were marked with BrdU at E14.5 and tissue analysis was conducted at E16.5 after those cells traveled radially to form the neocortical layers. Additionally, a EdU pulse was administered two hours before sacrifice to differentiate cells that had migrated to their current location from stationary proliferating cells. BrdU+ rates did not differ significantly in statistical testing between control and transgenic animals in the respective areas of the

ventricular zone, the intermediate migration area and the area of destination after the two days of migration. However, to more accurately evaluate cell migration, the averaged percentage of those BrdU+ cells which reached their destination, hence the outer neocortical layers, compared to all BrdU+ cells that left the ventricular zone was determined. Here, a statistical significant difference between the two groups was observed, suggesting that in fact, less migrating cells reached the outer neocortical layers when CBP was knocked out in ventricular zone precursor cells. The second analysis was employed as solely examining the BrdU+ rate was considered to be vulnerable to confounding variables such as variable cell density and the earlier observed differences in apoptosis- and proliferation rates that were bound to have led to reduced total cell counts in the *hGFAPcre::CBP*$^{Fl/Fl}$ group. In a setting in which only the percentage of BrdU+ cells of the total cell count is determined, reduced total cell counts would mask a factual reduction of BrdU+ cells. (Fig. 20).

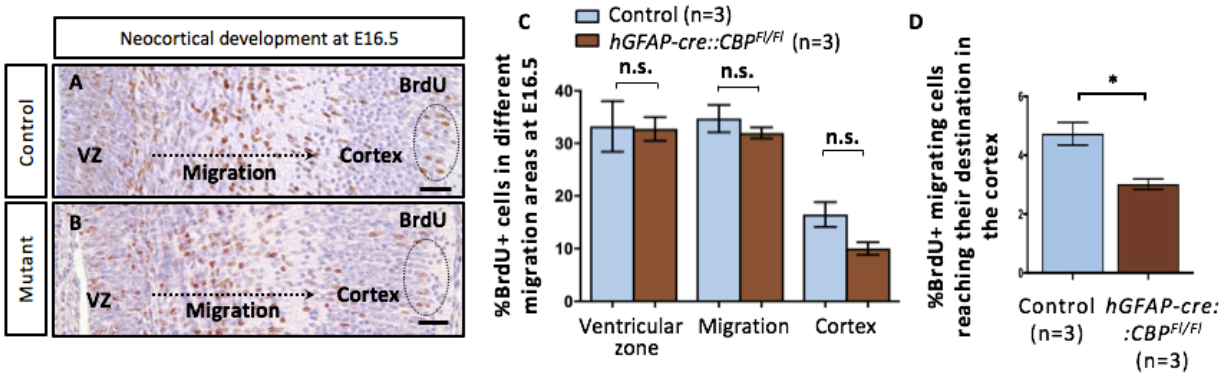

Figure 20: Impairment of radial migration during neocortex development after early CBP knock-out. **(A,B)** Frontal section overview over the migration process from the ventricular zone to the outer neocortical layers which are marked with circles. BrdU was injected at E14.5 labeling proliferating and then migrating cells in the ventricular zone. **(C)** BrdU+ rate in the different migration areas after two days of migrating with no statistical significant difference between control and transgenic mice. **(D)** Percentage of BrdU+ cells that reached the circled outer layers of the neocortex compared to all BrdU+ cells that left the ventricular zone, with a statistical significant difference between the two groups, suggesting that less migrating cells reach their destination in *hGFAPcre::CBP*$^{Fl/Fl}$ animals during the period between E14.5 and E16.5. *Scale bar: 50 µm (A,B), *p < 0.05*

4.5 Hippocampus development and adult neurogenesis

4.5.1 Early CBP depletion leads to an underdeveloped hippocampus and a reduction of neurogenesis in the dentate gyrus of adult animals

Frontal, H&E stained overview sections of the hippocampus showed a clearly dysmorphic and smaller hippocampus in *hGFAPcre::CBP*$^{Fl/Fl}$ animals. Thickness measurements of the dentate gyrus at different time points delivered similar results to those in the neocortex. While at P0 the dentate gyrus thickness did not differ between control and transgenic animals, measurements at later time points produced highly significant differences suggesting an impairment particularly of postnatal hippocampal development when CBP is knocked-out (Fig. 21). The general development of the different hippocampal zones cornu ammonis (CA) I-III and the dentate gyrus however, was not halted (see also 4.5.2). To furthermore analyze the effect of early CBP depletion on postnatal neurogenesis in the subgranular zone (SGZ) of the dentate gyrus[251,252], Sox2, Ki67 and Caspase 3 staining were used. Sox2 was shown to be a sensitive marker for hippocampal multipotent stem cells[253]. While no significant amount of apoptosis was detected (App. 8), Sox2+ and Ki67+ rates in the SGZ were significantly reduced at P30 indicating that a lack of CBP leads to a reduction of postnatal neurogenesis in the hippocampal SGZ (Fig. 21).

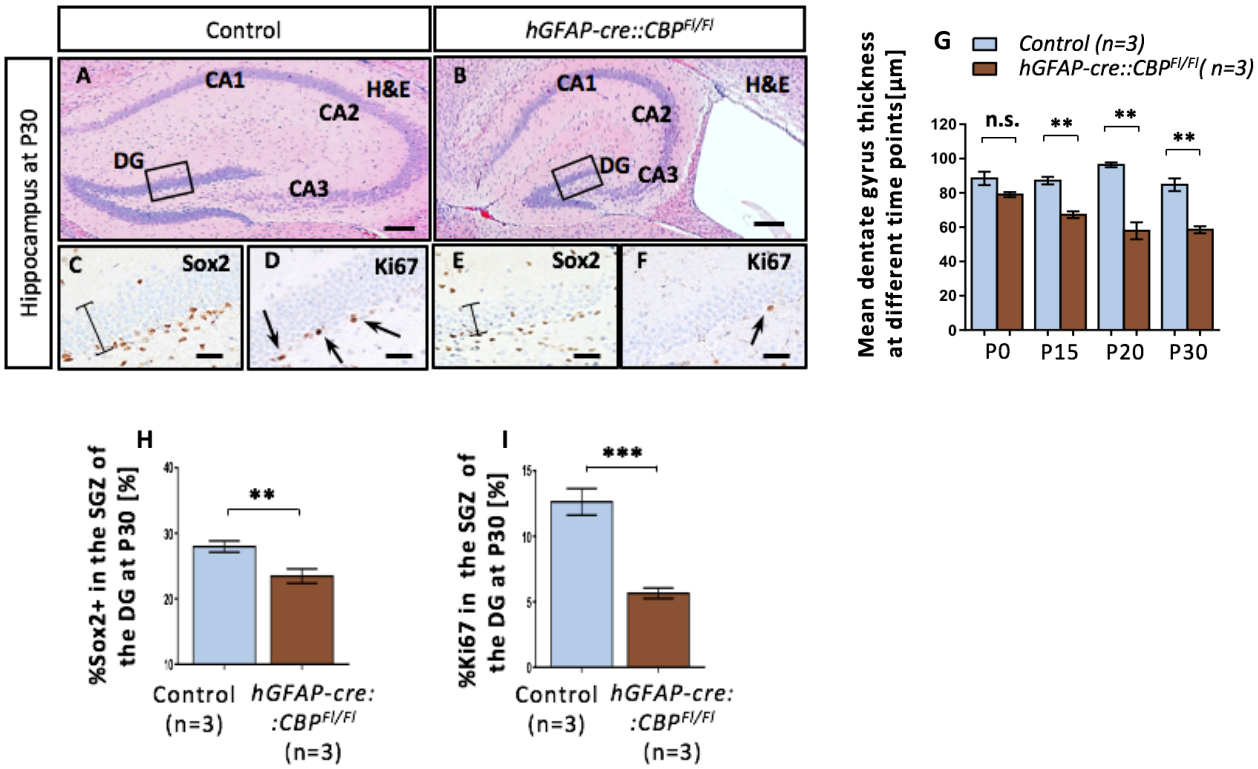

Figure 21: Structural hippocampus alterations in postnatal *hGFAP-cre::CBP$^{Fl/Fl}$* animals and influence on adult neurogenesis. (A,B) Hippocampus overview showing a dysmorphic and smaller hippocampus in transgenic animals. Cornu ammonis I-III (CA1-CA3), Dentate gyrus (DG). **(C-F)** Sox2 stem cell staining and Ki67 proliferation staining of frontal sections through the dentate gyrus was used for analyzing adult neurogenesis. **(G)** No difference was observed concerning the mean dentate gyrus thickness at P0. Averaged thickness measurements of the dentate gyrus at P15, P20 and P30 on the other hand showed a significantly reduced thickness in knock-out animals. **(H,I)** Both the Sox2+ and Ki67+ rate were found to be significantly reduced in the subgranular zone of the dentate gyrus of *hGFAP-cre::CBP$^{Fl/Fl}$* mice at P30. *Scale bar: 150 µm (A,B), 40 µm (C-F); **p < 0.01, ***p < 0.001*

4.5.2 HuB is temporarily translocated to the cell core in hippocampal and neocortical neurons during postnatal development when CBP is missing

To differentiate between cornu ammonis segments, Wfs1 & HuB antibodies were used for immunohistochemical staining of frontal sections of the hippocampus. Wfs1, a transmembrane cation-selective ion channel, was found to be predominantly expressed in neurons of the CA1 segment[254,255]. HuB, a neuronal member of the Hu protein family - a family of mRNA-binding and stabilizing proteins[256,257] - on the other hand, was shown to be specifically and highly expressed in pyramidal cells of the CA3 segment[258]. Compared to control animals no difference in hippocampus segmentation was found in *hGFAPcre::CBP$^{Fl/Fl}$* animals at different postnatal time points (App. 9). However, at P15 a notable increase in HuB concentration in the pyramidal cell nuclei both in the hippocampus as well as the neocortical lamina V was observed in transgenic mice, while in sections from control animals at P15, HuB was mainly detected in the somata of these cells (Fig.22). This phenomenon did not occur at other time points (P0, P5, P20 or P30), suggesting a temporary translocation of HuB to the cell nuclei of neurons lacking CBP (App. 10).

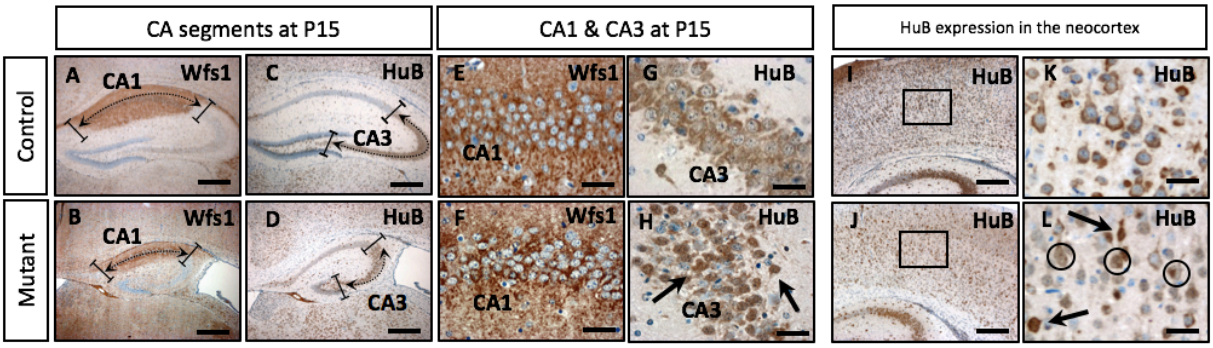

Figure 22: Hippocampal segmentation and HuB expression at P15. (A-D) Cornu ammonis segments CA1 & CA3 made visible through Wfs1 and HuB staining at P15. **(E-H)** CA1 and CA3 close-up with HuB translocation to the cell nuclei of pyramidal cells in *hGFAPcre::CBP$^{Fl/Fl}$* animals indicated by arrows. **(I-L)** HuB expression in the neocortex at P15, particularly lamina V (K,L). Pyramidal cells with HuB detection in the nuclei are emphasized by arrows and circles. *Scale bar: 200 µm (A-D,I,J), 40 µm (E-H,K,L)*

4.5.3 Embryonal hippocampus development is impaired in *hGFAPcre::CBP$^{Fl/Fl}$* transgenic mice

Analogous to the investigation of neocortical development, the time points E14.5 and E16.5 were chosen for the investigation of hippocampus-, and especially dentate gyrus development. First, a complete CBP depletion was shown at both E14.5 and E16.5 in the hippocampal area of *hGFAPcre::CBP$^{Fl/Fl}$* prenatal animals. Second, Sox2 and Prox1 - a homeobox transcription factor[259], inter alia expressed in dentate gyrus precursor cells and essential for dentate gyrus development[260,261] - antibodies were used to confirm an unaltered dentate gyrus granule cell lineage character of the dentate gyrus forming, migrating cells as well as an precursor cell character in the dentate neuroepithelium of transgenic mice despite lacking CBP (App. 11). Regarding structural differences between control and transgenic mice a significantly reduced thickness of the 1ry matrix was found at E16.5 while at E14.5 thickness measurements didn't produce significant differences. Furthermore, area measurements in frontal sections confirmed significantly smaller 2ry and 3ry matrices at E16.5, thus indicating that alterations found in postnatal mice might root in a disturbed prenatal development of the hippocampus (Fig. 23).

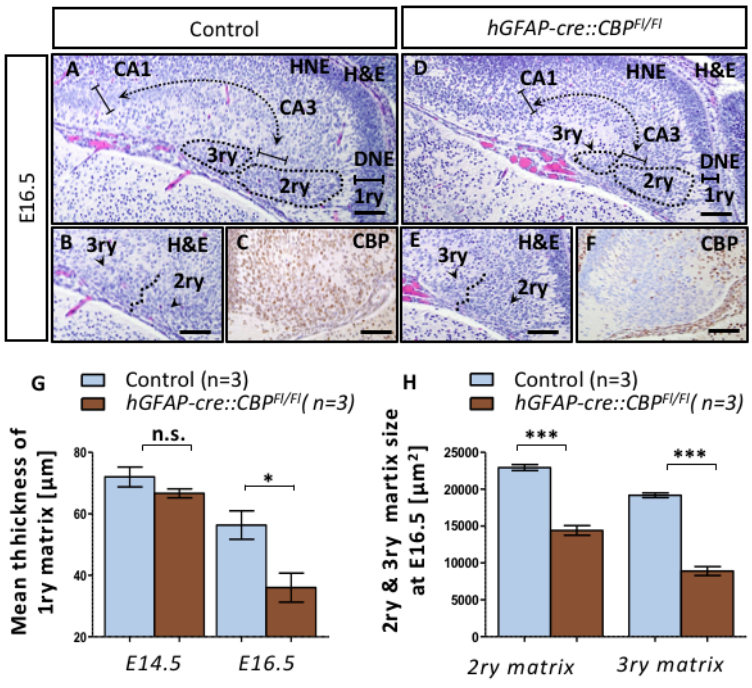

Figure 23: Structural alterations during hippocampal development at E16.5. ***(A,D)*** Overview over hippocampal formation at E16.5 in H&E staining of frontal sections displaying the cornu ammonis (CA1 and CA3), the hippocampal neuroepethelium (HNE), the dentate neuroepithelium (DNE, 1ry) and 2ry & 3ry matrix. **(B,C,E,F)** 2ry & 3ry matrix of the developing dentate gyrus at E16.5 with a complete CBP depletion in both the DNE and in migrating cells. **(G)** The 1ry matrix (DNE) was measured to be significantly thinner in transgenic mice at E16.5, while measurements at E14.5 did not result in significant differences. **(H)** Area sizes of 2ry & 3ry matrix were shown to be significantly reduced in *hGFAPcre::CBP$^{Fl/Fl}$* animals at E16.5. *Scale bar: 50 µm (A-F); *p < 0.05, ***p < 0.001*

4.5.4 CBP depletion leads to alterations in proliferation and apoptosis rates during hippocampal development

To further investigate the cause of the structural alterations found in the transgenic mice, proliferation- and apoptosis rates were determined at E14.5 and E16.5 in different areas of interest using Caspase 3 antibodies for apoptosis- and BrdU & EdU antibodies for proliferation staining. At E14.5, regardless the genotype, no substantial apoptosis was observable in the DNE and no proliferation was seen among the migrating cells in the 2ry matrix. However, while the apoptosis rate in the 2ry matrix did not differ between the two groups, the proliferation rate in the DNE was significantly reduced in those transgenic embryos where CBP was missing (Fig. 24). In this setting, BrdU had been injected into the pregnant mouse 2 hours before sacrifice.

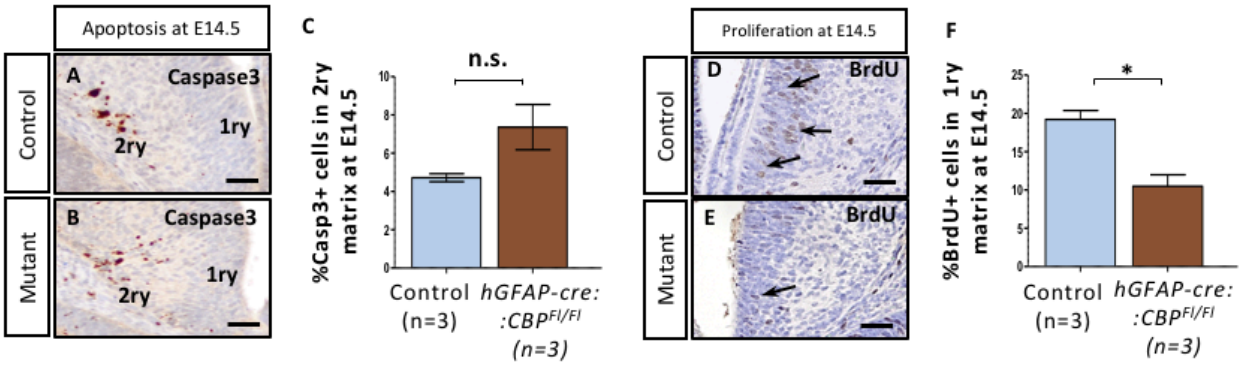

Figure 24: Apoptosis and proliferation during dentate gyrus development at E14.5. (A,B,D,E) 1ry and 2ry matrix in Caspase 3 and BrdU stained frontal sections at E14.5. **(C)** No significant difference in the apoptosis rate among the migrating cells within the 2ry matrix was measured between the two groups. **(F)** Proliferation rate in the 1ry matrix of *hGFAPcre::CBP$^{Fl/Fl}$ mice at E14.5* was measured to be significantly reduced compared to the control group. Scale bar*: 25 µm (A,B,D,E); *p < 0.05*

Analysis of apoptosis- and proliferation rates at E16.5 showed even more extensive effects of CBP depletion. On the one hand, at E16.5 apoptosis was detectable in the 1ry matrix of solely *hGFAPcre::CBP$^{Fl/Fl}$* animals, and at this time point the apoptosis rate was measured to be significantly increased in the area of 2ry and 3ry matrix of transgenic mice, too. On the other hand, while again reduced proliferation was measured in the 1ry matrix of CBP lacking mice, at E16.5 proliferation was also detected in the 2ry and 3ry matrix regardless the genotype. Here a significant reduction of proliferation was again observable in transgenic mice. Proliferation was thereby determined in BrdU/EdU double stained frontal sections with BrdU injection at E14.5 and EdU 2 hours before sacrifice (Fig. 25).

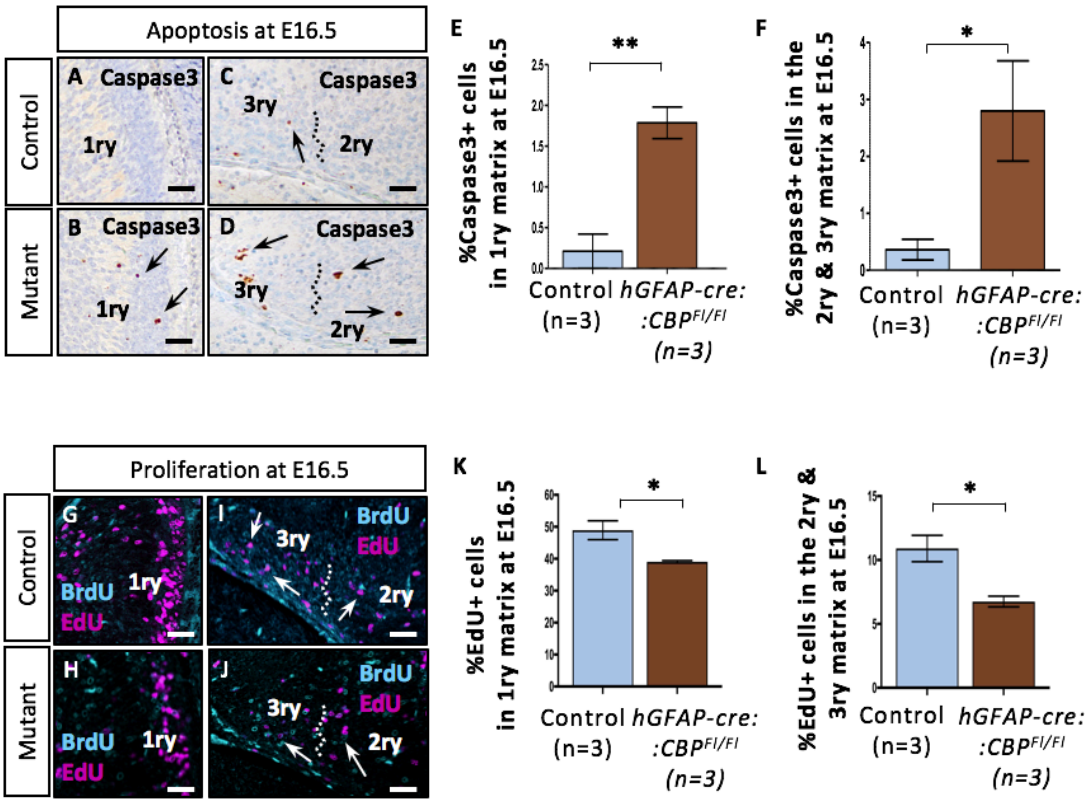

Figure 25: Apoptosis and proliferation during dentate gyrus development at E16.5. (A-C) Caspase 3 apoptosis staining in frontal sections of 1ry, 2ry and 3ry matrix at E16.5. **(E,F)** Significant increase in apoptosis rates was found in the 1ry, 2ry and 3ry matrix of *hGFAPcre::CBP$^{Fl/Fl}$* mice at E16.5 compared to the control group. **(G-J)** EdU proliferation staining and BrdU fate-mapping in frontal sections of the 1ry, 2ry and 3ry matrix at E16.5. Arrows mark EdU+ proliferating cells. No substantial overlap was observed. **(K,L)** Significant decrease in proliferation rates in the 1ry, 2ry and 3ry matrix of *hGFAPcre::CBP$^{Fl/Fl}$* mice at E16.5 was observed compared to the control group. *Scale bar: 25 µm (A-D), 30 µm (G-J); *p < 0.05, **p < 0.01*

4.5.5 Cell migration is compromised during the prenatal development of the hippocampus when CBP is knocked-out at an early time-point

For analyzing migration processes during hippocampus development, the same BrdU/EdU double pulse fate-mapping setting was used as it was for investigations of the neocortex development. BrdU was administered at E14.5 and EdU at E16.5. As no substantial proliferation was observed in the 2ry and 3ry matrix at E14.5, only proliferating cells in the 1ry matrix of the DNE were labeled by BrdU. During the timespan between E14.5 and E16.5 these cells subsequently migrated to the 3ry matrix via the 2ry matrix before the animals were sacrificed and examined. Considering the reduced sizes of 2ry and 3ry matrix in transgenic mice averaged BrdU+ cell counts in the respective areas were analyzed instead of BrdU+ rates. As was

conjecturable, the BrdU cell counts were observed to be significantly lower in *hGFAPcre::CBP$^{Fl/Fl}$* animals. To further reduce the impact of the confounding variable of reduced proliferation in the DNE after CBP depletion the ratio of BrdU+ cells reaching the 3ry to all BrdU+ migrating cells was determined. The ratio was found to be significantly lower in transgenic mice suggesting an impairment of cell migration during hippocampus development after early loss of CBP (Fig. 26). Since no significant overlap was observed in BrdU/EdU double staining in the 2ry and 3ry matrix it is unlikely that the measured effects are explainable solely by differences in further proliferation of the migrating cells after leaving the DNE (see Fig. 25).

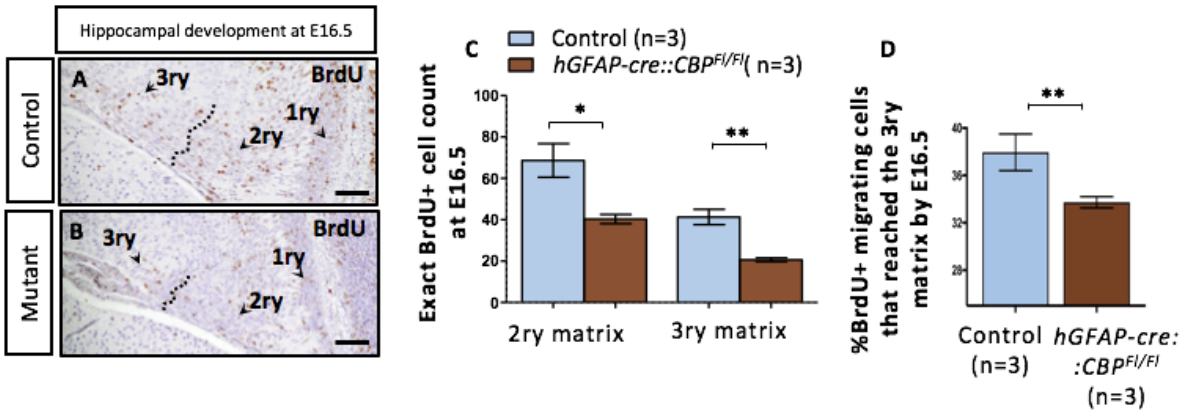

Figure 26: Impairment of precursor cell migration during hippocampus development after early loss of CBP. (A,B) BrdU fate-mapping in frontal sections at E16.5 with BrdU injection at E14.5 displaying the developing hippocampus with 1ry, 2ry and 3ry matrix. **(C)** In line with reduced sizes of the 2ry and 3ry matrix the BrdU+ migrating cell counts were also found to be significantly reduced in hGFAPcre::CBP$^{Fl/Fl}$ mice. **(D)** Percentage of BrdU+ cells that reached the 3ry matrix compared to all BrdU+ cells that left dentate neuroepithelium, suggesting that less cells reach their destination in transgenic mice during the period between E14.5 and E16.5. *Scale bar: 50 µm (A,B); *p < 0.05, **p < 0.01*

4.6 Olfactory bulb and olfaction

4.6.1 Early CBP depletion leads to a reduced olfactory bulb size

Following the leads found in overview sections of *hGFAPcre::CBP$^{Fl/Fl}$* animals (see 4.2.2) the olfactory system was analyzed more thoroughly in P30 animals. Besides the consistent observation of a cell accumulation at the beginning of the rostral migratory stream close to the ventricular-subventricular zone below the corpus callosum which could not be found in control animals, a significant reduction of the size of the olfactory bulb was measured in sagittal, H&E stained sections at P30 (Fig. 27).

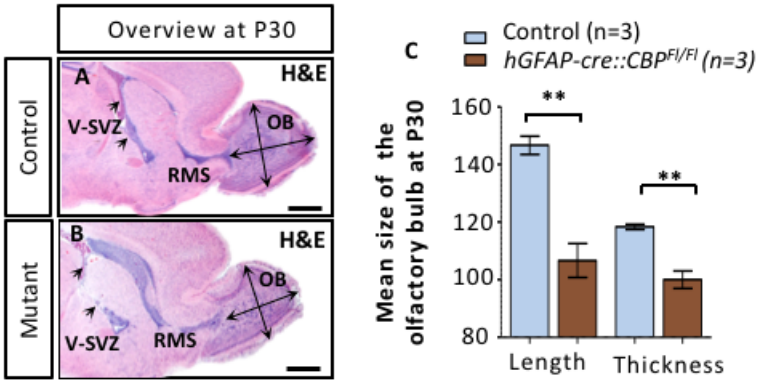

Figure 27: Olfactory bulb size at P30. (A,B) Sagittal overview sections at P30 displaying the ventricular-subventricular zone (V-SVZ) highlighted with black arrowheads, the rostral migratory stream (RMS) and the olfactory bulb (OB) with measurements of olfactory bulb length and thickness indicated by arrows. **(C)** Length and thickness measurements show a significant reduction in olfactory bulb size in *hGFAPcre::CBP$^{Fl/Fl}$* mice at P30. *Scale bar: 1000 µm (A,B); **p < 0.01*

4.6.2 Cytoarchitecture within the olfactory bulb is altered in *hGFAPcre::CBP$^{Fl/Fl}$* animals and the excitatory-inhibitory balance in the glomerular layer is disrupted

Concerning structural differences, it was observed that neither the internal plexiform layer (IPL) nor the rostral migratory stream bundle within the olfactory bulb were consistently determinable in the olfactory bulb of transgenic mice. NeuN was then used as a neuronal marker to further investigate the composition and integrity of the different layers of the olfactory bulb. It was shown that both in the granule cell layer (GCL) as well as in the glomerular layer (GL) the percentage of NeuN positive neuronal cells are reduced in *hGFAPcre::CBP$^{Fl/Fl}$* animals. Mitral cells in the mitral cell layer (MCL) and tufted cells in the external plexiform layer (EPL) where not covered by this analysis since they do not express NeuN[262]. Cell subpopulation composition and excitatory-inhibitory balance in the glomerular layer was investigated further using Tbr2 and Calbindin staining. Tbr2 was shown to be expressed in a mitral cell and a tufted cell subpopulation as well as glutamatergic excitatoric juxtaglomerular neurons in the glomerular cell layer[263,264].

Calbindin is expressed amongst others in GABAergic inhibitory periglomerular neurons in the granular cell layer[265,266,267]. Quantification resulted in a significantly higher Tbr2+ rate and a significantly lower Calbindin+ rate in the glomerular cell layer of the olfactory bulb at P30 when CBP was missing, thus suggesting that the early loss of CBP leads to an excitatory-inhibitory imbalance in the glomerular layer of the olfactory bulb (Fig. 28).

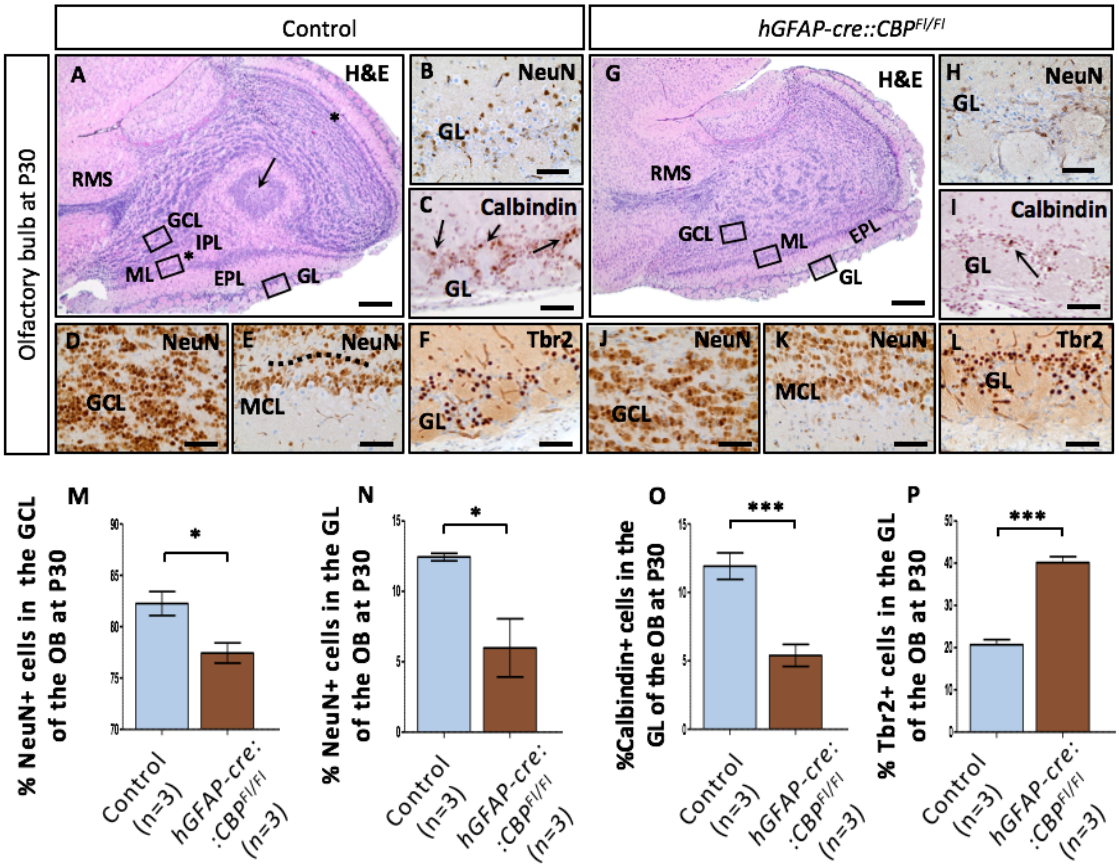

Figure 28: Cytoarchitecture of the olfactory bulb at P30. **(A,G)** Sagittal H&E stained sections of the olfactory bulb with granule cell layer (GCL), internal plexiform layer (IPL,*) mitral cell layer (MCL), external plexiform layer (EPL) and glomerular layer (GL). The arrow marks the continuation of the rostral migratory stream (RMS) within the olfactory bulb. It was frequently found to be undeterminable in transgenic mice. **(B,D,E,H,J,K)** NeuN neuronal staining of the GCL, MCL and GL. The IPL is indicated as a dotted line (E). It was not consistently determinable in *hGFAPcre::CBP$^{Fl/Fl}$* mice (K). **(C,F,I,L)** Calbindin staining of GABAergic periglomerular neurons and Tbr2 staining of glutamatergic juxtaglomerular neurons in the glomerular layer at P30. **(M,N)** The rate of NeuN positive cells was found to be significantly lower after early loss of CBP in both the GCL and GL. **(O,P)** While the rate of calbindin positive inhibitory neurons was significantly reduced in the GL of the OB in *hGFAPcre::CBP$^{Fl/Fl}$* mice, the rate of Tbr2 positive excitatory neurons was significantly increased compared to control animals, suggesting an excitatory-inhibitory imbalance. *Scale bar: 220 µm (A,G) 130 µm (B-F,H-L); *p < 0.05, ***p < 0.001*

No substantial amount of proliferation or apoptosis that could have constituted these findings was observed in the olfactory bulb at P30 in Ki67 proliferation- and Caspase 3 apoptosis stained sections. Concerning gliogenesis and composition, no differences were found between transgenic and control mice in S100 and Olig2 stained sections of the olfactory bulb at P30 (App. 12). The expression of S100 - a family of low-molecular-weight proteins with two calcium binding sites involved in different regulation processes in cells[268] - characterizes thereby an advanced astroglial maturation after the loss of the cell's neural stem cell character[269]. Frequently, S100 was used as a marker for astrocytes. Olig2 on the other hand - a basic helix-loop-helix transcription factor - was previously described as a specific marker for oligodendrocytes[270,271].

4.6.3 Cells in the accumulation found in transgenic mice lose their stem cell character and partly differentiate towards mature neurons

The observed cell accumulation close to the ventricular-subventricular zone was analysed at P15 as this was the time point which was used for BrdU injection for a BrdU/EdU double pulse fate-mapping experiment (see. 4.6.4). The accumulation was located between the the corpus callosum and the ceiling of the lateral ventricle at both sides of the brain. Cells closer to the ventricle were rather Sox2 positive and thus more premature and of stem cell character than cells farther from the ventricle. In contrast, more cells farther from the ventricle, closer to the corpus callosum where observed to be NeuN positive and consequently more differentiated than when located close to the ventricle. In conjunction with the findings in the olfactory bulb this suggests that cells closer to the ventricle were later born neuroblasts adding to the accumulation instead of travelling to the olfactory bulb. Besides, a significant amount of apoptosis within the cell accumulation was found using Caspase 3 apoptosis staining. On the other hand, only little proliferation was observed in the accumulation in Ki67 stained sections at P15 letting a neoplastic process as a cause for the cell mass appear unlikely (Fig. 29).

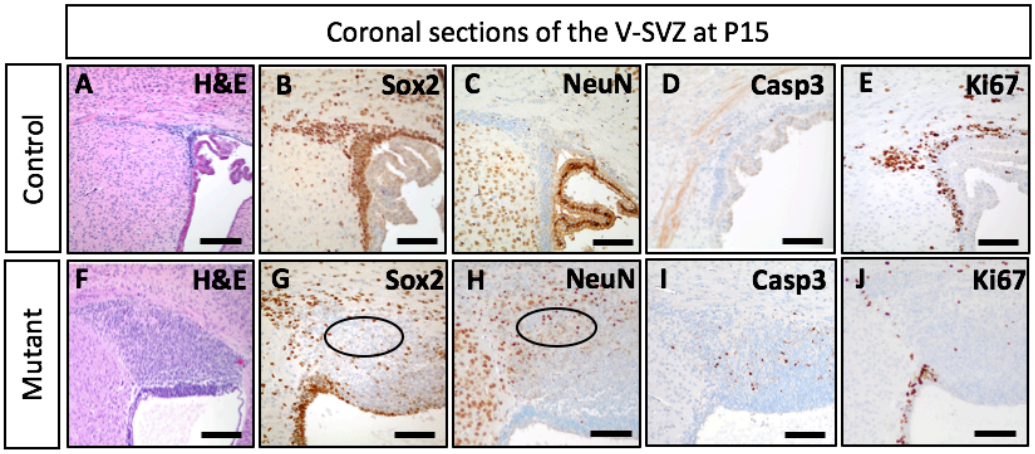

Figure 29: Characterisation of the cell accumulation found in *hGFAPcre::CBP$^{Fl/Fl}$* mice. (A,F) H&E staining of frontal sections in the area of the ventricular-subventricular zone of the left lateral ventricle at P15 showing location and size of the cell accumulation found in transgenic mice. **(B,G,C,H)** Sox2 and NeuN stained frontal sections show that cells closer to the ventricle are rather Sox2 positive and thus of stem cell character while cells farther from the ventricle are rather NeuN positive and frequently more differentiated. Circles mark areas farther from the ventricle. **(D,I)** Caspase 3 apoptosis staining shows a significant apoptosis rate within the cell accumulation. **(E,J)** No substantial proliferation was observed within the cell accumulation in Ki67 stained frontal sections at P15. *Scale bar: 150 µm (A,F) 75 µm (B-E,G-J)*

4.6.4 A migration deficit leads to cell accumulation and an underdeveloped olfactory bulb when CBP is missing during embryonal development.

To confirm that a migration deficit indeed was the cause of the cell accumulation and the reduced NeuN positive rates in the olfactory bulb found at P30, another BrdU/EdU double pulse fate-mapping experiment was conducted. BrdU was administered intraperitoneally at P15 and EdU 15 days later at P30, two hours before preparation. Thus, neural stem cells in the ventricular-subventricular zone were marked at P15 during proliferation before they travelled to the olfactory bulb via the rostral migratory stream. BrdU+ rates were determined in the V-SVZ of control animals, the cell accumulation of transgenic mice and in the granular cell layer & glomerular layer of all animals. While the BrdU+ rate in the cell accumulation of *hGFAPcre::CBP$^{Fl/Fl}$* mice was significantly higher than in the V-SVZ of control mice, the BrdU+ rate in the granular cell layer of the olfactory bulb was significantly lower, implicating a migration deficit that leads to the cell accumulation and underdeveloped olfactory bulb. In the glomerular layer only a tendency towards lower BrdU+ rates in *hGFAPcre::CBP$^{Fl/Fl}$* mice was observed. However, the reduced NeuN+ rate in the GL was not yet considered in this setting (see. 4.6.5).

At the same time, no cells were found to be both BrdU+ and EdU+ and thus still proliferating. Hence, the observed differences in BrdU+ rates in the different areas cannot be explained by differences in continued proliferation of the neuroblasts once they left the V-SVZ zone (Fig. 30).

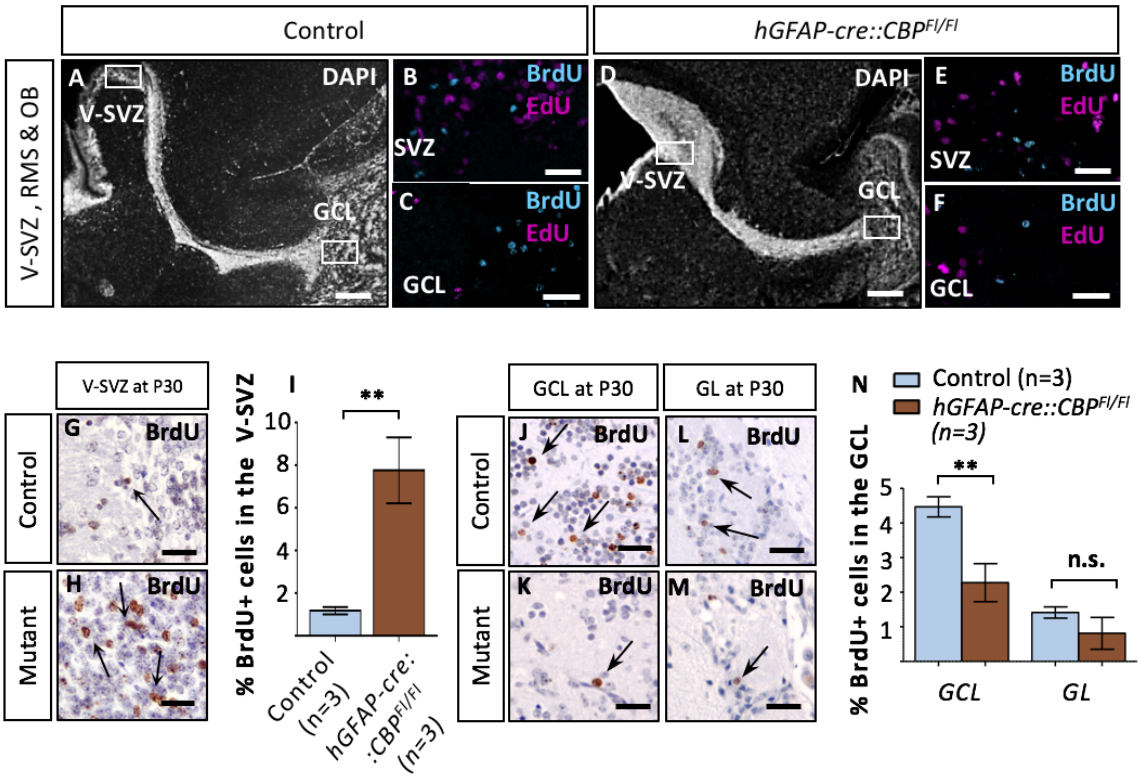

Figure 30: A migration deficit leads to cell accumulation near the ventricular-subventricular zone in *hGFAPcre::CBP$^{Fl/Fl}$* mice . **(A,D)** DAPI, nucleus stained[272] overview of the ventricular-subventricular zone (V-SVZ), rostral migratory stream (RMS) and granular cell layer (GCL) of the olfactory bulb in sagittal sections at P30. **(B,C,E,F)** In BrdU/EdU immunofluorescence staining of the V-SVZ and GCL no cells that were both BrdU+ and EdU+ were found. BrdU was administered at P15 and EdU at P30, 2h before preparation. **(G,H)** BrdU+ cells in the V-SVZ of control animals and within the cell accumulation found in *hGFAPcre::CBP$^{Fl/Fl}$* mice 15 days after BrdU injection. **(I)** The BrdU+ rate was found to be significantly higher within the cell accumulation than in the V-SVZ of control animals. **(J,K,L,M)** BrdU+ cells in the GCL and glomerular layer (GL) of the olfactory bulb 15 days after injection. **(N)** The BrdU+ rate in the GCL of the olfactory bulb was measured to be significantly reduced in transgenic mice, whereas no significant difference between the two groups was found in the GL. *Scale bar: 250 µm (A,D) 30 µm (B,C,E,F,G,H,J-M); **p < 0.01*

4.6.5 Neurogenesis in the olfactory bulb is impaired after early loss of CBP

Following the lead that NeuN+ rates in the granular cell layer and glomerular layer of the OB in *hGFAPcre::CBP$^{Fl/Fl}$* animals are significantly reduced and that migration was found to be impaired, neurogenesis rates at P30 were estimated as BrdU+ cells per mm^2 times the NeuN+ rate in the respective area as was done previously[273]. These so determined values were used for statistical comparison between CBP deficient animals and control litter mates. While the BrdU+ rate was

only significantly reduced in the granular cell layer of the olfactory bulb of transgenic mice at P30 (see. 4.6.4), the estimated neurogenesis values were found to be significantly reduced both in the granular cell layer as well as the glomerular layer of *hGFAPcre::CBP$^{Fl/Fl}$* animals (Fig. 31). Thus, allowing the conclusion that a complete loss of CBP in GFAP expressing precursor cells during early development leads to a decrease in olfactory bulb neurogenesis.

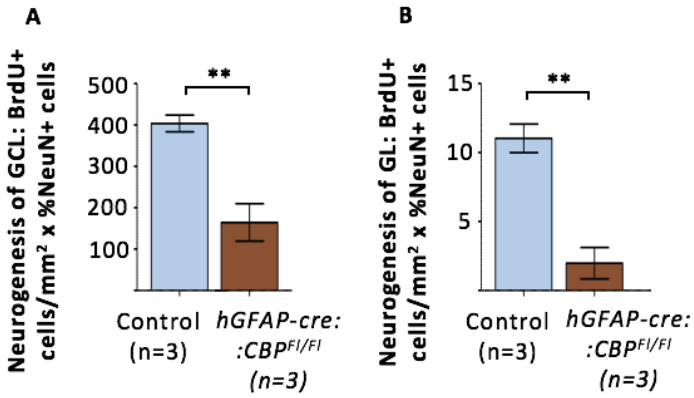

Figure 31: Neurogenesis in the olfactory bulb between P15 and P30. (A,B) Neurogensis was estimated in the granular cell layer and the glomerular cell layer of the olfactory bulb with BrdU injection at P15. Neurogenesis was shown to be significantly reduced in both the granular cell layer and the glomerular layer of *hGFAPcre::CBP$^{Fl/Fl}$* mice. ***p < 0.01*

4.6.6 Olfaction and olfactory-related behaviour is impaired in *hGFAPcre::CBP$^{Fl/Fl}$* transgenic mice

Analyzing the food motivated aspect of olfaction through the buried food test produced a significant difference between transgenic mice and control litter mates. After early loss of CBP, mice spent significantly more time searching for the buried chocolate pellet than wild type animals suggesting that CBP depletion leads to reduced olfactory detection abilities (Fig. 26). The habituation/dishabituation test on the other hand led to more ambiguous findings. While curve appearance and a two-way repeated measurements ANOVA test confirmed that *hGFAPcre::CBP$^{Fl/Fl}$* mice did exhibit habituation and dishabituation behaviour in general, Bonferroni's multiple comparisons post hoc test for the repeated habituation steps showed significant differences between the two groups at time points t3 and t4. At these time points, *hGFAPcre::CBP$^{Fl/Fl}$* mice spent significantly more time examining the presented scent (Fig. 32). Furthermore, non-linear regression analysis produced further differences between the two habituation curves as the habituation curve for transgenic mice showed a relatively bad fit (R^2= 0.3229) compared to the relatively good fit of the habituation curve for control animals (R^2= 0.8071) (App. 13) underlining the qualitative differences in curve appearance what suggests that habituation happens delayed in transgenic mice.

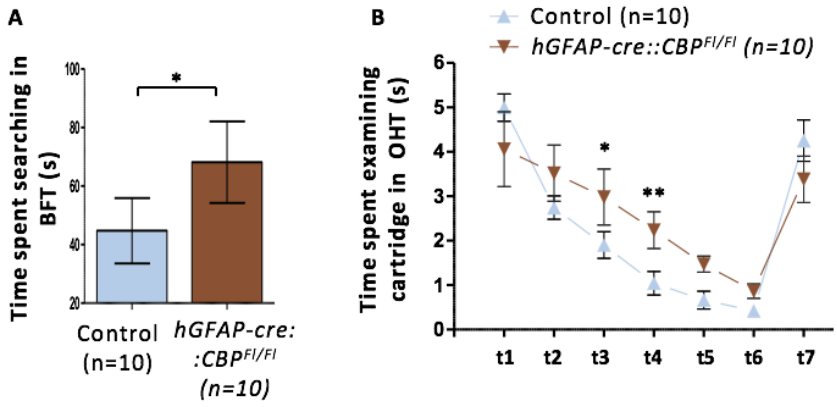

Figure 32: Differences in olfactory related behavior between transgenic- and control mice. ***(A)*** The buried food test (BFT) showed significant differences in time spent searching between the two groups suggesting reduced olfactory detection abilities of *hGFAPcre::CBP$^{Fl/Fl}$* mice. **(B)** In the habituation/ dishabituation test transgenic mice spent significantly more time examining the cartridge carrying the novel scent when presented for the 3rd and 4th time suggesting that CBP depletion leads to delayed habituation. *$p < 0.05$, **$p < 0.01$*

The dark/light box test was used to determine the influence of anxiety and curiosity on behavior as confounding variables. It was found that *hGFAPcre::CBP$^{Fl/Fl}$* mice spent significantly less time exploring the novel environment of the bright and open chamber of the box and accordingly transitioned less often between the two compartments (Table 4). This suggests that the early loss of CBP leads to a shifted anxiety/curiosity ratio towards more aversive behaviour compared to control animals. Nevertheless, with the alterations described in olfactory bulb anatomy and neural composition it seems more likely that a reduced olfactory sense leads to a more aversive behaviour in the transgenic mice, rather than a more anxiety driven behaviour leading to the observed results in olfactory testing. That is to say, a more anxiety driven behaviour cannot explain the longer sniffing times found in transgenic mice during habituation testing.

Parameter	Control group	*hGFAP-cre::CBP$^{fl/fl}$*	p-value	Results
Mean latency [s] +/- SE	12.5 +/- 1.3	26.0 +/- 10.6	0.223	n.s.
Mean no° of transitions [no°] +/- SE	23.7 +/- 1.3	10.0 +/- 2.0	0.0001	***
Mean time spent in light [s] +/- SE	129.7 +/- 10.4	73.5 +/- 14.8	0.0117	*

Table 4: Dark/light behavior test

4.7 Analysis of brain MR images from RTS patients

4.7.1 RTS patients have a smaller sized brain compared to age-matched control children

Microcephaly and smaller brain sizes as well as dysmorphia of the head have been described repeatedly in Rubinstein-Taybi syndrome patients[274,275,276]. In line with these mostly qualitative findings, significantly reduced anterior-posterior diameters of both hemispheres were verified in axial MRI sections when compared to anterior-posterior diameters in MR images from age-matched control children. Left-right diameters, however, were found to be significantly reduced only on a level with the anterior horn of the lateral ventricles and thus in the anterior part of the brain, what is especially compatible with dysmorphia of the head (Fig. 33).

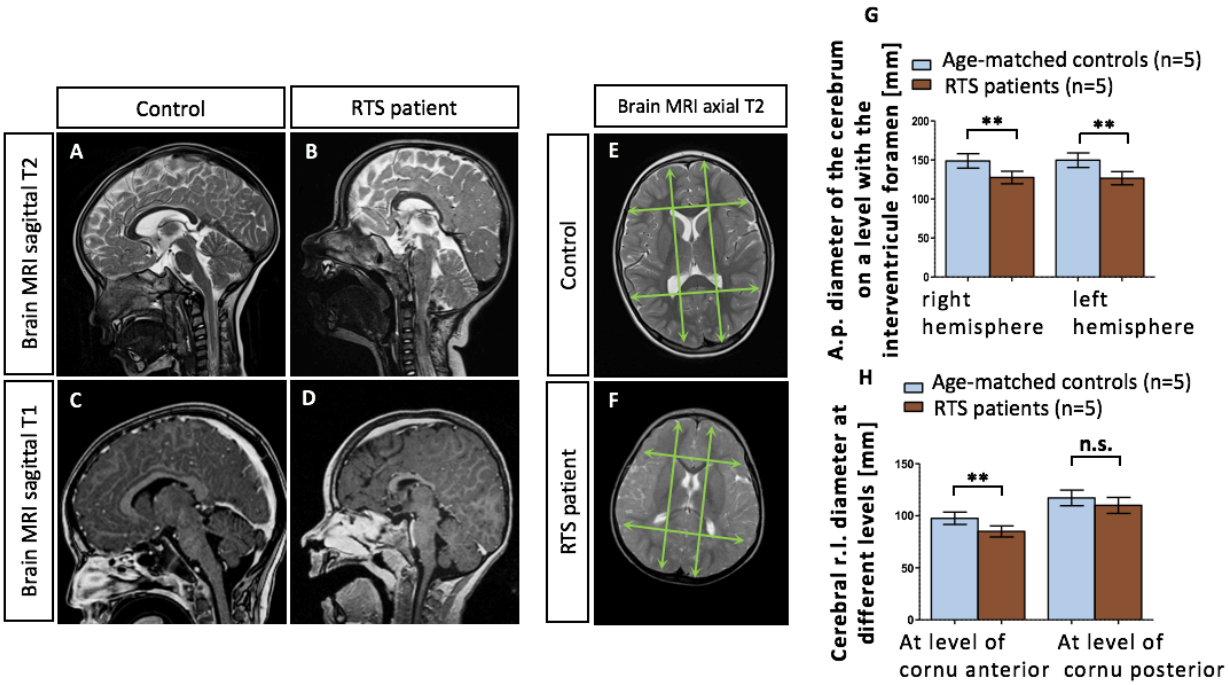

Figure 33: Cranial MR images of Rubinstein-Taybi syndrome patients. **(A-D)** Sagittal T2 and T1 weighted MR images of a RTS patient and age matched control child aged 30 months. Microcephaly and a smaller brain can be observed in the RTS MR images. **(E,F)** Axial T2 weighted MR images with section level on a level with the interventricular foramen. Anterior-posterior and left-right diameter measurements are displayed as green arrows. Furthermore, myelination deficits and dysmorphic heads were found in the MR images of RTS patients. **(G)** The paramedian anterior-posterior diameter was measured to be significantly reduced in both hemispheres of RTS patient's brain MR images. **(H)** The anterior left-right diameter, measured in axial sections on a level with the anterior horns of the lateral ventricles, was shown to be significantly smaller when compared to measurements in MR images of age-matched control children. No such difference was found for the measured posterior left-right diameter. *$**p < 0.01$*

4.7.2 Corpus callosum thickness is reduced in RTS patients

Following reports of corpus callosum dysplasia in RTS patients[240,241,277], the corpus callosum genu and splenium thickness as well as the anterior-posterior corpus callosum length were measured in sagittal MR sections. While splenium thickness and length measurement comparisons produced only trends towards smaller values due to the small number of patients and necessary case-control setting, the genu thickness was shown to be significantly reduced in RTS patients, hence supporting previous reports. Furthermore, as an additional finding, the distance between basis of the frontal lobe to the sellar floor was found to be significantly bigger in the MR images of RTS patients, which fits with reduced brain sizes. Width measurements of the anterior and posterior horns of the lateral ventricles, however, did not show differences between RTS patients and control children (Fig. 28).

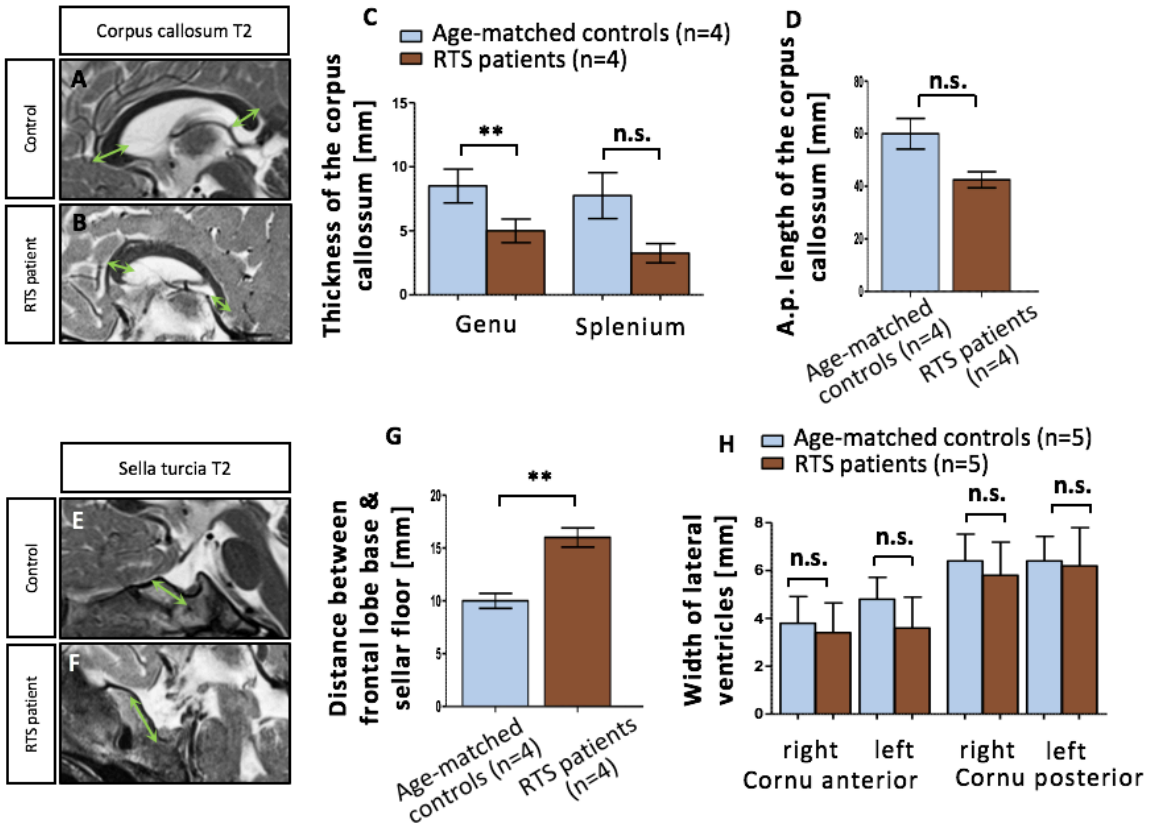

Figure 34: Structural parameters in MR images of RTS patients and control children. (A,B) The corpus callosum in sagittal, T2 weighted MR sections. Thickness measurements of the genu and splenium are highlighted with green arrows. **(C)** The thickness of the corpus callosum genu was shown to be significantly reduced in RTS patients. For the CC splenium a clear trend towards smaller values was found. **(D)** Also, a trend towards a reduced corpus callosum length when being diagnosed with RTS was observable. **(E,F)** Sagittal MR sections magnified in the area of the pituitary gland. The distance between the base of the frontal lobe and the sellar floor is marked with green arrows. **(G)** It was shown to be significantly bigger in RTS patients. **(H)** Width measurements of the horns of the lateral ventricles did not produce differences between RTS patients and age-matched control children. ***p < 0.01*

5. Discussion

5.1 A homozygous knock-out model for a disease with a heterozygous genotype

Previous loss-of-function approaches investigating the role of CBP in forebrain development and RTS related cognitive impairment were constrained by partial and uncertain levels of CBP function inhibition in heterozygous knock-out or other transgenic RTS mouse models[226]. A dominant negative effect of truncated or functionally impaired CBP variants was thereby described in different models implicating a reduced function also of the remaining CBP transcribed from the unaffected allele in those models or RTS cases[278–280]. Correspondingly, analogous to previous studies on heterozygous knock-out or transgenic models, a basic analysis of the heterozygous variant *hGFAPcre::CBP$^{Fl/+}$* used in this work did not show consistent and striking abnormalities within the forebrain that could help explain the clinical findings of mental retardation and cognitive impairment in RTS or illuminate pathophysiological processes which lead to its clinical picture. Therefore, here a homozygous tissue-specific complete CBP knock-out model *hGFAPcre::CBP$^{Fl/Fl}$* was used to study more profoundly the role of CBP in forebrain development and identify developmental processes and forebrain structures that depend highly on CBP and hence are likely to also be impaired in their development in RTS. That the truncated variant *CBP^{Stop523}* in the used model could also occur in RTS is furthermore likely, as it misses its HAT domain and thus does not bear HAT activity[227]. It had been shown before that loss of HAT activity was sufficient to cause RTS[223]. Hereby, this work adds further evidence to this theory - that the reduction of HAT-activity plays a central role in RTS genesis - through the conducted mutation frequency analysis. It shows an unequal distribution of mutations within the CBP gene of clinical apparent RTS cases with a clear accumulation of mutations affecting the HAT domain. This corresponds well with the fact that RTS is also caused by mutations within the p300 gene, also a transcription co-activator with HAT activity[7,8]. Finally, the concordance of microcephaly and reduced corpus callosum size found both in the used mouse model as well as the acquired cranial MR images of RTS patients further supports the used homozygous conditional knock-out mouse-model in being a viable model for studying basic pathophysiological processes that may lead to the development of mental retardation and cognitive impairment in RTS.

5.2 The role of CBP in forebrain development

5.2.1 General remarks and CBP as a regulator of brain size

Though of high importance for forebrain- and cognitive development - as seen from the example of RTS[1,5] - the early depletion of CBP in the used model does not halt forebrain development completely and general structuring is conserved. Thus, although perturbed, the neocortex with its six layers, the hippocampus and the olfactory bulb are developed, animals are viable - though with an increased 30-day mortality - and show no overt behavioral deficits postnatally. Nevertheless, it has to be noted that the CBP depletion in the used model occurs after neural tube formation and onset of neurogenesis. Hence, it cannot be ruled out that CBP is indeed indispensable for general forebrain structuring or neural tube formation. However, hippocampus development initiates after the time point of complete CBP depletion and still is developed, although in an impaired manner, making a point for a certain expendability of CBP or compensation by other transcription co-activators with HAT activity like p300. Although general forebrain development proceeds, a loss of CBP led to a smaller brain-, neocortex-, hippocampus, olfactory bulb- and corpus callosum size in the analyzed knock-out model supporting previous postulations of its important role in brain size regulation. A heterozygous loss of CBP had been shown to lead to microcephaly both in mouse-models as well as in RTS patients[281,9,239].

5.2.2 Developmental processes depending on functioning CBP

Regarding developmental processes a study using CBP siRNA knockdown in cortical precursor cell cultures and a study using a induced Pluripotent Stem Cell (iPSC)-neuronal model of RTS patients suggested an essential role of CBP in neural differentiation[282,283]. Both the findings of a disturbed excitatory and inhibitory balance of neurons in the glomerular layer of the OB and the reduced cell volume of 3D reconstructed lamina V pyramidal neurons as a marker for correct neural growth and differentiation in the used conditional knock-out model support these results. Moreover, while the incomplete siRNA knockdown and a postnatal conditional CBP knock-out in principal neurons of the forebrain did not show alterations in cell survival- and proliferation rates[245,282] early CBP depletion leads to visibly increased apoptosis- and lower proliferation rates of neural precursor cells within the germinal ventricular zone during forebrain development. This suggests a higher dependence on CBP of neural precursor cells compared to already senescent neurons. It had thereby been shown before that CBP expression levels decrease with

developmental progress and especially postnatally[282]. In line with these findings adult neurogenesis with its specialized neural precursor cells was also found to be impaired in *hGFAPcre::CBP$^{Fl/Fl}$* mice, especially in the hippocampus. This also corresponds well with deficits in hippocampal synaptic plasticity and memory storage seen in transgenic mice that start expressing a truncated form of CBP in postnatal forebrain neurons[280]. Another important developmental process affected by the early loss of CBP, however, was neural precursor cell migration. In *hGFAPcre::CBP$^{Fl/Fl}$* mice neural precursor cell migration was visibly disturbed during forebrain development. Those deficits were not only measurable for radial migration during neocortex development but also for the unique migration processes during hippocampus formation and within the RMS, through which neuroblasts migrate tangentially towards the OB. For assessing the migration processes during neocortex- and hippocampus development the ratio of traveling cells, to cells reaching their destiny was used as a surrogate marker and found to be reduced compared to measurements in control animals. In the RMS, however, the deficits were of such extent that an accumulation of neural precursor cells that ceased migrating became visible close to their origin in the ventricular-subventricular zone. That these cells where indeed cells born in the V-SVZ was confirmed through the conducted fate mapping experiment. They furthermore started expressing NeuN as a marker of neural differentiation showing that their neurogenic character was preserved although migration was halted. This particularly important role of CBP during OB development and precursor cell migration through the RMS remains also throughout postnatal stages as the reduced number of migrating cells between P15 and P30 in the used knock-out model suggests. So far, numerous factors like DCX (doublecortin) - a microtubule stabilizing protein - or PSA-NCAM - a protein with antiadhesive properties providing a favorable extracellular environment for cell migration - have been found to be important for correct cell migration within the RMS[284–286]. As this is the first time CBP was found to play a central role for unimpaired migration through the RMS it remains to be further investigated which RMS migration regulating downstream factors are especially affected by a decrease in CBP availability. Factors to be examined in subsequent works might be DCX, NCAM, Integrin, Cdk5 (cyclin dependent kinase 5) or BDNF (brain derived neurotrophic factor). They all have been shown to play a vital role in correct cell migration through the RMS and their genes are bound by CBP[39,286]. Reduction of BDNF was furthermore found to be involved with disrupted migration during cerebellar development related to early loss of CBP[76].

5.3 Implications for Rubinstein-Taybi syndrome pathogenesis

5.3.1 Anatomical substrates of mental retardation and cognitive impairment

Neocortex and hippocampus have been postulated as main anatomical substrates of mental retardation and cognitive impairment in RTS in previous works[245,280,282]. With its new findings concerning the general role of CBP in forebrain development this work supports these postulations and identifies the corpus callosum as another structure important for correct cognitive development and affected by reduced CBP availability.

It has been shown that a reduced HAT activity in postnatal transgenic mice leads to deficits in hippocampal synaptic plasticity and memory storage[280,287,288]. A lower CBP activity postnatally may therefore explain clinical findings in RTS patients, especially impairments in memory consolidation, to some extent. This falls in line with the reduced adult neurogenesis found in *hGFAPcre::CBP$^{Fl/Fl}$* mice after early CBP depletion as it had been shown that adult neurogenesis plays an important role in memory formation[201,202]. On the other hand, another study on conditional CBP knock-out in postnatal principal neurons of the hippocampus only found a very modest reduction in the expression of early genes in response to novelty exposure[245]. These unexpected findings could be due to the fact that the development of the hippocampus advanced without disturbance in the model used for this study. Some processes or functions, important for early gene expression and disturbed in RTS, are likely to be conserved and unaffected by solely postnatal depletion of CBP. This is supported by the fact that CBP plays a central role during development of forebrain structures as shown in this work. Neocortex, hippocampus and corpus callosum development are considerably impaired after early loss of CBP leading to the conclusion that their correct functioning is likewise not developed correctly and impaired from an early time point on. It is therefore recommendable to further study cognitive functionality and processes like hippocampal synaptic plasticity and expression of early genes in response to novelty exposure in the used conditional knock-out model or a similar model with early CBP depletion as models of RTS. In terms of the role of the neocortex in RTS , its impaired development and thus impaired functioning could explain especially symptoms such as difficulties in planning and executing motor acts as seen in RTS patients[289,290].

5.3.2 RTS as a neural migration disorder

It has only recently been suggested for the first time that RTS - so far mainly attributed as multiple congenital anomalies and mental retardation syndrome - should be included in the family of neuronal migration disorders due to commonalities with holoprosencephalic and arhinencephalic conditions as observed through in vivo MRI based volumetry of CBP haploinsufficient mice[281]. It is thereby necessary to highlight the fact that the spectrum of neural migration disorders is a large and heterogenous, loosely defined group of cerebral dysgenesis disorders, which share the ethiopathological role of distortion of neural precursor cell migration during central nervous system development. Depending on the source and definition the group entails entities such as schizencephaly, distortions of convulsion formation such as lissencephaly, agyria, macrogyria, microgyria, polymicrogyria, pachygyria, micropolygyria, neuronal heterotopias (including band heterotopia) and agenesis of the corpus callosum, to name just a few[291,292,293]. Many of these entities themselves being subdivided into different subgroups and different forms of manifastations[294]. In addition, there are a large number of syndromes which are associated with neuronal migration disorders, meaning that a disorder of neural migration is part of the syndrome's pathogenesis or that signs of a neural migration disorder may be found in the phenotype, usually besides other disturbed processes or clinical findings. Hence, leading to the syndrome itself being named a neural migration disorder in the broader sense as well. This accounts for example for holoprosencephaly and arhincephaly as stated by Ateca-Cabarga et al.[281,295,296] Depending on the entity or syndrome the distortion of neural migration can occur as a primary defect or secondarily and hence play a more or less significant role in defining the clinical picutre. This aspect can be highlighted by two examples: On the one hand lissencephaly – a disorder characterized by the absence of normal brain convulsions - with causative defects within the DCX and LIS1 gene. Here, molecular genetic analyis unveiled the direct importance of DCX and LIS1 protein function for unhindered neural precursor cell migration. The clinical picture results directly and nearly exclusively from a disturbance of correct neural progenitor migration[297,298,299]. On the other hand holoprosencephaly – a cerebral dysgenesis disorder in which the prosencephalon fails to develop into two hemispheres, whereby the degree of manifestation can vary wildely – with for example causative mutations affecting the SHH gene. SHH is thereby being involved in establishing cell fates at several points during early embryonic development and is a key inductive signal in patterning of the ventral neural tube[295]. In this case

one could say that neural migration deficits, for example a failed development of the body of the corpus callosum, occur secondarily due to these upstream distortions caused by SHH mutations. Thus, due to this heterogenity of phenotypical findings and in many cases uncertain connection of underlying causes and downstream effects, or simple co-appearance, the deduction of the causative of role of a neural migration disorder from clinical findings remains speculative in most cases. Keeping this in mind has the Rubinstein-Taybi Syndrome been associated with a number of findings typical of neural migration disorders such as the aforementioned holoprosencephaly and arhinecephaly[300,301], an abnormally thin cortex and defects like (poli)microgyria, pachigyria and agenesis of the corpus callosum[13,239,240,241,302,303]. It has thereby been shown that microlissencephaly caused by a distortion of neuronal migration contributes to microcephaly, which is also frequently described in RTS and was also found in the MR images of RTS patients investigated in this study[13,275,304]. While our mouse model does not permit assumptions on the effect of CBP depletion on the formation of brain convulsions due to the lissencephalic composition of the mouse brain, other aspects coincided very well with these associations of RTS to neural migration disorders and the corresponding morphological aspects. This firstly includes the findings of microcephaly in our mouse model as seen in microlissencephaly. Or secondly, the reduced olfactory bulb size and neocortex size that resulted after CBP depletion and that are typical of the reduction of prosencephalic tissue as observed in arhincephaly and holoprosencephaly. Thirdly, the reduced corpus callosum size indicating a mild form of corpus callosum agenesis. And finally, the verification of profoundly disturbed migration processes during forebrain development unmasked through the performed fate-mapping experiments in *hGFAPcre::CBP$^{Fl/Fl}$* conditional knock-out mice that suggest the direct causative role of a distortion of neural migration leading the aforementioned phenotypical findings. Thus, with providing evidence that CBP acts as an upstream regulator of correct neural migration – upstream due to its function as a transcription coactivator and its HAT activity – it seems imperative to include the Rubinstein-Taybi syndrome in the spectrum of neural migration disorders in a broader sense as a type of secondary neural migration disorder where the primary genetic alteration goes along with a secondary downstream distortion of neural precursor cell migration besides other affected processes. At least, the results gathered in this work strongly support this assumption and make it also seem very likely that disrupted migration processes during brain development play an important role in RTS pathogenesis. Nevertheless, these

findings do not permit an assumption which pathophysiological process predominantly causes the development of the typical RTS related symptoms such as cognitive impairment and learning disabilities before others. Be it the migration disorder, alterations in germinal layers like the VZ, disturbed neural differentiation or impaired adult neurogenesis. To not narrow the scientific approach on elucidating the causes of these symptoms to one aspect and therefore dismiss or omit other important processes, the development of RTS should not be attributed to one single disrupted process during developmental stages but has to be seen rather as the result of continuous interference between multiple processes that are affected by diminished availability of CBP or its HAT activity. The collectivity of these affected developmental processes has consequently to be further investigated and further processes that might depend on CBP have to be identified. Of course, an in-depth comparison of findings between Rubinstein-Taybi syndrome and available mouse models to other entities such as neural migration disorders or disorders that result from distorted cell differentiation, hindered establishment of adult neurogenesis or impaired stem cell viability could allow deductions with regards to RTS pathogenesis as well and would be desirable. This comparison should include a solid statistical analysis of frequencies of findings and take the possibility of co-appearance of different genetic alterations into account. As this would require a well-planned methodical approach due to the vast heterogeneity and ambiguity - as set out above - to reduce bias and arbitrary acception of assumptions this would exceed the set framework and aim chosen for this work and should be done separately. Another aspect is that, while this work focused mainly on processes related to the neural cell line, the importance of the glial cell line for forebrain integrity and functionality is undisputed and effects of CBP depletion on glial cells and related processes should therefore be center of future investigations as well. To sum it up, while this work delivers strong evidence that neural precursor cell migration, neural cell differentiation, establishment of adult neurogenesis and precursor cell viability are processes that depend highly on CBP during brain development and hence are likely to be disturbed also during Rubinstein-Taybi syndrome development more consecutive research has to be done. That said, an advance in the field of understanding the pathogenesis of the Rubinstein-Taybi syndrome or other comparable rare diseases is eventually essential for their early diagnosis, a goal-orientated clinical approach and finally a first step in the search for ways of preventing the development of chronic conditions such as mental retardation and cognitive impairment.

6. References

1. RUBINSTEIN, J. H. & TAYBI, H. Broad thumbs and toes and facial abnormalities. A possible mental retardation syndrome. *Am. J. Dis. Child.* **105,** 588–608 (1963).
2. Hennekam, R. C., Stevens, C. A. & Van de Kamp, J. J. Etiology and recurrence risk in Rubinstein-Taybi syndrome. *Am. J. Med. Genet. Suppl.* **6,** 56–64 (1990).
3. Hennekam, R. C. M. Rubinstein–Taybi syndrome. *Eur. J. Hum. Genet.* **14,** 981–985 (2006).
4. Cantani, A. & Gagliesi, D. Rubinstein-Taybi syndrome. Review of 732 cases and analysis of the typical traits. *Eur. Rev. Med. Pharmacol. Sci.* **2,** 81–7
5. Petrij, F. *et al.* Rubinstein-Taybi syndrome caused by mutations in the transcriptional co-activator CBP. *Nature* **376,** 348–51 (1995).
6. Bartsch, O. *et al.* DNA sequencing of CREBBP demonstrates mutations in 56% of patients with Rubinstein-Taybi syndrome (RSTS) and in another patient with incomplete RSTS. *Hum. Genet.* **117,** 485–93 (2005).
7. Roelfsema, J. H. *et al.* Genetic heterogeneity in Rubinstein-Taybi syndrome: mutations in both the CBP and EP300 genes cause disease. *Am. J. Hum. Genet.* **76,** 572–80 (2005).
8. Zimmermann, N., Maria, A., Ferrer Acosta, B., Kohlhase, J. & Bartsch, O. Confirmation of EP300 gene mutations as a rare cause of Rubinstein–Taybi syndrome. *Eur. J. Hum. Genet.* **15,** 837–842 (2007).
9. Fergelot, P. *et al.* Phenotype and genotype in 52 patients with Rubinstein-Taybi syndrome caused by EP300 mutations. *Am. J. Med. Genet. A* **170,** 3069–3082 (2016).
10. Stevens, C. A. *Rubinstein-Taybi Syndrome*. *GeneReviews(®)* (University of Washington, Seattle, 1993).
11. Van Genderen, M. M., Kinds, G. F., Riemslag, F. C. C., C, R. & Hennekam, M. Ocular features in Rubinstein-Taybi syndrome: investigation of 24 patients and review of the literature. *Br J Ophthalmol* **84,** 1177–1184 (2000).
12. Stevens, C. A., Pouncey, J. & Knowles, D. Adults with Rubinstein-Taybi syndrome. *Am. J. Med. Genet. A* **155A,** 1680–4 (2011).
13. Kumar, S., Suthar, R., Panigrahi, I. & Marwaha, R. K. Rubinstein-Taybi syndrome: Clinical profile of 11 patients and review of literature. *Indian J. Hum. Genet.* **18,** 161–6 (2012).
14. Goodfellow, A., Emmerson, R. W. & Calvert, H. T. Rubinstein-Taybi syndrome and spontaneous keloids. *Clin. Exp. Dermatol.* **5,** 369–70 (1980).
15. Shilpashree, P., Jaiswal, A. K. & Kharge, P. M. Keloids: an unwanted spontaneity in rubinstein-taybi syndrome. *Indian J. Dermatol.* **60,** 214 (2015).
16. Stevens, C. A. & Bhakta, M. G. Cardiac abnormalities in the Rubinstein-Taybi syndrome. *Am. J. Med. Genet.* **59,** 346–348 (1995).
17. Hennekam, R. C., Van Den Boogaard, M. J., Sibbles, B. J. & Van Spijker, H. G. Rubinstein-Taybi syndrome in The Netherlands. *Am. J. Med. Genet. Suppl.* **6,** 17–29 (1990).

18. Miller, R. W. & Rubinstein, J. H. Tumors in Rubinstein-Taybi syndrome. *Am. J. Med. Genet.* **56,** 112–5 (1995).

19. Roelfsema, J. H. & Peters, D. J. M. Rubinstein–Taybi syndrome: clinical and molecular overview. *Expert Rev. Mol. Med.* **9,** 1–16 (2007).

20. Hennekam, R. C. *et al.* Psychological and speech studies in Rubinstein-Taybi syndrome. *Am. J. Ment. Retard.* **96,** 645–60 (1992).

21. Hennekam, R. C., Lommen, E. J., Strengers, J. L., Van Spijker, H. G. & Jansen-Kokx, T. M. Rubinstein-Taybi syndrome in a mother and son. *Eur. J. Pediatr.* **148,** 439–41 (1989).

22. Marion, R. W., Garcia, D. M. & Karasik, J. B. Apparent dominant transmission of the Rubinstein-Taybi syndrome. *Am. J. Med. Genet.* **46,** 284–7 (1993).

23. Breuning, M. H. *et al.* Rubinstein-Taybi syndrome caused by submicroscopic deletions within 16p13.3. *Am. J. Hum. Genet.* **52,** 249–54 (1993).

24. Imaizumi, K. & Kuroki, Y. Rubinstein-Taybi syndrome with de novo reciprocal translocation t(2;16) (p13.3; p13.3). *Am. J. Med. Genet.* **38,** 636–639 (1991).

25. Lacombe, D., Saura, R., Taine, L. & Battin, J. Confirmation of assignment of a locus for Rubinstein-Taybi syndrome gene to 16p13.3. *Am. J. Med. Genet.* **44,** 126–8 (1992).

26. Gervasini, C. *et al.* High frequency of mosaic CREBBP deletions in Rubinstein–Taybi syndrome patients and mapping of somatic and germ-line breakpoints. *Genomics* **90,** 567–573 (2007).

27. de Vries, T. I. *et al.* Mosaic CREBBP mutation causes overlapping clinical features of Rubinstein-Taybi and Filippi syndromes. *Eur. J. Hum. Genet.* **24,** 1363–6 (2016).

28. Schorry, E. K. *et al.* Genotype-phenotype correlations in Rubinstein-Taybi syndrome. *Am. J. Med. Genet. Part A* **146A,** 2512–2519 (2008).

29. Spena, S. *et al.* Insights into genotype-phenotype correlations from *CREBBP* point mutation screening in a cohort of 46 Rubinstein-Taybi syndrome patients. *Clin. Genet.* **88,** 431–440 (2015).

30. Goodman, R. H. & Smolik, S. CBP/p300 in cell growth, transformation, and development. *Genes Dev.* **14,** 1553–77 (2000).

31. Bannister, A. J. & Kouzarides, T. The CBP co-activator is a histone acetyltransferase. *Nature* **384,** 641–3 (1996).

32. Ogryzko, V. V, Schiltz, R. L., Russanova, V., Howard, B. H. & Nakatani, Y. The transcriptional coactivators p300 and CBP are histone acetyltransferases. *Cell* **87,** 953–9 (1996).

33. Chawla, S., Hardingham, G. E., Quinn, D. R. & Bading, H. CBP: a signal-regulated transcriptional coactivator controlled by nuclear calcium and CaM kinase IV. *Science* **281,** 1505–9 (1998).

34. Bannister, A. J. & Kouzarides, T. Regulation of chromatin by histone modifications. *Cell Res.* **21,** 381–95 (2011).

35. Verdone, L., Caserta, M. & Mauro, E. Di. Role of histone acetylation in the control of gene expression. *Biochem. Cell Biol.* **83,** 344–353 (2005).

36. Kwok, R. P. *et al.* Nuclear protein CBP is a coactivator for the transcription factor CREB. *Nature* **370,** 223–6 (1994).

37. Chrivia, J. C. *et al.* Phosphorylated CREB binds specifically to the nuclear protein CBP. *Nature* **365,** 855–859 (1993).

38. Bedford, D. C., Kasper, L. H., Fukuyama, T. & Brindle, P. K. Target gene context influences the transcriptional requirement for the KAT3 family of CBP and p300 histone acetyltransferases. *Epigenetics* **5,** 9–15 (2010).

39. Ramos, Y. F. M. *et al.* Genome-wide assessment of differential roles for p300 and CBP in transcription regulation. *Nucleic Acids Res.* **38,** 5396–408 (2010).

40. Wydner, K. L., Bhattacharya, S., Eckner, R., Lawrence, J. B. & Livingston, D. M. Localization of human CREB-binding protein gene (CREBBP) to 16p13.2-p13.3 by fluorescence in situ hybridization. *Genomics* **30,** 395–6 (1995).

41. Giles, R. H. *et al.* Construction of a 1.2-Mb Contig Surrounding, and Molecular Analysis of, the Human CREB-Binding Protein (CBP/CREBBP) Gene on Chromosome 16p13.3. *Genomics* **42,** 96–114 (1997).

42. Thompson, P. R. *et al.* Regulation of the p300 HAT domain via a novel activation loop. *Nat. Struct. Mol. Biol.* **11,** 308–15 (2004).

43. Dyson, H. J. & Wright, P. E. Role of Intrinsic Protein Disorder in the Function and Interactions of the Transcriptional Coactivators CREB-binding Protein (CBP) and p300. *J. Biol. Chem.* **291,** 6714–6722 (2016).

44. Piskacek, S. *et al.* Nine-amino-acid transactivation domain: Establishment and prediction utilities. *Genomics* **89,** 756–768 (2007).

45. Teufel, D. P., Freund, S. M., Bycroft, M. & Fersht, A. R. Four domains of p300 each bind tightly to a sequence spanning both transactivation subdomains of p53. *Proc. Natl. Acad. Sci. U. S. A.* **104,** 7009–14 (2007).

46. Ferreon, J. C. *et al.* Cooperative regulation of p53 by modulation of ternary complex formation with CBP/p300 and HDM2. *Proc. Natl. Acad. Sci. U. S. A.* **106,** 6591–6 (2009).

47. Wojciak, J. M., Martinez-Yamout, M. A., Dyson, H. J. & Wright, P. E. Structural basis for recruitment of CBP/p300 coactivators by STAT1 and STAT2 transactivation domains. *EMBO J.* **28,** 948–958 (2009).

48. O'Sullivan, L. A., Liongue, C., Lewis, R. S., Stephenson, S. E. M. & Ward, A. C. Cytokine receptor signaling through the Jak-Stat-Socs pathway in disease. *Molecular Immunology* **44,** 2497–2506 (2007).

49. Goto, N. K., Zor, T., Martinez-Yamout, M., Dyson, H. J. & Wright, P. E. Cooperativity in transcription factor binding to the coactivator CREB-binding protein (CBP). The mixed lineage leukemia protein (MLL) activation domain binds to an allosteric site on the KIX domain. *J. Biol. Chem.* **277,** 43168–74 (2002).

50. Ernst, P., Wang, J., Huang, M., Goodman, R. H. & Korsmeyer, S. J. MLL and CREB Bind Cooperatively to the Nuclear Coactivator CREB-Binding Protein. *Mol. Cell. Biol.* **21,** 2249–2258 (2001).

51. Zor, T., Mayr, B. M., Dyson, H. J., Montminy, M. R. & Wright, P. E. Roles of phosphorylation and helix propensity in the binding of the KIX domain of CREB-binding protein by constitutive (c-Myb) and inducible (CREB) activators. *J. Biol. Chem.* **277,** 42241–8 (2002).

52. Cheng, J. C. *et al.* CREB is a critical regulator of normal hematopoiesis and leukemogenesis. *Blood* **111,** 1182–92 (2008).

53. Zeng, L., Zhang, Q., Gerona-Navarro, G., Moshkina, N. & Zhou, M.-M. Structural basis of site-specific histone recognition by the bromodomains of human coactivators PCAF and CBP/p300. *Structure* **16,** 643–52 (2008).

54. Park, S., Martinez-Yamout, M. A., Dyson, H. J. & Wright, P. E. The CH2 domain of CBP/p300 is a novel zinc finger. *FEBS Lett.* **587,** 2506–11 (2013).

55. Drendall, C. I., Pham, Q. H. & Dietze, E. C. Purification and characterization of recombinant CH3 domain fragment of the CREB-binding protein. *Protein Expr. Purif.* **70,** 196–205 (2010).

56. Hottiger, M. O. & Nabel, G. J. Viral replication and the coactivators p300 and CBP. *Trends Microbiol.* **8,** 560–5 (2000).

57. Ferreon, J. C., Martinez-Yamout, M. A., Dyson, H. J. & Wright, P. E. Structural basis for subversion of cellular control mechanisms by the adenoviral E1A oncoprotein. *Proc. Natl. Acad. Sci. U. S. A.* **106,** 13260–5 (2009).

58. Ferreon, A. C. M., Ferreon, J. C., Wright, P. E. & Deniz, A. A. Modulation of allostery by protein intrinsic disorder. *Nature* **498,** 390–394 (2013).

59. Jansma, A. L. *et al.* The high-risk HPV16 E7 oncoprotein mediates interaction between the transcriptional coactivator CBP and the retinoblastoma protein pRb. *J. Mol. Biol.* **426,** 4030–48 (2014).

60. Vendel, A. C., McBryant, S. J. & Lumb, K. J. KIX-mediated assembly of the CBP-CREB-HTLV-1 tax coactivator-activator complex. *Biochemistry* **42,** 12481–7 (2003).

61. Vendel, A. C. & Lumb, K. J. NMR mapping of the HIV-1 Tat interaction surface of the KIX domain of the human coactivator CBP. *Biochemistry* **43,** 904–8 (2004).

62. Cook, P. R., Polakowski, N. & Lemasson, I. HTLV-1 HBZ protein deregulates interactions between cellular factors and the KIX domain of p300/CBP. *J. Mol. Biol.* **409,** 384–98 (2011).

63. Rowley, J. D. *et al.* All patients with the T(11;16)(q23;p13.3) that involves MLL and CBP have treatment-related hematologic disorders. *Blood* **90,** 535–41 (1997).

64. Borrow, J. *et al.* The translocation t(8;16)(p11;p13) of acute myeloid leukaemia fuses a putative acetyltransferase to the CREB–binding protein. *Nat. Genet.* **14,** 33–41 (1996).

65. Ida, K. *et al.* Adenoviral E1A-associated protein p300 is involved in acute myeloid leukemia with t(11;22)(q23;q13). *Blood* **90,** 4699–704 (1997).

66. Mullighan, C. G. *et al.* CREBBP mutations in relapsed acute lymphoblastic leukaemia. *Nature* **471,** 235–239 (2011).

67. Pasqualucci, L. *et al.* Inactivating mutations of acetyltransferase genes in B-cell lymphoma. *Nature* **471,** 189–195 (2011).

68. Kishimoto, M. *et al.* Mutations and deletions of the CBP gene in human lung cancer. *Clin. Cancer Res.* **11,** 512–9 (2005).

69. Peifer, M. *et al.* Integrative genome analyses identify key somatic driver mutations of small-cell lung cancer. *Nat. Genet.* **44,** 1104–10 (2012).

70. Jones, D. T. W. *et al.* Dissecting the genomic complexity underlying medulloblastoma. *Nature* **488,** 100–5 (2012).

71. Robinson, G. *et al.* Novel mutations target distinct subgroups of medulloblastoma. *Nature* **488,** 43–48 (2012).

72. Ozdağ, H. *et al.* Mutation analysis of CBP and PCAF reveals rare inactivating mutations in cancer cell lines but not in primary tumours. *Br. J. Cancer* **87,** 1162–5 (2002).

73. Yao, T. P. *et al.* Gene dosage-dependent embryonic development and proliferation defects in mice lacking the transcriptional integrator p300. *Cell* **93,** 361–72 (1998).

74. Yuan, Z.-M. *et al.* Function for p300 and not CBP in the apoptotic response to DNA damage. *Oncogene* **18,** 5714–5717 (1999).

75. Rebel, V. I. *et al.* Distinct roles for CREB-binding protein and p300 in hematopoietic stem cell self-renewal. *Proc. Natl. Acad. Sci.* **99,** 14789–14794 (2002).

76. Merk, D. J. *et al.* Opposing Effects of CREBBP Mutations Govern the Phenotype of Rubinstein-Taybi Syndrome and Adult SHH Medulloblastoma. *Dev. Cell* **44,** 709–724.e6 (2018).

77. Semple, B. D., Blomgren, K., Gimlin, K., Ferriero, D. M. & Noble-Haeusslein, L. J. Brain development in rodents and humans: Identifying benchmarks of maturation and vulnerability to injury across species. *Prog. Neurobiol.* **106–107,** 1–16 (2013).

78. Rice, D., Barone, S. & Jr. Critical periods of vulnerability for the developing nervous system: evidence from humans and animal models. *Environ. Health Perspect.* **108 Suppl,** 511–33 (2000).

79. Rallu, M., Corbin, J. G. & Fishell, G. Parsing the prosencephalon. *Nat. Rev. Neurosci.* **3,** 943–951 (2002).

80. Wilson, S. W. & Houart, C. Early steps in the development of the forebrain. *Dev. Cell* **6,** 167–81 (2004).

81. Wilson, S. W. & Rubenstein, J. L. Induction and dorsoventral patterning of the telencephalon. *Neuron* **28,** 641–51 (2000).

82. Baldock, R. & Davidson, D. in *Anatomy Ontologies for Bioinformatics* 249–265 (Springer London, 2008). doi:10.1007/978-1-84628-885-2_12

83. Downs, K. M. & Davies, T. Staging of gastrulating mouse embryos by morphological landmarks in the dissecting microscope. *Development* **118,** 1255–66 (1993).

84. Mitiku, N. & Baker, J. C. Genomic analysis of gastrulation and organogenesis in the mouse. *Dev. Cell* **13,** 897–907 (2007).

85. Xue, L. *et al.* Global expression profiling reveals genetic programs underlying the developmental divergence between mouse and human embryogenesis. *BMC Genomics* **14,** 568 (2013).

86. Sakai, Y. Neurulation in the mouse: Manner and timing of neural tube closure. *Anat. Rec.* **223,** 194–203 (1989).

87. Martynoga, B., Drechsel, D. & Guillemot, F. Molecular control of neurogenesis: a view from the mammalian cerebral cortex. *Cold Spring Harb. Perspect. Biol.* **4,** a008359 (2012).

88. Monuki, E. S. & Walsh, C. A. Mechanisms of cerebral cortical patterning in mice and humans. *Nat. Neurosci.* **4 Suppl,** 1199–206 (2001).

89. Richards, L., Plachez, C. & Ren, T. Mechanisms regulating the development of the corpus callosum and its agenesis in mouse and human. *Clin. Genet.* **66,** 276–289 (2004).

90. Shu, T. & Richards, L. J. Cortical axon guidance by the glial wedge during the development of the corpus callosum. *J. Neurosci.* **21,** 2749–58 (2001).

91. Lavdas, A. A., Grigoriou, M., Pachnis, V. & Parnavelas, J. G. The medial ganglionic eminence gives rise to a population of early neurons in the developing cerebral cortex. *J. Neurosci.* **19,** 7881–8 (1999).

92. Grove, E. A., Tole, S., Limon, J., Yip, L. & Ragsdale, C. W. The hem of the embryonic cerebral cortex is defined by the expression of multiple Wnt genes and is compromised in Gli3-deficient mice. *Development* **125,** 2315–25 (1998).

93. Mangale, V. S. *et al.* Lhx2 selector activity specifies cortical identity and suppresses hippocampal organizer fate. *Science* **319,** 304–9 (2008).

94. Sugiyama, T., Osumi, N. & Katsuyama, Y. The germinal matrices in the developing dentate gyrus are composed of neuronal progenitors at distinct differentiation stages. *Dev. Dyn.* **242,** 1442–53 (2013).

95. Treloar, H. B., Miller, A. M., Ray, A. & Greer, C. A. *Development of the Olfactory System*. *The Neurobiology of Olfaction* (CRC Press/Taylor & Francis, 2010).

96. Deneen, B. *et al.* The transcription factor NFIA controls the onset of gliogenesis in the developing spinal cord. *Neuron* **52,** 953–68 (2006).

97. Choi, B. H. Prenatal gliogenesis in the developing cerebrum of the mouse. *Glia* **1,** 308–16 (1988).

98. Foran, D. R. & Peterson, A. C. Myelin acquisition in the central nervous system of the mouse revealed by an MBP-Lac Z transgene. *J. Neurosci.* **12,** 4890–7 (1992).

99. Zhuo, L. *et al.* hGFAP-cre transgenic mice for manipulation of glial and neuronal function in vivo. *Genesis* **31,** 85–94 (2001).

100. Brenner, M. & Messing, A. METHODS: A Companion to Methods in GFAP Transgenic Mice. *Enzymology* **10,** 351–364 (1996).

101. Florio, M. & Huttner, W. B. Neural progenitors, neurogenesis and the evolution of the neocortex. *Development* **141,** 2182–2194 (2014).

102. Purves, D. G. J. A. D. F. W. C. H. A.-S. L. J. O. M. L. E. W. (2008). *Neuroscience*. (Sinauer Associates, 2008).

103. Mountcastle, V. B. The columnar organization of the neocortex. *Brain* **120 (Pt 4),** 701–22 (1997).

104. Rakic, P. Confusing cortical columns. *Proc. Natl. Acad. Sci. U. S. A.* **105,** 12099–100 (2008).

105. Brodmann K. *Vergleichende Lokalisationslehre der Grosshirnrinde in ihren Prinzipien dargestellt auf Grund des Zellenbaues.* (J.A. Barth, 1909).

106. Gilbert, C. D. & Wiesel, T. N. Morphology and intracortical projections of functionally characterised neurones in the cat visual cortex. *Nature* **280,** 120–5 (1979).

107. Douglas, R. J. & Martin, K. A. C. Neuronal circuits of the neocortex. *Annu. Rev. Neurosci.* **27,** 419–51 (2004).

108. Rakic, P. Mode of cell migration to the superficial layers of fetal monkey neocortex. *J. Comp. Neurol.* **145,** 61–83 (1972).

109. Noctor, S. C., Martínez-Cerdeño, V., Ivic, L. & Kriegstein, A. R. Cortical neurons arise in symmetric and asymmetric division zones and migrate through specific phases. *Nat. Neurosci.* **7,** 136–144 (2004).

110. Molyneaux, B. J., Arlotta, P., Menezes, J. R. L. & Macklis, J. D. Neuronal subtype specification in the cerebral cortex. *Nat. Rev. Neurosci.* **8,** 427–437 (2007).

111. Malatesta, P., Hartfuss, E. & Gotz, M. Isolation of radial glial cells by fluorescent-activated cell sorting reveals a neuronal lineage. *Development* **127,** (2000).

112. Noctor, S. C., Flint, A. C., Weissman, T. A., Dammerman, R. S. & Kriegstein, A. R. Neurons derived from radial glial cells establish radial units in neocortex. *Nature* **409,** 714–20 (2001).

113. Gal, J. S. *et al.* Molecular and morphological heterogeneity of neural precursors in the mouse neocortical proliferative zones. *J. Neurosci.* **26,** 1045–56 (2006).

114. Tyler, W. A. & Haydar, T. F. Multiplex genetic fate mapping reveals a novel route of neocortical neurogenesis, which is altered in the Ts65Dn mouse model of Down syndrome. *J. Neurosci.* **33,** 5106–19 (2013).

115. Haubensak, W., Attardo, A., Denk, W. & Huttner, W. B. Neurons arise in the basal neuroepithelium of the early mammalian telencephalon: a major site of neurogenesis. *Proc. Natl. Acad. Sci. U. S. A.* **101,** 3196–201 (2004).

116. Kowalczyk, T. *et al.* Intermediate Neuronal Progenitors (Basal Progenitors) Produce Pyramidal–Projection Neurons for All Layers of Cerebral Cortex. *Cereb. Cortex* **19,** 2439–2450 (2009).

117. Marin-Padilla, M. Dual origin of the mammalian neocortex and evolution of the cortical plate. *Anat. Embryol. (Berl).* **152,** 109–126 (1978).

118. Caviness, V. S. Neocortical histogenesis in normal and reeler mice: a developmental study based upon [3H]thymidine autoradiography. *Brain Res.* **256,** 293–302 (1982).

119. Angevine, J. B. & Sidman, R. L. Autoradiographic study of cell migration during histogenesis of cerebral cortex in the mouse. *Nature* **192,** 766–8 (1961).

120. Smart, I. H. & McSherry, G. M. Growth patterns in the lateral wall of the mouse telencephalon. II. Histological changes during and subsequent to the period of isocortical neuron production. *J. Anat.* **134,** 415–42 (1982).

121. Lambert de Rouvroit, C. & Goffinet, A. M. The reeler mouse as a model of brain development. *Adv. Anat. Embryol. Cell Biol.* **150,** 1–106 (1998).

122. Lee, G. H. & D'Arcangelo, G. New Insights into Reelin-Mediated Signaling Pathways. *Front. Cell. Neurosci.* **10,** 122 (2016).

123. Anderson, S. A., Eisenstat, D. D., Shi, L. & Rubenstein, J. L. Interneuron migration from basal forebrain to neocortex: dependence on Dlx genes. *Science* **278,** 474–6 (1997).

124. Wichterle, H., Turnbull, D. H., Nery, S., Fishell, G. & Alvarez-Buylla, A. In utero fate mapping reveals distinct migratory pathways and fates of neurons born in the mammalian basal forebrain. *Development* **128,** 3759–71 (2001).

125. Stühmer, T., Puelles, L., Ekker, M. & Rubenstein, J. L. R. Expression from a Dlx gene enhancer marks adult mouse cortical GABAergic neurons. *Cereb. Cortex* **12,** 75–85 (2002).

126. Spassky, N. *et al.* Multiple restricted origin of oligodendrocytes. *J. Neurosci.* **18,** 8331–43 (1998).

127. Rakic, P. Radial unit hypothesis of neocortical expansion. *Novartis Found. Symp.* **228,** 30-42; discussion 42-52 (2000).

128. Borrell, V. & Reillo, I. Emerging roles of neural stem cells in cerebral cortex development and evolution. *Dev. Neurobiol.* **72,** 955–71 (2012).

129. Reillo, I., de Juan Romero, C., García-Cabezas, M. Á. & Borrell, V. A Role for Intermediate Radial Glia in the Tangential Expansion of the Mammalian Cerebral Cortex. *Cereb. Cortex* **21,** 1674–1694 (2011).

130. Hansen, D. V., Lui, J. H., Parker, P. R. L. & Kriegstein, A. R. Neurogenic radial glia in the outer subventricular zone of human neocortex. *Nature* **464,** 554–561 (2010).

131. Betizeau, M. *et al.* Precursor Diversity and Complexity of Lineage Relationships in the Outer Subventricular Zone of the Primate. *Neuron* **80,** 442–457 (2013).

132. Shitamukai, A., Konno, D. & Matsuzaki, F. Oblique Radial Glial Divisions in the Developing Mouse Neocortex Induce Self-Renewing Progenitors outside the Germinal Zone That Resemble Primate Outer Subventricular Zone Progenitors. *J. Neurosci.* **31,** 3683–3695 (2011).

133. LaMonica, B. E., Lui, J. H., Hansen, D. V & Kriegstein, A. R. Mitotic spindle orientation predicts outer radial glial cell generation in human neocortex. *Nat. Commun.* **4,** 1665 (2013).

134. Pilz, G.-A. *et al.* Amplification of progenitors in the mammalian telencephalon includes a new radial glial cell type. *Nat. Commun.* **4,** 2125 (2013).

135. Treves, A., Tashiro, A., Witter, M. P. & Moser, E. I. What is the mammalian dentate gyrus good for? *Neuroscience* **154,** 1155–72 (2008).

136. O'Keefe, J. Place units in the hippocampus of the freely moving rat. *Exp. Neurol.* **51,** 78–109 (1976).

137. Sargolini, F. *et al.* Conjunctive representation of position, direction, and velocity in entorhinal cortex. *Science* **312,** 758–62 (2006).

138. Carpenter, M. *Human Neuroanatomy, 7th Ed; Chapter 18: Olfactory Pathways, Hippocampal Formation and Amygdala.* (Williams & Wilkins, 1976).

139. Solodkin, A. & Van Hoesen, G. W. in *Encyclopedia of Neuroscience* 1121–1123 (Elsevier, 2004). doi:10.1016/B978-008045046-9.02032-5

140. Cajal, S. in *Cajal on the Cerebral Cortex: An Annotated Translation of the Complete Writings.* (ed. DeFelipe, J.; Jones, E.) pp289-362 (Oxford University Press, 1988).

141. Witter, M. P. *et al.* Cortico-hippocampal communication by way of parallel parahippocampal-subicular pathways. *Hippocampus* **10,** 398–410 (2000).

142. Sloviter, R. S. & Lømo, T. Updating the lamellar hypothesis of hippocampal organization. *Front. Neural Circuits* **6,** 102 (2012).

143. O'Mara, S. The subiculum: what it does, what it might do, and what neuroanatomy has yet to tell us. *J. Anat.* **207,** 271–82 (2005).

144. Grove, E. A., Tole, S., Limon, J., Yip, L. & Ragsdale, C. W. The hem of the embryonic cerebral cortex is defined by the expression of multiple Wnt genes and is compromised in Gli3-deficient mice. *Development* **125,** 2315–25 (1998).

145. Mangale, V. S. *et al.* Lhx2 selector activity specifies cortical identity and suppresses hippocampal organizer fate. *Science* **319,** 304–9 (2008).

146. Caronia, G., Wilcoxon, J., Feldman, P. & Grove, E. A. Bone morphogenetic protein signaling in the developing telencephalon controls formation of the hippocampal dentate gyrus and modifies fear-related behavior. *J. Neurosci.* **30,** 6291–301 (2010).

147. Furuta, Y., Piston, D. W. & Hogan, B. L. Bone morphogenetic proteins (BMPs) as regulators of dorsal forebrain development. *Development* **124,** 2203–12 (1997).

148. Lee, S. M., Tole, S., Grove, E. & McMahon, A. P. A local Wnt-3a signal is required for development of the mammalian hippocampus. *Development* **127,** 457–67 (2000).

149. Pleasure, S. J. *et al.* Cell migration from the ganglionic eminences is required for the development of hippocampal GABAergic interneurons. *Neuron* **28,** 727–40 (2000).

150. Hayashi, K., Kubo, K.-I., Kitazawa, A. & Nakajima, K. Cellular dynamics of neuronal migration in the hippocampus. *Front. Neurosci.* **9,** 135 (2015).

151. Li, G. & Pleasure, S. J. Genetic regulation of dentate gyrus morphogenesis. *Prog. Brain Res.* **163,** 143–52 (2007).

152. Yu, D. X., Marchetto, M. C. & Gage, F. H. How to make a hippocampal dentate gyrus granule neuron. *Development* **141,** 2366–75 (2014).

153. Urbán, N. & Guillemot, F. Neurogenesis in the embryonic and adult brain: same regulators, different roles. *Front. Cell. Neurosci.* **8,** 396 (2014).

154. Galceran, J., Miyashita-Lin, E. M., Devaney, E., Rubenstein, J. L. & Grosschedl, R. Hippocampus development and generation of dentate gyrus granule cells is regulated by LEF1. *Development* **127,** 469–82 (2000).

155. Sugiyama, T., Osumi, N. & Katsuyama, Y. The germinal matrices in the developing dentate gyrus are composed of neuronal progenitors at distinct differentiation stages. *Dev. Dyn.* **242,** 1442–53 (2013).

156. Seki, T. *et al.* Distinctive population of Gfap-expressing neural progenitors arising around the dentate notch migrate and form the granule cell layer in the developing hippocampus. *J. Comp. Neurol.* **522,** 261–83 (2014).

157. Del Río, J. A. *et al.* A role for Cajal-Retzius cells and reelin in the development of hippocampal connections. *Nature* **385,** 70–4 (1997).

158. Hodge, R. D. *et al.* Tbr2 expression in Cajal-Retzius cells and intermediate neuronal progenitors is required for morphogenesis of the dentate gyrus. *J. Neurosci.* **33,** 4165–80 (2013).

159. Altman, J. & Bayer, S. A. Migration and distribution of two populations of hippocampal granule cell precursors during the perinatal and postnatal periods. *J. Comp. Neurol.* **301,** 365–81 (1990).

160. Humphrey, T. The development of the human hippocampal fissure. *J. Anat.* **101,** 655–76 (1967).

161. Harding, J. W., Getchell, T. V & Margolis, F. L. Denervation of the primary olfactory pathway in mice. V. Long-term effect of intranasal ZnSO4 irrigation on behavior, biochemistry and morphology. *Brain Res.* **140,** 271–85 (1978).

162. Wilson, D. A., Kadohisa, M. & Fletcher, M. L. Cortical contributions to olfaction: plasticity and perception. *Semin. Cell Dev. Biol.* **17,** 462–70 (2006).

163. Theiler K. The House Mouse. Development and Normal Stages from Fertilization to 4 Weeks of Age. Berlin-Heidelberg-New York; Springer: 1972. (1972).

164. Valverde, F., Santacana, M. & Heredia, M. Formation of an olfactory glomerulus: morphological aspects of development and organization. *Neuroscience* **49,** 255–75 (1992).

165. Whitesides, J. G. & LaMantia, A. S. Differential adhesion and the initial assembly of the mammalian olfactory nerve. *J. Comp. Neurol.* **373,** 240–54 (1996).

166. Balmer, C. W. & LaMantia, A.-S. Loss of Gli3 and Shh function disrupts olfactory axon trajectories. *J. Comp. Neurol.* **472,** 292–307 (2004).

167. Purves, D. *et al. The Olfactory Bulb - Neuroscience 2nd edition*. (Sinauer Associates, 2001).

168. Urban, N. N. Lateral inhibition in the olfactory bulb and in olfaction. *Physiol. Behav.* **77,** 607–12 (2002).

169. Egger, V., Svoboda, K. & Mainen, Z. F. Mechanisms of lateral inhibition in the olfactory bulb: efficiency and modulation of spike-evoked calcium influx into granule cells. *J. Neurosci.* **23,** 7551–8 (2003).

170. Hinds, J. W. Autoradiographic study of histogenesis in the mouse olfactory bulb I. Time of origin of neurons and neuroglia. *J. Comp. Neurol.* **134,** 287–304 (1968).

171. Jiménez, D. *et al.* Evidence for intrinsic development of olfactory structures in Pax-6 mutant mice. *J. Comp. Neurol.* **428,** 511–26 (2000).

172. Long, J. E., Garel, S., Depew, M. J., Tobet, S. & Rubenstein, J. L. R. DLX5 regulates development of peripheral and central components of the olfactory system. *J. Neurosci.* **23,** 568–78 (2003).

173. Shay, E. L., Greer, C. A. & Treloar, H. B. Dynamic expression patterns of ECM molecules in the developing mouse olfactory pathway. *Dev. Dyn.* **237,** 1837–50 (2008).

174. Blanchart, A., De Carlos, J. A. & López-Mascaraque, L. Time frame of mitral cell development in the mice olfactory bulb. *J. Comp. Neurol.* **496,** 529–43 (2006).

175. Altman, J. Autoradiographic and histological studies of postnatal neurogenesis. IV. Cell proliferation and migration in the anterior forebrain, with special reference to persisting neurogenesis in the olfactory bulb. *J. Comp. Neurol.* **137,** 433–457 (1969).

176. Hatten, M. E. CENTRAL NERVOUS SYSTEM NEURONAL MIGRATION. *Annu. Rev. Neurosci.* **22,** 511–539 (1999).

177. Pencea, V. & Luskin, M. B. Prenatal development of the rodent rostral migratory stream. *J. Comp. Neurol.* **463,** 402–418 (2003).

178. Deacon, T. W., Pakzaban, P. & Isacson, O. The lateral ganglionic eminence is the origin of cells committed to striatal phenotypes: neural transplantation and developmental evidence. *Brain Res.* **668,** 211–9 (1994).

179. Tucker, E. S., Polleux, F. & LaMantia, A.-S. Position and time specify the migration of a pioneering population of olfactory bulb interneurons. *Dev. Biol.* **297,** 387–401 (2006).

180. Bédard, A. & Parent, A. Evidence of newly generated neurons in the human olfactory bulb. *Dev. Brain Res.* **151,** 159–168 (2004).

181. Curtis, M. A. *et al.* Human neuroblasts migrate to the olfactory bulb via a lateral ventricular extension. *Science* **315,** 1243–9 (2007).

182. Altman, J. & Das, G. D. Autoradiographic and histological evidence of postnatal hippocampal neurogenesis in rats. *J. Comp. Neurol.* **124,** 319–335 (1965).

183. Morrison, S. J. & Spradling, A. C. Stem Cells and Niches: Mechanisms That Promote Stem Cell Maintenance throughout Life. *Cell* **132,** 598–611 (2008).

184. Ming, G. & Song, H. Adult Neurogenesis in the Mammalian Brain: Significant Answers and Significant Questions. *Neuron* **70,** 687–702 (2011).

185. Fuentealba, L. C., Obernier, K. & Alvarez-Buylla, A. Adult Neural Stem Cells Bridge Their Niche. *Cell Stem Cell* **10,** 698–708 (2012).

186. Brill, M. S. *et al.* Adult generation of glutamatergic olfactory bulb interneurons. *Nat. Neurosci.* **12,** 1524–1533 (2009).

187. Eriksson, P. S. *et al.* Neurogenesis in the adult human hippocampus. *Nat. Med.* **4,** 1313–1317 (1998).

188. Spalding, K. L. *et al.* Dynamics of Hippocampal Neurogenesis in Adult Humans. *Cell* **153,** 1219–1227 (2013).

189. Alvarez-Buylla, A. & Lim, D. A. For the long run: maintaining germinal niches in the adult brain. *Neuron* **41,** 683–6 (2004).

190. Ma, D. K., Ming, G.-L. & Song, H. Glial influences on neural stem cell development: cellular niches for adult neurogenesis. *Curr. Opin. Neurobiol.* **15,** 514–20 (2005).

191. Zhao, C., Deng, W. & Gage, F. H. Mechanisms and Functional Implications of Adult Neurogenesis. *Cell* **132,** 645–660 (2008).

192. Taverna, E., Götz, M. & Huttner, W. B. The Cell Biology of Neurogenesis: Toward an Understanding of the Development and Evolution of the Neocortex. *Annu. Rev. Cell Dev. Biol.* **30,** 465–502 (2014).

193. López-Juárez, A. *et al.* Gsx2 controls region-specific activation of neural stem cells and injury-induced neurogenesis in the adult subventricular zone. *Genes Dev.* **27,** 1272–87 (2013).

194. Merkle, F. T. *et al.* Adult neural stem cells in distinct microdomains generate previously unknown interneuron types. *Nat. Neurosci.* **17,** 207–214 (2013).

195. Simons, B. D. & Clevers, H. Strategies for homeostatic stem cell self-renewal in adult tissues. *Cell* **145,** 851–62 (2011).

196. Seri, B., García-Verdugo, J. M., Collado-Morente, L., McEwen, B. S. & Alvarez-Buylla, A. Cell types, lineage, and architecture of the germinal zone in the adult dentate gyrus. *J. Comp. Neurol.* **478,** 359–78 (2004).

197. Li, G., Fang, L., Fernández, G. & Pleasure, S. J. The Ventral Hippocampus Is the Embryonic Origin for Adult Neural Stem Cells in the Dentate Gyrus. *Neuron* **78,** 658–672 (2013).

198. Hsieh, J. Orchestrating transcriptional control of adult neurogenesis. *Genes Dev.* **26,** 1010–21 (2012).

199. Sierra, A. *et al.* Microglia Shape Adult Hippocampal Neurogenesis through Apoptosis-Coupled Phagocytosis. *Cell Stem Cell* **7,** 483–495 (2010).

200. Sierra, A. *et al.* Surveillance, Phagocytosis, and Inflammation: How Never-Resting Microglia Influence Adult Hippocampal Neurogenesis. *Neural Plast.* **2014,** 1–15 (2014).

201. Jessberger, S. *et al.* Dentate gyrus-specific knockdown of adult neurogenesis impairs spatial and object recognition memory in adult rats. *Learn. Mem.* **16,** 147–54 (2009).

202. Sahay, A. *et al.* Increasing adult hippocampal neurogenesis is sufficient to improve pattern separation. *Nature* **472,** 466–470 (2011).

203. Lugert, S. *et al.* Quiescent and Active Hippocampal Neural Stem Cells with Distinct Morphologies Respond Selectively to Physiological and Pathological Stimuli and Aging. *Cell Stem Cell* **6,** 445–456 (2010).

204. Encinas, J. M. *et al.* Division-Coupled Astrocytic Differentiation and Age-Related Depletion of Neural Stem Cells in the Adult Hippocampus. *Cell Stem Cell* **8,** 566–579 (2011).

205. Seib, D. R. M. *et al.* Loss of Dickkopf-1 Restores Neurogenesis in Old Age and Counteracts Cognitive Decline. *Cell Stem Cell* **12,** 204–214 (2013).

206. Peretto, P., Giachino, C., Aimar, P., Fasolo, A. & Bonfanti, L. Chain formation and glial tube assembly in the shift from neonatal to adult subventricular zone of the rodent forebrain. *J. Comp. Neurol.* **487,** 407–27 (2005).

207. Doetsch, F., Caillé, I., Lim, D. A., García-Verdugo, J. M. & Alvarez-Buylla, A. Subventricular zone astrocytes are neural stem cells in the adult mammalian brain. *Cell* **97,** 703–16 (1999).

208. Tramontin, A. D., García-Verdugo, J. M., Lim, D. A. & Alvarez-Buylla, A. Postnatal development of radial glia and the ventricular zone (VZ): a continuum of the neural stem cell compartment. *Cereb. Cortex* **13,** 580–7 (2003).

209. Mirzadeh, Z., Merkle, F. T., Soriano-Navarro, M., Garcia-Verdugo, J. M. & Alvarez-Buylla, A. Neural stem cells confer unique pinwheel architecture to the ventricular surface in neurogenic regions of the adult brain. *Cell Stem Cell* **3,** 265–78 (2008).

210. Fuentealba, L. C. *et al.* Embryonic Origin of Postnatal Neural Stem Cells. *Cell* **161,** 1644–1655 (2015).

211. Furutachi, S. *et al.* Slowly dividing neural progenitors are an embryonic origin of adult neural stem cells. *Nat. Neurosci.* **18,** 657–65 (2015).

212. Doetsch, F., García-Verdugo, J. M. & Alvarez-Buylla, A. Cellular composition and three-dimensional organization of the subventricular germinal zone in the adult mammalian brain. *J. Neurosci.* **17,** 5046–61 (1997).

213. Ponti, G., Obernier, K. & Alvarez-Buylla, A. Lineage progression from stem cells to new neurons in the adult brain ventricular-subventricular zone. *Cell Cycle* **12,** 1649–1650 (2013).

214. Codega, P. *et al.* Prospective identification and purification of quiescent adult neural stem cells from their in vivo niche. *Neuron* **82,** 545–59 (2014).

215. Mich, J. K. *et al.* Prospective identification of functionally distinct stem cells and neurosphere-initiating cells in adult mouse forebrain. *Elife* **3,** e02669 (2014).

216. Ortega, F. *et al.* Oligodendrogliogenic and neurogenic adult subependymal zone neural stem cells constitute distinct lineages and exhibit differential responsiveness to Wnt signalling. *Nat. Cell Biol.* **15,** 602–13 (2013).

217. Merkle, F. T., Mirzadeh, Z. & Alvarez-Buylla, A. Mosaic Organization of Neural Stem Cells in the Adult Brain. *Science (80-.).* **317,** 381–384 (2007).

218. Alvarez-Buylla, A., Kohwi, M., Nguyen, T. M. & Merkle, F. T. The Heterogeneity of Adult Neural Stem Cells and the Emerging Complexity of Their Niche. *Cold Spring Harb. Symp. Quant. Biol.* **73,** 357–365 (2008).

219. Menn, B. *et al.* Origin of Oligodendrocytes in the Subventricular Zone of the Adult Brain. *J. Neurosci.* **26,** 7907–7918 (2006).

220. REGULATION (EC) No 141/2000 OF THE EUROPEAN PARLIAMENT AND OF THE COUNCIL of 16 December 1999 on orphan medicinal products. *Off. J. Eur. Communities* **22,** (2000).

221. Orphanet: About rare diseases. Available at: http://www.orpha.net/consor/cgi-bin/Education_AboutRareDiseases.php?lng=EN. (Accessed: 23rd November 2017)

222. Van Weely, S., Leufkens, H. G. M., De Vrueh, R., Baekelandt, E. R. F. & De Haan, J. M. H. Background Paper 6.19 Rare Diseases. (2013).

223. Kalkhoven, E. *et al.* Loss of CBP acetyltransferase activity by PHD finger mutations in Rubinstein-Taybi syndrome. *Hum. Mol. Genet.* **12,** 441–50 (2003).

224. Tanaka, Y. *et al.* Abnormal skeletal patterning in embryos lacking a single Cbp allele: a partial similarity with Rubinstein-Taybi syndrome. *Proc. Natl. Acad. Sci. U. S. A.* **94,** 10215–20 (1997).

225. Oike, Y. *et al.* Truncated CBP protein leads to classical Rubinstein-Taybi syndrome phenotypes in mice: implications for a dominant-negative mechanism. *Hum. Mol. Genet.* **8,** 387–96 (1999).

226. Barco, A. The Rubinstein-Taybi syndrome: modeling mental impairment in the mouse. *Genes. Brain. Behav.* **6 Suppl 1,** 32–9 (2007).

227. Zhang, Z., Hofmann, C., Casanova, E., Schutz, G. & Lutz, B. Generation of a conditional allele of the CBP gene in mouse. *Genesis* **40,** 82–89 (2004).

228. Lehmkuhl, A. M., Dirr, E. R. & Fleming, S. M. Olfactory Assays for Mouse Models of Neurodegenerative Disease. *J. Vis. Exp.* e51804 (2014). doi:10.3791/51804

229. Yang, M. & Crawley, J. N. in *Current Protocols in Neuroscience* **Chapter 8,** Unit 8.24 (John Wiley & Sons, Inc., 2009).

230. Crawley, J. & Goodwin, F. K. Preliminary report of a simple animal behavior model for the anxiolytic effects of benzodiazepines. *Pharmacol. Biochem. Behav.* **13,** 167–70 (1980).

231. Bourin, M. & Hascoët, M. The mouse light / dark box test. *Eur. J. Pharmacol.* **463,** 55–65 (2003).

232. Tanaka, Y. *et al.* Extensive brain hemorrhage and embryonic lethality in a mouse null mutant of CREB-binding protein. *Mech. Dev.* **95,** 133–45 (2000).

233. Duan, X., Kang, E., Liu, C. Y., Ming, G. & Song, H. Development of neural stem cell in the adult brain. *Curr. Opin. Neurobiol.* **18,** 108–115 (2008).

234. Liu, Y. *et al.* Glial fibrillary acidic protein-expressing neural progenitors give rise to immature neurons via early intermediate progenitors expressing both glial fibrillary acidic protein and neuronal markers in the adult hippocampus. *Neuroscience* **166,** 241–251 (2010).

235. Kriegstein, A. R. & Götz, M. Radial glia diversity: A matter of cell fate. *Glia* **43,** 37–43 (2003).

236. Deber, C. M. & Reynolds, S. J. Central nervous system myelin: structure, function, and pathology. *Clin. Biochem.* **24,** 113–34 (1991).

237. Párraga, H. C., Párraga, M. I. & Jensen, A. R. Cognitive, behavioral, and psychiatric symptoms in two children with agenesis of the corpus callosum: case report. *Int. J. Psychiatry Med.* **33,** 107–13 (2003).

238. Hinkley, L. B. N. *et al.* The role of corpus callosum development in functional connectivity and cognitive processing. *PLoS One* **7,** e39804 (2012).

239. Milani, D. *et al.* Rubinstein-Taybi syndrome: clinical features, genetic basis, diagnosis, and management. *Ital. J. Pediatr.* **41,** 4 (2015).

240. Mishra, S., Agarwalla, S. K., Potpalle, D. R. & Dash, N. N. Rubinstein-Taybi syndrome with agenesis of corpus callosum. *J. Pediatr. Neurosci.* **10,** 175–7 (2015).

241. Ajmone, P. F. *et al.* Rubinstein-Taybi syndrome: New neuroradiological and neuropsychiatric insights from a multidisciplinary approach. *Am. J. Med. Genet. Part B Neuropsychiatr. Genet.* **177,** 406–415 (2018).

242. Sohn, J. *et al.* The subventricular zone continues to generate corpus callosum and rostral migratory stream astroglia in normal adult mice. *J. Neurosci.* **35,** 3756–63 (2015).

243. Levers, T. E., Edgar, J. M. & Price, D. J. The fates of cells generated at the end of neurogenesis in developing mouse cortex. *J. Neurobiol.* **48,** 265–77 (2001).

244. Lyck, L., Krøigård, T. & Finsen, B. Unbiased cell quantification reveals a continued increase in the number of neocortical neurones during early post-natal development in mice. *Eur. J. Neurosci.* **26,** 1749–1764 (2007).

245. Valor, L. M. *et al.* Ablation of CBP in Forebrain Principal Neurons Causes Modest Memory and Transcriptional Defects and a Dramatic Reduction of Histone Acetylation But Does Not Affect Cell Viability. *J. Neurosci.* **31,** 1652–1663 (2011).

246. Lim, R. W. L. & Halpain, S. Regulated Association of Microtubule-associated Protein 2 (MAP2) with Src and Grb2: Evidence for MAP2 as a Scaffolding Protein. *J. Biol. Chem.* **275,** 20578–20587 (2000).

247. Arens, J. Die Rolle von Mikrotubuli-regulierenden Proteinen während der neuronalen Differenzierung. (2012). doi:10.17877/DE290R-4179

248. McMahon, H. T. *et al.* Synaptophysin, a major synaptic vesicle protein, is not essential for neurotransmitter release. *Proc. Natl. Acad. Sci. U. S. A.* **93,** 4760–4 (1996).

249. Thomson, M. *et al.* Pluripotency Factors in Embryonic Stem Cells Regulate Differentiation into Germ Layers. *Cell* **145,** 875–889 (2011).

250. Zhao, S., Nichols, J., Smith, A. G. & Li, M. SoxB transcription factors specify neuroectodermal lineage choice in ES cells. *Mol. Cell. Neurosci.* **27,** 332–342 (2004).

251. Gage, F. H., Kempermann, G., Palmer, T. D., Peterson, D. A. & Ray, J. Multipotent progenitor cells in the adult dentate gyrus. *J. Neurobiol.* **36,** 249–66 (1998).

252. Miller, J. A. *et al.* Conserved molecular signatures of neurogenesis in the hippocampal subgranular zone of rodents and primates. *Development* **140,** 4633–44 (2013).

253. Suh, H. *et al.* In Vivo Fate Analysis Reveals the Multipotent and Self-Renewal Capacities of Sox2+ Neural Stem Cells in the Adult Hippocampus. *Cell Stem Cell* **1,** 515–528 (2007).

254. Osman, A. A. *et al.* Wolframin expression induces novel ion channel activity in endoplasmic reticulum membranes and increases intracellular calcium. *J. Biol. Chem.* **278,** 52755–62 (2003).

255. Takeda, K. *et al.* WFS1 (Wolfram syndrome 1) gene product: predominant subcellular localization to endoplasmic reticulum in cultured cells and neuronal expression in rat brain. *Hum. Mol. Genet.* **10,** 477–84 (2001).

256. Good, P. J. A conserved family of elav-like genes in vertebrates. *Proc. Natl. Acad. Sci. U. S. A.* **92,** 4557–61 (1995).

257. Hinman, M. N. & Lou, H. Diverse molecular functions of Hu proteins. *Cell. Mol. Life Sci.* **65,** 3168–3181 (2008).

258. Ohtsuka, T., Yano, M. & Okano, H. Acute reduction of neuronal RNA binding Elavl2 protein and Gap43 mRNA in mouse hippocampus after kainic acid treatment. *Biochem. Biophys. Res. Commun.* **466,** 46–51 (2015).

259. Oliver, G. *et al.* Prox 1, a prospero-related homeobox gene expressed during mouse development. *Mech. Dev.* **44,** 3–16 (1993).

260. Li, G., Kataoka, H., Coughlin, S. R. & Pleasure, S. J. Identification of a transient subpial neurogenic zone in the developing dentate gyrus and its regulation by Cxcl12 and reelin signaling. *Development* **136,** 327–35 (2009).

261. Lavado, A., Lagutin, O. V, Chow, L. M. L., Baker, S. J. & Oliver, G. Prox1 is required for granule cell maturation and intermediate progenitor maintenance during brain neurogenesis. *PLoS Biol.* **8,** (2010).

262. Yang, M. J. *et al.* Mitral and tufted cells are potential cellular targets of nitration in the olfactory bulb of aged mice. *PLoS One* **8,** e59673 (2013).

263. Englund, C. *et al.* Pax6, Tbr2, and Tbr1 Are Expressed Sequentially by Radial Glia, Intermediate Progenitor Cells, and Postmitotic Neurons in Developing Neocortex. *J. Neurosci.* **25,** 247–251 (2005).

264. Mizuguchi, R. *et al.* Tbr2 deficiency in mitral and tufted cells disrupts excitatory-inhibitory balance of neural circuitry in the mouse olfactory bulb. *J. Neurosci.* **32,** 8831–44 (2012).

265. Kosaka, T. & Kosaka, K. Heterogeneity of calbindin-containing neurons in the mouse main olfactory bulb: I. General description. *Neurosci. Res.* **67,** 275–292 (2010).

266. Panzanelli, P., Fritschy, J. M., Yanagawa, Y., Obata, K. & Sassoè-Pognetto, M. GABAergic phenotype of periglomerular cells in the rodent olfactory bulb. *J. Comp. Neurol.* **502,** 990–1002 (2007).

267. Murphy, G. J., Darcy, D. P. & Isaacson, J. S. Intraglomerular inhibition: signaling mechanisms of an olfactory microcircuit. *Nat. Neurosci.* **8,** 354–64 (2005).

268. Marenholz, I., Heizmann, C. W. & Fritz, G. S100 proteins in mouse and man: from evolution to function and pathology (including an update of the nomenclature). *Biochem. Biophys. Res. Commun.* **322,** 1111–1122 (2004).

269. Raponi, E. *et al.* S100B expression defines a state in which GFAP-expressing cells lose their neural stem cell potential and acquire a more mature developmental stage. *Glia* **55,** 165–77 (2007).

270. Yokoo, H. *et al.* Anti-human Olig2 antibody as a useful immunohistochemical marker of normal oligodendrocytes and gliomas. *Am. J. Pathol.* **164,** 1717–25 (2004).

271. Zhou, Q., Wang, S. & Anderson, D. J. Identification of a novel family of oligodendrocyte lineage-specific basic helix-loop-helix transcription factors. *Neuron* **25,** 331–43 (2000).

272. Kapuscinski, J. DAPI: a DNA-specific fluorescent probe. *Biotech. Histochem.* **70,** 220–33 (1995).

273. May, V. E. L. *et al.* Impaired olfactory bulb neurogenesis depends on the presence of human wild-type alpha-synuclein. *Neuroscience* **222,** 343–55 (2012).

274. Wiley, S., Swayne, S., Rubinstein, J. H., Lanphear, N. E. & Stevens, C. A. Rubinstein-Taybi syndrome medical guidelines. *Am. J. Med. Genet.* **119A,** 101–110 (2003).

275. Beets, L., Rodríguez-Fonseca, C. & Hennekam, R. C. Growth charts for individuals with Rubinstein-Taybi syndrome. *Am. J. Med. Genet. Part A* **164,** 2300–2309 (2014).

276. Lee, J. S. *et al.* Clinical and mutational spectrum in Korean patients with Rubinstein-Taybi syndrome: the spectrum of brain MRI abnormalities. *Brain Dev.* **37,** 402–8 (2015).

277. Wójcik, C. *et al.* Rubinstein-Taybi syndrome associated with Chiari type I malformation caused by a large 16p13.3 microdeletion: a contiguous gene syndrome? *Am. J. Med. Genet. A* **152A,** 479–83 (2010).

278. Korzus, E. *et al.* Transcription factor-specific requirements for coactivators and their acetyltransferase functions. *Science* **279,** 703–7 (1998).

279. Coupry, I. *et al.* Molecular analysis of the CBP gene in 60 patients with Rubinstein-Taybi syndrome. *J. Med. Genet.* **39,** 415–21 (2002).

280. Wood, M. A. *et al.* Transgenic mice expressing a truncated form of CREB-binding protein (CBP) exhibit deficits in hippocampal synaptic plasticity and memory storage. *Learn. Mem.* **12,** 111–9 (2005).

281. Ateca-Cabarga, J. C. *et al.* Brain size regulations by cbp haploinsufficiency evaluated by in-vivo MRI based volumetry. *Sci. Rep.* **5,** 16256 (2015).

282. Wang, J. *et al.* CBP Histone Acetyltransferase Activity Regulates Embryonic Neural Differentiation in the Normal and Rubinstein-Taybi Syndrome Brain. *Dev. Cell* **18,** 114–125 (2010).

283. Alari, V. *et al.* iPSC-derived neurons of CREBBP - and EP300 -mutated Rubinstein-Taybi syndrome patients show morphological alterations and hypoexcitability. *Stem Cell Res.* **30,** 130–140 (2018).

284. Cremer, H. *et al.* Inactivation of the N-CAM gene in mice results in size reduction of the olfactory bulb and deficits in spatial learning. *Nature* **367,** 455–459 (1994).

285. Koizumi, H. *et al.* Doublecortin maintains bipolar shape and nuclear translocation during migration in the adult forebrain. *Nat. Neurosci.* **9,** 779–86 (2006).

286. Capilla-Gonzalez, V., Lavell, E., Quiñones-Hinojosa, A. & Guerrero-Cazares, H. in *Advances in experimental medicine and biology* **853,** 1–21 (2015).

287. Korzus, E., Rosenfeld, M. G. & Mayford, M. CBP histone acetyltransferase activity is a critical component of memory consolidation. *Neuron* **42,** 961–72 (2004).

288. Viosca, J., Lopez-Atalaya, J. P., Olivares, R., Eckner, R. & Barco, A. Syndromic features and mild cognitive impairment in mice with genetic reduction on p300 activity: Differential contribution of p300 and CBP to Rubinstein-Taybi syndrome etiology. *Neurobiol. Dis.* **37,** 186–94 (2010).

289. Gotts, E. E. & Liemohn, W. P. Behavioral characteristics of three children with the broad thumb-hallux (Rubinstein-Taybi) syndrome. *Biol. Psychiatry* **12,** 413–23 (1977).

290. Hennekam, R. C. *et al.* Psychological and speech studies in Rubinstein-Taybi syndrome. *Am. J. Ment. Retard.* **96,** 645–60 (1992).

291. Spalice, A. *et al.* Neuronal migration disorders: clinical, neuroradiologic and genetics aspects. *Acta Paediatr.* **98,** 421–433 (2009).

292. Verrotti, A. *et al.* New trends in neuronal migration disorders. *Eur. J. Paediatr. Neurol.* **14,** 1–12 (2010).

293. Schell-Apacik, C. C. *et al.* Agenesis and dysgenesis of the corpus callosum: clinical, genetic and neuroimaging findings in a series of 41 patients. *Am. J. Med. Genet. A* **146A,** 2501–11 (2008).

294. Dobyns, W. & Truwit, C. Lissencephaly and Other Malformations of Cortical Development: 1995 Update. *Neuropediatrics* **26,** 132–147 (1995).

295. Solomon, B. D., Gropman, A. & Muenke, M. Holoprosencephaly Overview. (2013).

296. Kobori, J. A., Herrick, M. K. & Urich, H. Arhinencephaly. The spectrum of associated malformations. *Brain* **110 (Pt 1),** 237–60 (1987).

297. Gleeson, J. G. *et al.* Doublecortin, a brain-specific gene mutated in human X-linked lissencephaly and double cortex syndrome, encodes a putative signaling protein. *Cell* **92,** 63–72 (1998).

298. des Portes, V. *et al.* A novel CNS gene required for neuronal migration and involved in X-linked subcortical laminar heterotopia and lissencephaly syndrome. *Cell* **92,** 51–61 (1998).

299. Pilz, D. T. *et al.* LIS1 and XLIS (DCX) mutations cause most classical lissencephaly, but different patterns of malformation. *Hum. Mol. Genet.* **7,** 2029–37 (1998).

300. Petryk, A., Graf, D. & Marcucio, R. Holoprosencephaly: signaling interactions between the brain and the face, the environment and the genes, and the phenotypic variability in animal models and humans. *Wiley Interdiscip. Rev. Dev. Biol.* **4,** 17–32 (2015).

301. Dubourg, C. *et al.* Holoprosencephaly. *Orphanet J. Rare Dis.* **2,** 8 (2007).

302. Sener, R. N. Rubinstein-Taybi syndrome: cranial MR imaging findings. *Comput. Med. Imaging Graph.* **19,** 417–8

303. Yoo, H. J. *et al.* Whole exome sequencing for a patient with Rubinstein-Taybi syndrome reveals de novo variants besides an overt CREBBP mutation. *Int. J. Mol. Sci.* **16,** 5697–713 (2015).

304. Ross, M. E. & Walsh, C. A. Human Brain Malformations and Their Lessons for Neuronal Migration. *Annu. Rev. Neurosci.* **24,** 1041–1070 (2001).

7. List of figures

8. List of tables

9. Abbreviations

aIP Apical intermediate progenitor

App.[no°] Appendix figure [number]

aRG Apical radial glia

BDNF Brain derived neurotrophic factor

BFT Buried food test

bIP Basal intermediate progenitor

bp Base pairs

BP Basal progenitor

BrdU Bromodeoxyuridin

bRG Basal radial glia

CA Cornu ammonis

CBP CREB binding protein

CC Corpus callosum

CH Cortical hem

CNS Central nervous system

CP Cortical plate

CR Cajal-Retzius

CREB cAMP response element binding protein

CRE cAMP response element

DAB 3,3'-Diaminobenzidine

DAPI 4',6-Diamidin-2-phenylindol

DCX Doublecortin

DG Dentate gyrus

DNE Dentate neuroepithelium

DMS Dentate migration stream

DNE Dentate neuroepithelium

EdU 5-Ethynyl-2´-deoxyuridine

E[no.] Embryonal age in days after conception

EPL External plexiform layer

Fig.[no°] Figure [number]

FL Fibre layer

Fwd. Forward

GC Granule cells

GCL Granule cell layer

GL Glomerular layer

HAT Histone acetyltransferase

HC Hippocampus

H&E Hematoxylin & eosin

HF Hippocampal fissure

HGMD Human Gene Mutation Database (Qiagen Bioinformatics)

HNE Hippocampal neuroepithelium

IPL Internal plexiform layer

LMU Ludwig Maximilians University

LGE Lateral ganglionic eminence

LOT Lateral olfactory tract

LV Lateral ventricle

MCL Mitral cell layer

MRI Magnetic resonance imaging

MZ Marginal zone

NC Neocortex

NEC Neuroepithelial cell

NPC Neural precursor cell

NSC Neural stem cell

n.s. 'Not significant' (No significant statistical difference)

OB Olfactory bulb

OE Olfactory epithelium

ORN Olfactory receptor neurons

OSN Olfactory sensory neurons

PBS Phosphate-buffered saline

PGC Periglomerular cells

P[no.]	Postnatal age in days
pONL	Presumptive olfactory nerve layer
PP	Pre-plate
p	p-value
Rev.	Reverse
RGP	Radial glia precursor
RM	Radial migration
RMS	Rostral migratory stream
RTS	Rubinstein-Taybi-Syndrome
SAP	Subapical progenitor
SEM	Standard error of mean
SGZ	Subgranular zone
SHH	Sonic hedgehog
SNP	Short neural precursor
SP	Sub-plate
SVZ	Subventricular zone
TM	Tangential migration
V-SVZ	Ventricular-subventricular zone
VZ	Ventricular zone
X^2	Chi-squared

10. Acknowledgements

First and foremost, I would like to express my sincere gratitude to **Prof. Dr. Ulrich Schüller**, professor for molecular pediatric neurooncology at the University Medical Center Hamburg, for giving me the opportunity to conduct this research in his workgroup at the LMU Center for Neuropathology and Prion Research (ZNP) and for his great support through his guidance, motivation and critical discussions.

Furthermore, I would like to thank

Prof. Dr. Volker Mall, professor for social pediatrics and medical director of the kbo Kinderzentrum München (Munich Children's Center) and **Dr. med. Monika Cohen** of the kbo Kinderzentrum for the collaboration and their help with contacting RTS patients and their parents for acquiring the MRI data used in this study.

The RTS patients and their parents who not only participated in the study by consenting to the use of the preexisting MRI data but also through their encouraging interest in our work.

Prof. Dr. Birgit Ertl-Wagner, professor for clinical and experimental magnetic resonance imaging, vice-chair Institute of Clinical Radiology and section chief magnetic resonance imaging of the LMU University Clinic, for her aid with analyzing the accquiered MRI images of RTS patients and for providing adequate control MRI data sets.

Dr. rer. nat. Severin Filser and **Dipl. Biochem. Finn Peters** from the German Center for Neurodegenerative Diseases (DZNE) for their aid with acquiring z-stack image data sets using confocal microscopy and the 3D cell reonstruction with Imaris.

Jana Immenschuh for her help with different experiments and analysises during her internship at the LMU Center for Neuropathology and Prion Research (ZNP).

Luke Harrison, **PhD Daniel J. Merk** and **Dr. med Julia Neumann** for their guidance and discussions regarding the experimental setups and their realisation during the course of this work.

And last but not least, **Michael Schmidt, Silvia Occhionero** and **Pia Schindler** for their great technical support as well as the rest of the workgroup and all ZNP coworkers for their combined help and the pleasant working atmosphere.

Appendix

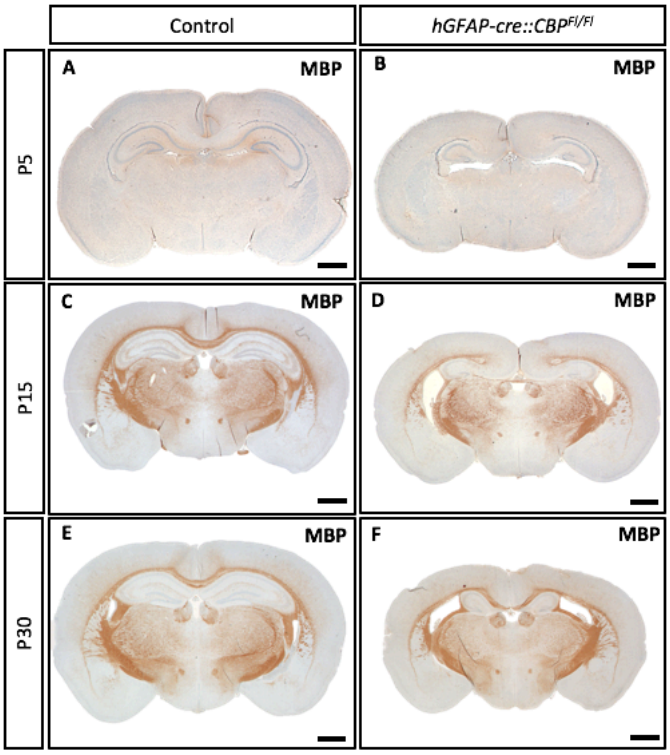

App. 1: Myelination at different postnatal time points after CBP depletion. (A-F) MBP (myelin basic protein) staining of frontal sections at P5, P15 and P30. No substantial differences in MBP expression were observed between transgenic and control animals. Visible differences in the corpus callosum (midline) occur due to an altered corpus callosum development when CBP is missing rather than altered myelination (see. 4.3). *Scale bar: 1250 µm (A,B), 1000 µm (C-F)*

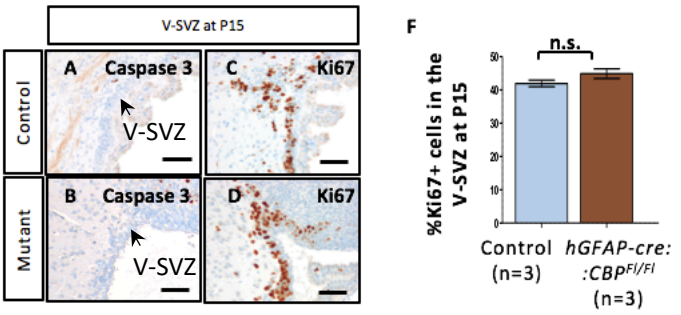

App. 2: Apoptosis and Proliferation in the SVZ at P15. (A,B) No increase of apoptosis was observed in *hGFAPcre::CBP$^{Fl/Fl}$* mice in frontal Casp3 stained sections of the SVZ at P15. **(C,D)** Ki67 proliferation staining of frontal sections of the SVZ at P15. **(F)** No significant difference was measured for the Ki67+ rate in the SVZ at P15 between transgenic and control animals. *Scale bar: 150 µm (A-D)*

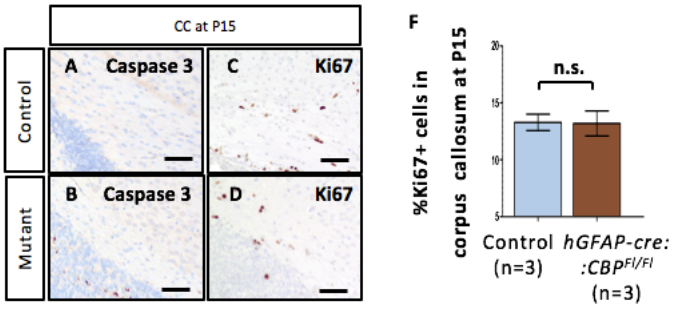

App. 3: Apoptosis and Proliferation in the CC at P15. (A,B) No increase of apoptosis was observed in *hGFAPcre::CBP$^{Fl/Fl}$* mice in sagittal Casp3 stained sections of the CC at P15. **(C,D)** Ki67 proliferation staining of sagittal sections of the CC genu at P15. **(F)** No significant difference was measured for the Ki67+ rate in the CC at P15 between transgenic and control animals. *Scale bar: 200 µm (A-D)*

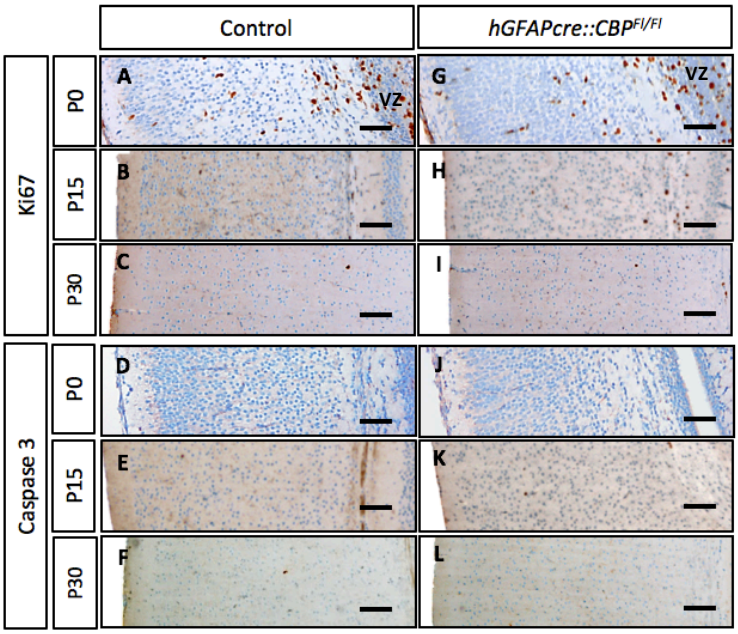

App. 4: Apoptosis and proliferation in the neocortex at different postnatal time points. (A-C, G-I) No difference in proliferation was observed in frontal Ki67 stained sections of the neocortex of *hGFAPcre::CBP$^{Fl/Fl}$* mice at P0, P15 or P30. **(D-F, J-L)** Caspase 3 stained frontal sections of the Neocortex did not reveal differences between transgenic and control animals at P0, P15 or P30 neither in the neocortex nor the ventricular zone (VZ). *Scale bar: 200 µm (A-L)*

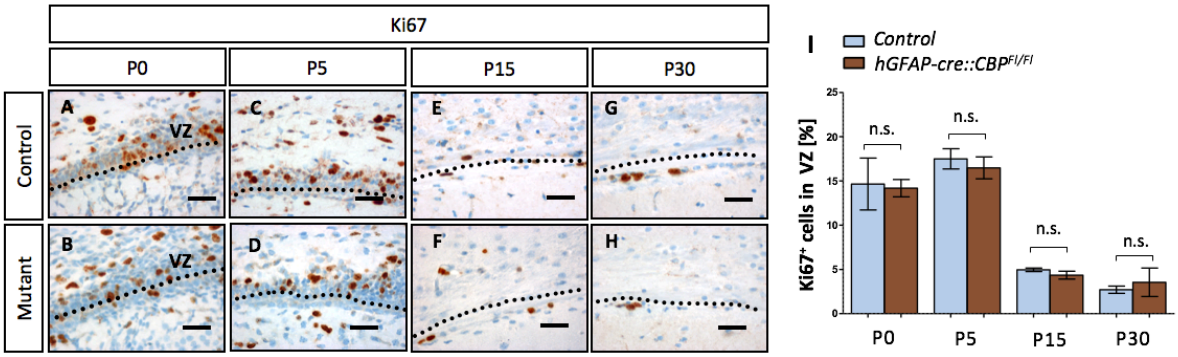

App. 5: Postnatal proliferation-rate in the VZ. (A-H) Ki67 proliferation staining of frontal sections of the ventricular zone at different time points. **(I)** No statistical significant difference was measured for comparing the proliferation rate in the VZ at different postnatal time points between control and transgenic mice. *Scale bar: 100 µm (A-D)*

App. 6: Neurite development. (A-H) No difference in MAP2 and synaptophysin stained frontal sections was observed at P0 and P20, suggesting that neurite development is not impaired in *hGFAPcre::CBP$^{Fl/Fl}$* transgenic mice. *Scale bar: 50 µm (A-H)*

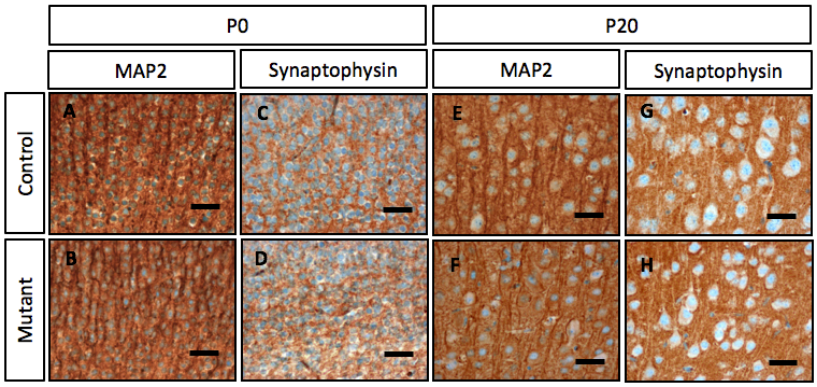

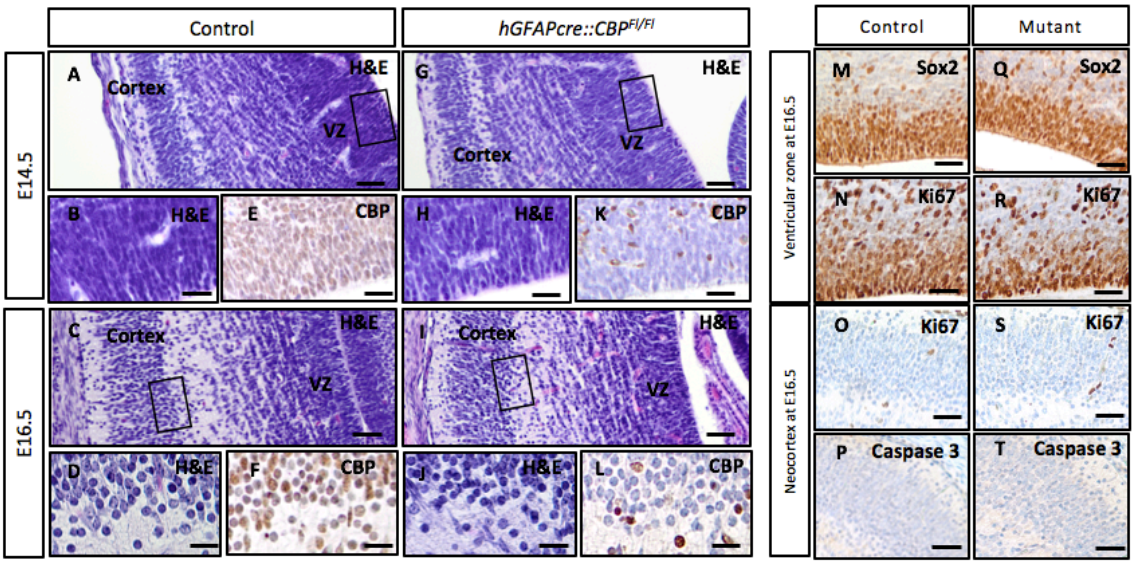

App. 7: Prenatal development of the neocortex. (A,G,C,I) Overview over ventricular zone and the emerging neocortex at E14.5 and E16.5 in H&E staining of frontal sections. **(B,E,H,K)** Ventricular zone at E14.5 with extensive CBP knock-out in CBP stained sections of *hGFAPcre::CBP$^{Fl/Fl}$* animals. **(D,F,J,L)** Early formed layers of the neocortex at E16.5. CBP staining shows depletion in sections from transgenic mice. **(M,Q)** Sox2 staining unveiling stem cell character in the ventricular zone at E16.5. **(N,R)** Ki67 proliferation of the ventricular zone at E16.5 staining suggesting differences between control and transgenic mice. **(O,P,ST)** No significant amount of proliferating or apoptotic cells was observed in the evolving neocortex at E16.5. *Scale bar: 80 µm (A,G), 20 µm (D,J,F,L), 40 µm (B,E,H,K), 50 µm (M-T).*

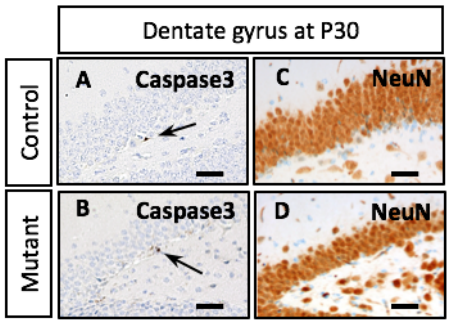

App. 8: Apoptosis and neural differentiation in the dentate gyrus at P30 . (A,B) No relevant amount of apoptotic cells were observed in the dentate gyrus of *hGFAPcre::CBP$^{Fl/Fl}$* and control mice in Caspase 3 stained sections of the dentate gyrus at P30. **(C,D)** NeuN staining of the dentate gyrus shows a unaltered expression of the neural marker NeuN in the granular cell layer. *Scale bar: 40 µm (A-D)*

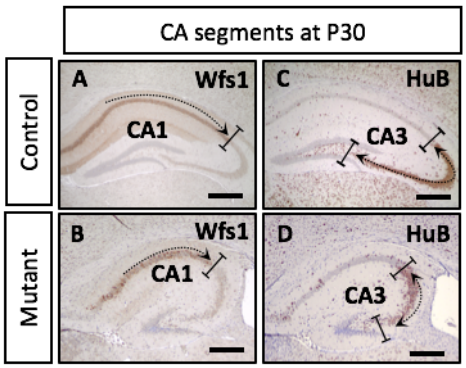

App. 9: Cornu ammonis segments CA1 and CA3 in the hippocampus at P30. (A,B) Wfs1 stained frontal sections of the hippocampus showing the CA1 segment **(C,D))** HuB stained frontal sections of the hippocampus showing the CA3 segment. *Scale bar: 200 µm (A-D)*

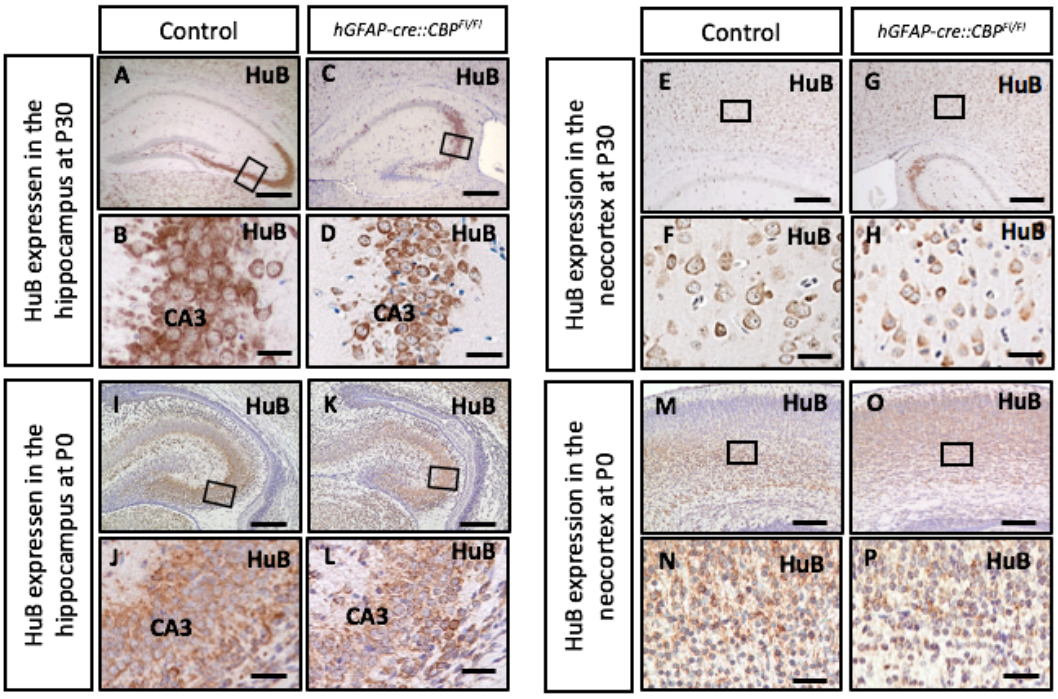

App. 10: Cornu ammonis segments CA3 and HuB expression in pyramidal cells at P0 & P30. (A-D, I-L) HuB expression in the hippocampus marking the CA3 segment at P30 and P0. **(E-H, M-P)** HuB expression in the neocortex, in particular in lamina V giant pyramidal cells at P30 and P0 (F,H,N,P). Both in CA3 and lamina V pyramidal cells HuB is located predominantly in the cell somata rather than the cell nuclei at P0 and P30 with no difference between control and transgenic mice. *Scale bar: 200 µm (A,C,E,G,I,K,M,O), 40 µm (B,D,F,H,J,L,N,P)*

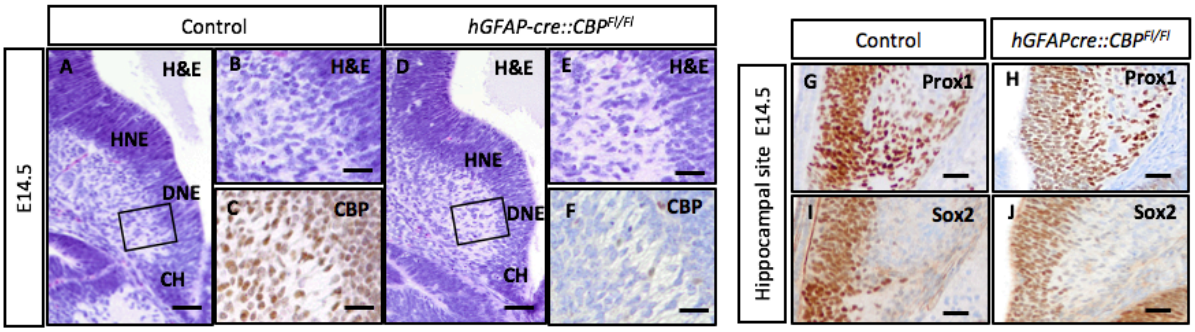

App. 11: Hippocampal development at E14.5. (A,D) Overview over hippocampal formation at E14.5 in H&E staining of frontal sections with neuroepithelium (HNE), dentate neuroepithelium (DNE) and cortical hem (CH). **(B,E,C,F)** Dentate neuroepithelium and ongoing cell migration with complete CBP knock-out in transgenic animals at E14.5. **(G,H)** Prox1 staining at E14.5 confirming dentate granule neuron lineage character of migrating cells in both control and transgenic mice. **(I,J)** Sox2 staining showing stem cell character in the dentate neuroepithelium at E14.5. *Scale bar: 35 µm (A,D), 15 µm (B,C,E,F), 25 µm (G-J).*

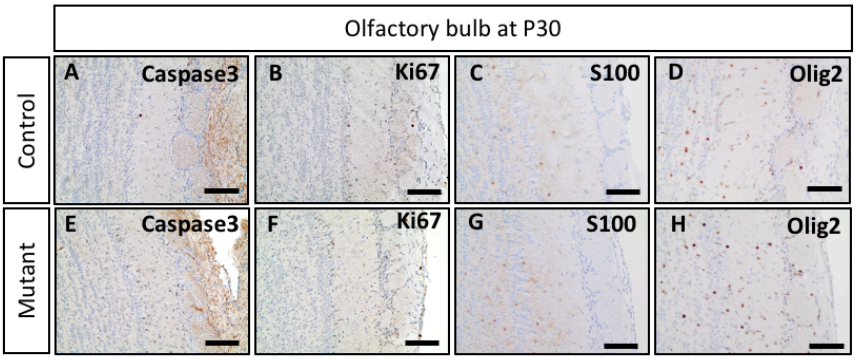

App. 12: Apoptosis, proliferation, and glial differentiation in the olfactory bulb at P30. (A,B,E,F) No relevant amount of apoptotic or proliferating cells were observed in the olfactory bulb of *hGFAPcre::CBP$^{Fl/Fl}$* or control mice in Caspase 3 (A,E) or Ki67 (B,F) stained sections of the olfactory bulb at P30. **(C,D,G,H)** S100 and Olig2 staining of astrocytes and oligodendrocytes in the olfactory bulb at P30 did not unveil striking differences in glial differentiation between transgenic mice and control litter mates. *Scale bar: 80 µm (A-H)*

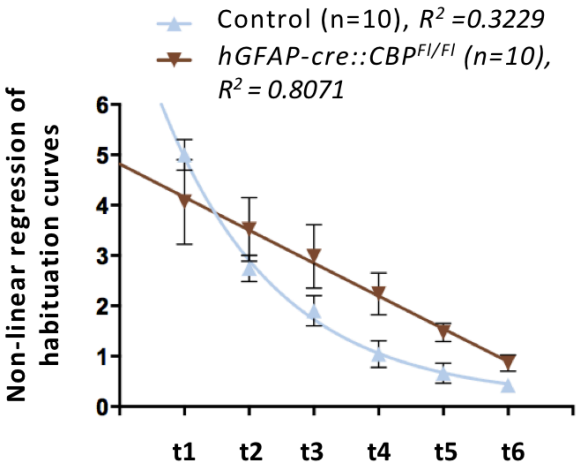

App. 13: Non-linear regression of habituation curves. A one phase exponential decay model *(Y= (Y0 - Plateau)^{K*X} + Plateau)* was used for non-linear regression. The *hGFAPcre::CBP$^{Fl/Fl}$* could not be fitted in an exponential manner due to its more linear character and wider scattering (R^2=0.3229), while regression of the control curve led to a rather good fit (R^2=0.8071), indicating that the chosen exponential model describes the habitation curve of the control group relatively well.